Integration of functions dedicated to the mechanical solicitation and characterization of biological cells in microfluidic devices

Amin Amirouche

N° d'ordre NNT : 2017LYSE1226

THÈSE DE DOCTORAT DE L'UNIVERSITÉ DE LYON
opérée au sein de
l'Université Claude Bernard Lyon 1

École Doctorale ED 160
Électronique, Électrotechnique, Automatique de Lyon (EEA)

Spécialité de doctorat : Ingénierie pour le vivant

Soutenue publiquement le 25/10/2017, par :
Amin AMIROUCHE

Integration of functions dedicated to the mechanical solicitation and characterization of biological cells in microfluidic devices

---

Devant le jury composé de :

BIESHEUVEL Arie, Professeur, Université de Lyon1	Président
ABKARIAN Manouk, Chargé de recherche, CNRS	Rapporteur
GUIDO Stefano, Professeur, Université de Naples Federico 2	Rapporteur
PIERRE-ROLS Marie, Directrice de recherche, CNRS	Examinatrice
COUPIER Gwennou, Chargé de Recherche, CNRS	Examinateur
FERRIGNO Rosaria, Professeur, Université de Lyon1	Directrice de thèse
FAIVRE Magalie, chargé de recherche, CNRS	Co-directrice de thèse
PICOT Stéphane, Professeur des universités - Praticien hospitalier, Université de Lyon1	Invité

UNIVERSITE CLAUDE BERNARD - LYON 1

Président de l'Université	**M. le Professeur Frédéric FLEURY**
Président du Conseil Académique	M. le Professeur Hamda BEN HADID
Vice-président du Conseil d'Administration	M. le Professeur Didier REVEL
Vice-président du Conseil Formation et Vie Universitaire	M. le Professeur Philippe CHEVALIER
Vice-président de la Commission Recherche	M. Fabrice VALLÉE
Directrice Générale des Services	Mme Dominique MARCHAND

COMPOSANTES SANTE

Faculté de Médecine Lyon Est – Claude Bernard	Directeur : M. le Professeur G.RODE
Faculté de Médecine et de Maïeutique Lyon Sud – Charles Mérieux	Directeur : Mme la Professeure C. BURILLON
Faculté d'Odontologie	Directeur : M. le Professeur D. BOURGEOIS
Institut des Sciences Pharmaceutiques et Biologiques	Directeur : Mme la Professeure C. VINCIGUERRA
Institut des Sciences et Techniques de la Réadaptation	Directeur : M. X. PERROT
Département de formation et Centre de Recherche en Biologie Humaine	Directeur : Mme la Professeure A-M. SCHOTT

COMPOSANTES ET DEPARTEMENTS DE SCIENCES ET TECHNOLOGIE

Faculté des Sciences et Technologies	Directeur : M. F. DE MARCHI
Département Biologie	Directeur : M. le Professeur F. THEVENARD
Département Chimie Biochimie	Directeur : Mme C. FELIX
Département GEP	Directeur : M. Hassan HAMMOURI
Département Informatique	Directeur : M. le Professeur S. AKKOUCHE
Département Mathématiques	Directeur : M. le Professeur G. TOMANOV
Département Mécanique	Directeur : M. le Professeur H. BEN HADID
Département Physique	Directeur : M. le Professeur J-C PLENET
UFR Sciences et Techniques des Activités Physiques et Sportives	Directeur : M. Y.VANPOULLE
Observatoire des Sciences de l'Univers de Lyon	Directeur : M. B. GUIDERDONI
Polytech Lyon	Directeur : M. le Professeur E.PERRIN
Ecole Supérieure de Chimie Physique Electronique	Directeur : M. G. PIGNAULT
Institut Universitaire de Technologie de Lyon 1	Directeur : M. le Professeur C. VITON
Ecole Supérieure du Professorat et de l'Education	Directeur : M. le Professeur A. MOUGNIOTTE
Institut de Science Financière et d'Assurances	Directeur : M. N. LEBOISNE

Acknowledgement

After an intensive period of three years, writing this note of thanks is the finishing touch on my PhD adventure. It has been the most rewarding experience for me (until now..), not only from a scientific perspective, but also on a personal level. Here, I would like to reflect on the people who have supported and helped me throughout this journey.

First and foremost, I would like to thank the French Ministry and "Ecole Doctorale EEA" for my thesis grant, as well as Labex iMust for providing the funding without which this work would have not be led. I also thank the UCBL for offering me the teaching opportunity which was a very fruitful experience.

This thesis was led at the "Institut des Nanotechnologies de Lyon" (INL), I would like to thank the laboratory for welcoming me.

I would like to express my sincere gratitude to my advisors Magalie Faivre and Rosaria Ferrigno for the confidence they put in me, their continuous support, their availability, their wise advice as well as for the many hours of work spent on the correction of this manuscript. Besides my advisors, I would like to thank the rest of my thesis committee: Pr Biesheuvel Arie who had the kindness to chair the jury, Pr GUIDO Stefano and Dr ABKARIAN Manouk for their reports and their precious time spent reading and judging this manuscript. Finally, I am grateful for the examinators Dr PIERRE-ROLS Marie and Dr COUPIER Gwennou for their insightful comments, and hard questions.

A big shout out for team LOCI, to start with Louis and Jean-françois for all the chats and photography advice, Gerome for the technical help at the clean room as well as coffee breaks at the meeting room, Nicolas for the technical advice as well as our great moment winning the Futsal tournament. My sincere thanks also goes to Yasmina and Pascal for their precious advice, without forgetting Patrick, Anne-Laure, Laurent, Guoneng, and Marie-Charlotte.

A special mention goes to my fellow labmate and friend Jaime without whom this thesis would have been finished a year earlier... Thanks a lot for all the fun we have had in the last two years as well as for the free Spanish courses. A very special gratitude goes to all the other PhD and Post Doc students I sheared moments with: Josué, Ruoxi, Samir, Sergkei, Pierrick, Rabah, Kevin, Xichen, Thais, Thibaut (I hope I didn't forget anyone).

I would like to thank Magalie and François for the moments spent outside the frame of the thesis, I loved eating at your place... To my baby sister Emma, thanks for the piece of art, it ended up on the wall at my place...

For my forever interested, encouraging and always enthusiastic parents: they were always keen to know what I was doing and how I was proceeding, although it is likely that they have never grasped what it was all about! thanks for your unconditional support.

Finally, last but by no means least, for my sisters who have supported me along the way... Merci infiniment.

RÉSUMÉ

Dans le cadre du développement d'outils diagnostiques basés sur le phénotypage mécanique des cellules présentes dans l'échantillon, cette thèse vise à évaluer deux approches différentes pour la distinction de cellules biologiques aux propriétés mécaniques altérées. Bien qu'ils aient été élaborés avec des globules rouges artificiellement rigidifiés, les concepts développés dans ce travail peuvent être adaptés à d'autres types de cellules.

Dans une première partie, nous avons évalué une approche dite de microfluidique passive où seule la géométrie originale du canal et les forces hydrodynamiques associées, sont responsables de la sollicitation mécaniques des cellules. Nous avons notamment mis en évidence l'existence de deux comportements de relaxation de globules rouges sains en sortie d'une constriction géométrique, selon les paramètres de l'écoulement. La résolution des forces hydrodynamiques, à la transition entre les deux modes de relaxation, nous a permis de determiner le module élastique des globules rouges responsable de cette transition. Bien que cela reste à prouver experimentalement, cette technique pourrait être utilisée pour déterminer des globules rouges mécaniquement altérés.

La seconde approche que nous avons évaluée repose sur la réponse mécanique de globules rouges sollicités par électrodéformation. Nous avons étudié l'influence des paramètres expérimentaux sur l'étirement maximum et le temps de relaxation de la cellule. Cette étude a permis l'obtention d'un jeu de paramètres optimisés pour la sollicitation des cellules sans les altérer.

Une fois les deux techniques caractérisées, nous les avons appliquées à la discrimination de globules rouges sains et de globules rouges artificiellement rigidifiés. Finalement, les avantages et inconvénients de chaque approche sont discutés.

Mots clés: Globule rouge, Microfluidique passive, Électrodéformation, Phénotype mécanique, Déformabilité, Relaxation.

ABSTRACT

In the context of Point of Care (POC) diagnosis tools, based on the mechanical phenotyping of cells present in the sample, this thesis aims at evaluating two different techniques for the distinction of mechanically impaired biological samples. Although, we developed these methods using Red Blood Cells, all the concepts developed in this work can be adapted to other cell types.

In the first part, we evaluated a passive microfluidic approach where only the channel geometry and the associated hydrodynamic forces, are responsible for the mechanical stress of the cells. In particular, we highlighted the existence of two relaxation dynamics of healthy red blood cells at the exit of a geometrical constriction, according to the parameters of the flow. The resolution of hydrodynamic forces at the transition between the two relaxation modes, allowed us to determine the elastic modulus of red blood cells responsible for this transition. Although this remains to be proven experimentally, this technique could be used to determine mechanically altered red blood cells.

In the second approach, we evaluated the mechanical response of red blood cells solicited by electro-deformation. We studied the influence of experimental parameters on the maximum stretch and the relaxation time of the cell. This study allowed us to obtain a set of optimized parameters for the solicitation of the cells without altering them.

Once the two techniques were characterized, we report the evaluation of both techniques in the discrimination of rigidified samples from healthy couterparts. The conclusions of this study and open new perspectives for future works are dicussed.

Keywords: Red Blood Cell, Passive microfluidics, Electrodeformation, Mechanical phenotyping, Deformability, Relaxation.

TABLE OF CONTENTS

LIST OF TABLES

LIST OF FIGURES

CHAPTER 1

INTRODUCTION AND CONTEXT

Currently, large part of the conventional techniques used for medical diagnosis in laboratories, are based on recognition of biomarkers such as DNA, RNA, enzymes, antibodies and antigens, etc... [1] [2] that are mostly detected after a labelling step (nanoparticles, enzyme, ...)[1]. These conventional biomolecular approaches (immunoassays for example) are very well established. However, in the context of Point of Care (POC) diagnosis, performed at the patient side wherever his position, the actual conventional techniques present some drawbacks, among which the high cost, the need for specific storage due to the presence of reagents or the involvement of qualified staff to perform such analysis. Furthermore, in some pathologies, as for example malaria where rapid tests based on immunochromatography detect the presence of specific antigen proteins, the persistence of these biomarkers weeks after the beginning of an efficient therapeutic treatment, may lead to false-positives during future tests and limit their spreading. Therefore, most of the time, blood smear microscopy is favored for malaria.

Along with the improvement of conventional "gold standard" biomolecular techniques, we witness presently the emergence of alternative methods based on the analysis of physical property modification of pathological cells. Properties such as mechanical, electrical or magnetic properties are currently considered to perform medical diagnosis. For example, the variation of dielectrical properties of cells is used in Coulter flow cytometry applications[3]. This technique allows the counting and characterization of a cell population using its specific dielectrical properties. These alternative label free techniques can circumvent the drawbacks of conventional techniques in a context of POC diagnosis.

Cell mechanical properties have also been pointed out as an interesting biomarker for various diseases. Indeed, previous studies in literature have linked several pathologies to significant mod-

[1] Some label-free analytical technique are used to detect such biomarkers as for example impedance measurements and surface plasmon resonance for immunoassays.

ification of cells deformability. For example, variation of White Blood Cells (WBCs) deformability is associated with sepsis [4] and acute respiratory distress syndrome [5]. Increased deformability of metastatic cancer cells [6] and drop of stiffness during stem cell differentiation have also been observed [7]. Red Blood Cells (RBCs or erythrocytes) loss of deformability is associated with sickle cell anemia [8] and malaria [9]. Because of its pathophysiological importance, measurement of RBC deformability has been considerably studied in literature [10] and various techniques have been developed for its characterization. A better understanding of cell deformability and its interactions with cell physical environment may imply tremendous advances in the diagnosis area but also in therapeutics and drug screening assays.

Although conventional techniques allowing the quantification of mechanical properties at a single cell level, such as atomic force microscopy (AFM), micropipette aspiration and optical tweezers, are well-established, they present some limitations. We can cite the necessity of sophisticated equipments, skilled staff and most importantly, they are low throughput (of the order of several tens of cells per day). These limitations make them unadapted for diagnosis applications. Due to a match between cellular length scales and typical sizes accessible by microfabrication methods, microfluidic technologies propose attractive engineered microenvironments for the study of cellular mechanics compatible with high throughput. In the last twenty years, microfluidic techniques have emerged as powerful, label free, high throughput methods to assay the mechanical phenotype of biological cells. These microfluidic tools present various advantages over conventional techniques in terms of sample volume, low cost, portability and capacity of integration in a complete Lab-On-a-Chip (LOC) device. As mentioned earlier, such techniques allow not only the adaptation of channel geometry to cell scale but also the precise control of cell environment. Microfluidic methods can be divided into passive and active approaches. Passive approaches use the variation of channel geometry and associated hydrodynamic constraints to apply forces on the cells, whereas active approaches use an external field using electrical, magnetic or acoustic fields, for example, to manipulate the cells.

This thesis aims at evaluating two different techniques for the distinction of mechanically impaired biological samples. Both approaches were developed and investigated keeping in mind the long term objective which is the application of these techniques to diagnosis based on cell mechanical phenotype. Although, we developed these methods using Red Blood Cells as their mechanical properties can be affected by important pathologies as mentioned previously, all the concepts developed in this work can be adapted to other cell types.

In the present manuscript, we will first introduce in Chapter 2, the link between structural and mechanical properties of Red Blood Cells. In Chapter 3, we will detail the techniques reported in literature to perform mechanical characterization of cells. Then, Chapter 4 will present the different material and methods that have been used for both passive and active approaches. Afterwards, we will discuss our results concerning the mechanical characterization of RBCs using a passive microfluidic technique (Chapter 5). We focused on the shape relaxation of healthy Red Blood Cells (hRBCs) flowing

out of an oscillating width channel and demonstrated the dependency of their mechanical response upon the experimental conditions. In Chapter 6, we will present the results obtained during the study of the mechanical behavior of hRBCs using electrodeformation assays. We investigated the influence of the solicitation parameters on the cell response and concluded on optimized conditions for cell solicitation. Finally, Chapter 7 will discuss the choice and characterization of the model of mechanically impaired cells presenting rigidified properties. Then, we will report the evaluation of both techniques in the discrimination of rigidified samples from healthy couterparts. Finally, Chapter 8, will resume the conclusions of this study and open new perspectives for future works.

CHAPTER 2

STRUCTURAL AND MECHANICAL PROPERTIES OF RED BLOOD CELLS

Contents

2.1 Composition and functions of human blood

Blood is a liquid tissue of the human body, circulating inside a closed vascular system (Figure 2.1-a). It represents a vital biological suspension which constitutes about 8% of the body mass in an adult, and is considered as a connective tissue[1] composed of :

(i) **An aqueous phase**, representing 55% of the blood volume which is the blood plasma. It is composed of 90% of water and 10% of substances such as proteins (albumin, globulins, etc...), carbohydrates, lipids and mineral salts.

(ii) **A solid phase** (Figure 2.1-b), *i.e.* the blood cells which are produced from stem cells in the bone marrow during the hematopoiesis and consisting in 98% of Red Blood Cells (RBCs), 1% of White Blood Cells (WBCs): granulocytes, monocytes and lymphocytes and 1% of Platelets (PLTs). The morphological properties of these cells are presented in Table 2.1.

The presence of these blood cells gives the blood a non-Newtonian behavior, as it is considered as a shear thinning fluid, *i.e.* its dynamic viscosity decreases with increasing shear rate to which this

[1] *Connective tissues* supporting tissue that surrounds other tissues and organs. Specialized connective tissue includes bone, cartilage, blood, and fat. *PubMed Health Glossary*.

fluid is exposed [11]. At physiological flow velocity, blood is ~ 4.5 to 5.5 times more viscous than water [12].

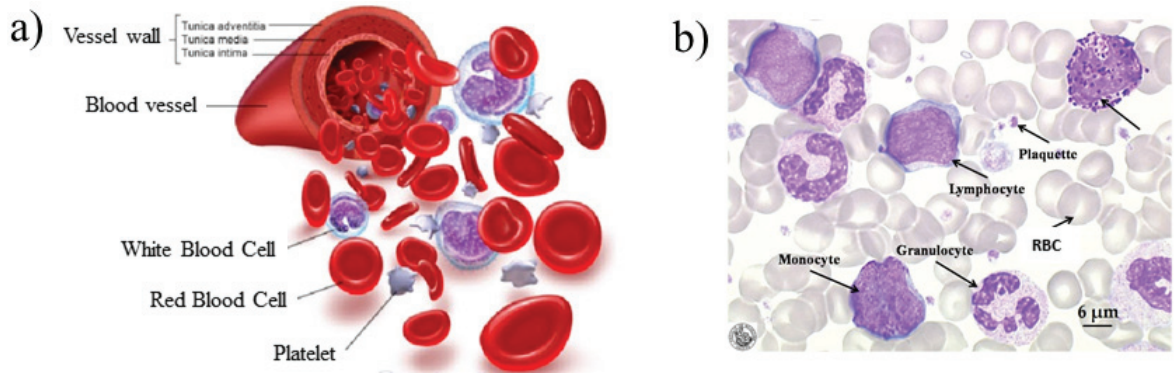

Figure 2.1: (a) Schematic representation of the different blood components flowing in a blood vessel, from [13]. (b) Microscopic image of a blood smear highlighting the different blood cells, from [14].

Cell type	Cell shape	Size (µm)	Concentration (number/µL of blood)
RBCs	discocyte	7-8	$4\text{-}6.10^6$
PLTs	spherical with asperities	2-4	$160\text{-}350.10^3$
WBCs	spherical	10-30	$4\text{-}10.10^3$

Table 2.1: Summarizing table of the size, shape and concentration of the three principal blood cells.

Human blood has mainly three functions:

(i) a function of **transport** of:

- of dioxygen (O_2) and carbon dioxide (CO_2), by the Red Blood Cells (RBCs) or solubilized in the plasma, between the lungs and the rest of the body.
- of hormones.
- of nutrients from digestion and storage.
- of toxins and waste to the liver and kidneys where they will be eliminated.

(ii) A function of **protection** provided:

- by the immune response of WBCs and antibodies during inflammations and infections.
- by coagulation involving fibrinogen and PLT during bleeding in the event of damage to the blood vessel wall.

(iii) A function of **regulation**:

- of the pH.
- of water balance.
- of body temperature by the transfer of heat to the skin.

2.2 Human Red Blood Cells (hRBCs)

Red Blood Cells (RBCs) are the most abundant cells in the blood, from 4 to 6 million per µL. In humans, as in all mammals, RBCs appears as an anucleated cell, which increases its deformability and allows its passage into blood capillaries smaller than their typical size. RBCs, also called erythrocytes, have an average lifespan of approximately 120 days during which they will traffic in the whole organism. RBCs present the form of a biconcave disk of 7 to 8 µm in diameter and about 2 µm in thickness [15] (Figure 2.2). Its surface, typically 130 μm^2, and its volume, ~ 98 μm^3, give to the cell an extended surface comparing to its volume which would be coverable by only 100 μm^2. RBC reduced volume - defined as the RBC volume normalized by the volume of a sphere of the same RBC surface - can be calculated around 0.7, which increases its capacity to deform compared to that of a sphere of same volume.

Indeed, during their flow through the organism, RBCs will have to deform in order to pass through the smallest capillaries of the microcirculation that can be as small as 0.5 to 2.5 µm in diameter in the spleen, the liver and bone marrow[16]. When aging, cells become more rigid and being not able to deform anymore to flow through these pores, get retained in the bone marrow or the spleen. This retention involves about 250 billion of cells per day (about 1% of the total RBC population) [17]. These blocked aged RBCs are then phagocytosed by the macrophages in the physiological haemolysis process, where their components are transformed into amino acids and simple elements that can be immediately reused by the bone marrow to form new cells.

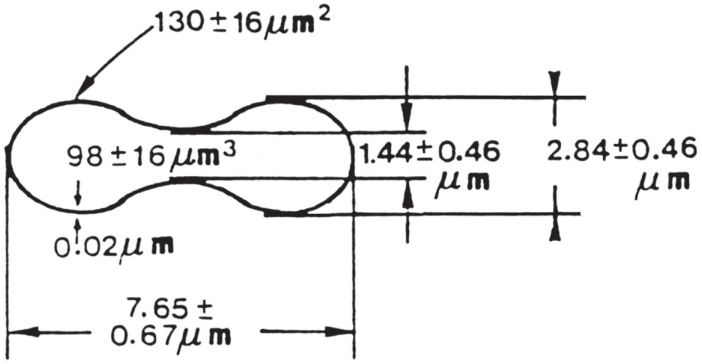

Figure 2.2: Schematic representation of a healthy human RBC, illustrating the biconcave shape and reporting the different dimensions. From [15].

2.3 Structure of the RBC

The RBCs possess a unique structure responsible for their remarkable mechanical properties (deformability, elasticity, shear resistance, etc...) allowing them to flow through capillaries of the microcirculation. Their membrane encloses a cytoplasm made of hemoglobin, allowing the transportation of oxygen through the organism. It is constituted of an elastic 2-D mesh-like spectrin cytoskeleton

anchored to the internal side of a lipid bilayer [18]. Together with the cytoplasmic fluid and the absence of nucleus or other organelles, the membrane controls the overall deformability of the cell.

2.3.1 The RBC membrane

The membrane of human RBC is a multicomponent structure consisting essentially in three layers, as illustrated in Figure 2.3:
(i) An external layer with a forest of peptidoglycans exceeding the proteolipid layer bilayer by about 10 nm of thickness [19].
(ii) A phospholipid bilayer of 5 nm in thickness, composed predominantly of phosopholipids (55%), cholesterol (25%) and dissolved proteins [20]. This lipid bilayer is embedded with transmembrane proteins and junction complexes, which can allow anchoring the cytoskeleton to the lipid bilayer, transporting ions through the lipids (*i.e.* chlorides and bicarbonates, etc...) or expressing the blood group and rhesus.
(iii) A cytoskeleton, mainly consisting in a triangular network of spectrin which maintains the membrane cohesion and the integrity of the cell in flow. It is attached to the lipid bilayer at a distance of about 10 nm through the junction complexes.

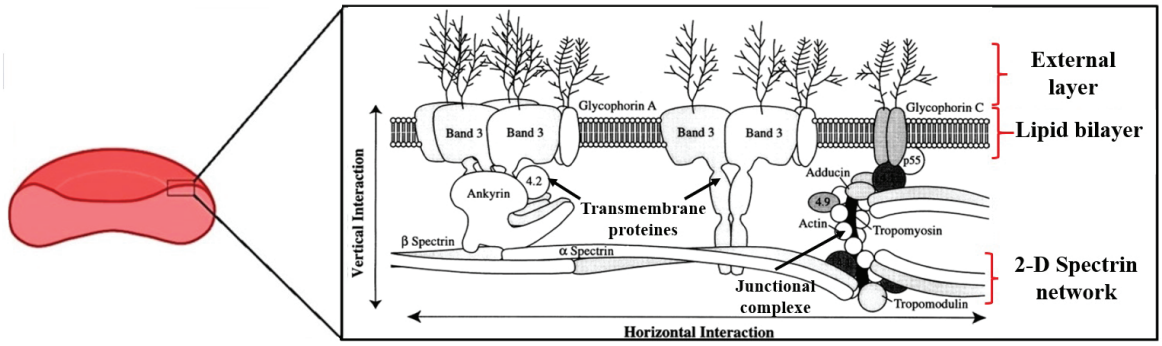

Figure 2.3: Schematic representation of the RBC membrane highlighting the three constituent layers with the spectrin network and the junction complexes, adapted from [20].

The cytoskeleton consists in a network of proteins that underlines the internal surface of the lipid bilayer. This 2-D network (about 10 nm in thickness [21]) is mainly composed of long spectrin filaments (200 nm of contour length [2]) which are interconnected by junction complexes. The spectrin is a heterodimeric fibrous protein, consisting of two strings α and β of about 100 nm in length and 5 nm in diameter wrapped one around another to form an α-β dimer shaped like an helix [21]. Scanning electron microscopic images of the RBC cytoskeleton presented in Figure 2.4-a, highlighted the organization of the skeleton in a triangular-based structure: the ridges consisting in spectrin filament and the vertices corresponding to the junction complexes.

The RBC membrane is considered semi-permeable since it is permeable to water molecules, but impermeable to most ions. This water exchange with the external environment allows the cell to

[2] The contour length is defined as the sum of the length of the two α and β strings constituting the spectrin.

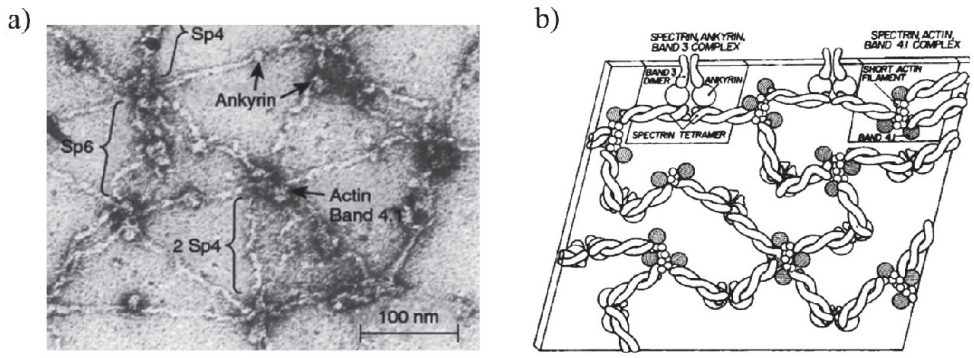

Figure 2.4: (a) Negatively stained electron micrographs and (b) schematic representation of the 2-D network of spectrin with the triangular-based structures, from [22].

support suspending buffer whose salt concentration is abnormal, too high or too low. Physiological media match the osmolarity of the cytoplasm (~ 300 mOsm/kg) hence ensuring isotonic conditions. Depending on the osmolarity (*i.e.* salt concentration) of the surrounding environment, the RBC membrane exchanges water with the external environment in order to balance the osmotic pressure on both sides. Therefore, by respecting the energy minimization principle, the cell adapts its shape to its new volume as illustrated in Figure 2.5. As stated earlier, in an isotonic medium, the RBC has a discoidal shape, whereas in a medium with low osmolarity (*i.e.* hypotonic buffer), the water of the surrounding medium crosses the membrane to enter the cytoplasm and dilute its salt concentration; in consequences the cell inflates to become a stomatocyte (Fig. 2.5 right). At 150 mOsm/kg, it is perfectly spherical and if the osmolarity is further decreased, the cell membrane ruptures under the tension and the hemoglobin is released: its the lysis phenomenon. At osmolarity greater than 300 mOsm/kg (*i.e.* hypertonic conditions), the water molecules contained in the RBCs exit the cell towards the external environment and the cell deflate to an echinocyte (Fig. 2.5 left).

2.3.2 The RBC cytoplasm

The cytoplasm of the RBC is mainly composed of hemoglobin which account for about 33% of the weight of cell [17]. Hemoglobin determines the internal viscosity of the cell which is ~ 6.5 mPa.s at 37°C and 10 mPa.s at 25°C [19]. Hemoglobin consists in the major part of proteins, called **globins**, itself composed of four polypeptides (long chains of amino acids), two strings α and two strings β, attached to each other. To each chain of globin is fixed a molecule of heme, which serves to fix oxygen on its atom of iron. Hemoglobin has a bright red color, when it is oxygenated, and becomes brown when it has lost its oxygen. Abnormal structure of the hemoglobin may influence the shape and deformability of the RBC, as for example in sickle cell anemia where the physiological hemoglobin "A", normally found in RBCs, is replaced by the pathological hemoglobin "S", also called **sickle cell hemoglobin**, capable of polymerizing into rigid fibers hence deforming the erythrocyte into a sickle cell [24].

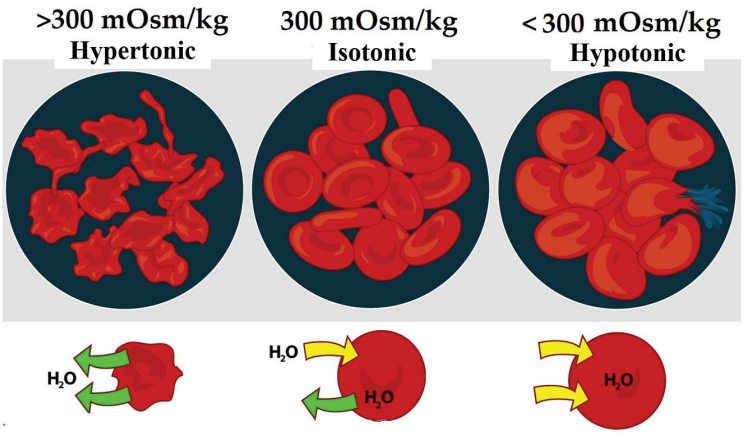

Figure 2.5: Illustration of the effect of the osmolarity of the surrounding buffer on the shape undergone by RBCs. In an isotonic buffer (~ 300 mOsm/kg), the RBC is discosyte. It becomes equinocyte when suspended in a hypertonic buffer (> 300 mOsm/kg) and stomatocytye in hypotonic conditions (< 300 mOsm/kg), from [23].

2.4 Mechanical aspects of the RBC membrane

The unique deformation capability of the RBCs results from the combination of its particularly low volume to surface ratio, the tremendous mechanical properties of its membrane and the loss of its nucleus during its maturation. The study of the mechanical behavior of the RBC involves inevitably the analysis of its membrane deformability. In 2-D general mechanics, the deformation of a material can be decomposed into three components, illustrated in Figure 2.6: (i) the isotropic deformation of extension-compression, (ii) the pure shear deformation, where the surface area is conserved and (iii) the deformation by curvature perpendicular to the material plane.

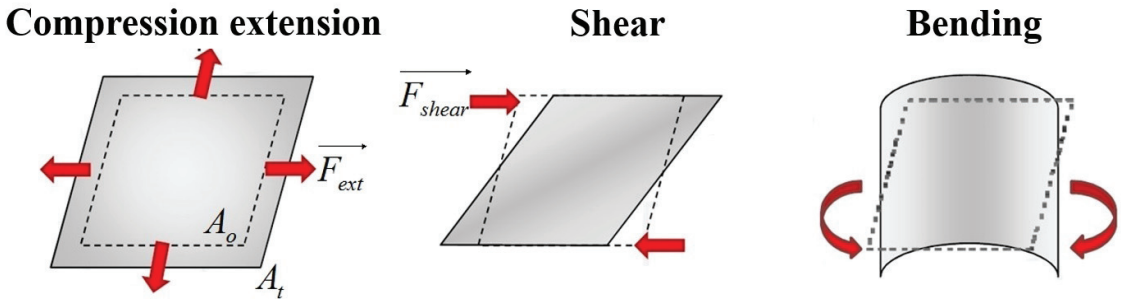

Figure 2.6: Schematic representation of the three basic types of deformation of 2-D material: compression-extension, shear and curvature. Adapted from [20].

In response to an external stress, the RBC presents, due to its composition, a behavior which is both viscous and elastic.

2.4.1 The elastic properties

The elasticity of the RBC characterizes its deformability under an applied force; it is only dictated by the elastic properties of its membrane structure. Due to its thinness, the membrane can be treated using as a 2-D continuum model. Despite the complexity of RBC membrane deformation, it can be explained by the three fundamental deformation modes as follows.

The **pure compression-extension** is characterized by the energy necessary to change (increase in the case of extension or decrease in the case of compression) the membrane surface area without any change in shape. This energy is characterized by the membrane extension-compression modulus k defined by [25]:

$$F_{ext} = k\frac{\Delta A}{A_o} \tag{2.1}$$

where F_{ext} is the external force applied to trigger the deformation, A_o is the initial surface area of the membrane and $\Delta A = A_t - A_o$ corresponds to the variation in surface area at the instant t as represented in Figure 2.6.
The extension-compression modulus k of a RBC is essentially dominated by the elasticity of its lipid bilayer which is weakly extensible, the lipids resisting the extension to avoid exposing their hydrophobic tails to the aqueous media on each side of the membrane. The bilayer expansion-compression modulus of the RBC was measured at 200-300 mN.m^{-1} by Rawicz et al. using micropipette pressurization of giant lipid vesicles [26]. Therefore, this relatively high modulus imposes constant surface deformations to the RBCs, so the extension-compression phenomena are usually neglected [27]. The expansion-compression modulus is strongly temperature-dependent (-6 mN/m°C [28]).

The deformation by **pure shear** corresponds to a modification of the membrane shape at constant surface area as schematized in Figure 2.6. It is characterized by the shear modulus μ defined as [29]:

$$T_s = \frac{\mu}{2}(\lambda^2 - \lambda^{-2}) \tag{2.2}$$

with T_s, the shear force and λ, the extension ratio defined by $\lambda = l_t/l_o$, where l_t is the extended dimension and l_o is the same dimension at rest. For a RBC, the shear modulus is mainly determined by the spectrin cytoskeleton, the lipid bilayer being considered completely fluid in the case of a shear stress [20]. μ has been measured experimentally in the order of 2.5-9 µN/m [29, 30]. These values may decrease with the temperature [28], or increase with increasing pH [31].

Finally, the deformation of **pure curvature**, corresponds to a change of curvature of the membrane with constant area and shape. This deformation is characterized by a curvature modulus B defined as [20]:

$$M = B(C_1 + C_2 - C_3) \tag{2.3}$$

where M is the moment of curvature, C_1 and C_2 the two curvatures in the two principal planes, and C_3 the curvature in the stress-free state.

For a RBC, the elastic curvature modulus B is mainly determined by the chemical composition of the lipid bilayer. It is very little influenced by the temperature [32] and hardly varies with the hemoglobin concentration [33]. Measurements of B for a RBC, give values ranging from 10 to 50 $k_bT \sim$ 2-19 Nm, k_b being the Boltzmann constant and T the temperature in Kelvin [34].

2.4.2 The viscous properties

The viscous response of the RBC characterizes its resistance to a rate of deformation [35], it has mainly two origins:

(i) The viscosity of its membrane $\eta_{2Dmemb} \sim 0.5-1.10^{-6}$N.s.m^{-1} [36] which is imposed by the type of lipids and their physical states (sol or gel phase) which is directly influenced by the temperature. In literature, the membrane viscosity is reported to be the major source of viscous dissipation of energy during RBC relaxation after large deformations [35].

(ii) The viscosity of the cytoplasm (*i.e.* the hemoglobin) η_{in} of the order of 6 mPa.s at physiological concentration [37]. According to literature, its effect on energy dissipation is generally neglected [27].

2.4.3 The Kelvin-Voigt model

In 1976, E.A. Evans and R.M. Hochmuth [25, 27, 35] developed a theory for viscoelastic behavior of large membrane deformations. The model describes the mechanical behavior of RBCs as that of a Kelvin-Voigt material. Such viscoelastic behavior is intermediate between that of an ideal elastic solid, of elastic modulus E, capable of conserving its energy, and that of a purely viscous Newtonian liquid of viscosity η, able to dissipate energy. Kelvin-Voigt materials can be modelled as a spring mounted in parallel to a purely viscous damper as represented in Figure 2.7.

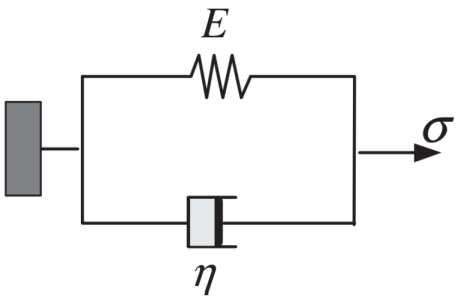

Figure 2.7: Schematic representation of the Kelvin-Voigt model, from [38].

Their model describes the shape relaxation of cell membranes for short lasting stresses, while considering the simultaneous elastic energy storage and internal viscous dissipation. For durations beyond 5 min or membrane expansion rates > 3-4:1, the membrane exhibits a plastic behavior and the model is no longer valid [35]. The elements of the calculation are briefly reminded here. The total tension force T_s is the sum of an elastic term T_s^e depending on the instantaneous strain and a viscous

term T_s^v depending on the instantaneous rate of strain:

$$T_s = T_s^e + T_s^v \tag{2.4}$$

where the first-order hyperelastic relation for a membrane is expressed as:

$$T_s^e = 2\mu\epsilon_s = \frac{\mu}{2}(\lambda^2 - \lambda^{-2}) \tag{2.5}$$

where μ is the elastic shear modulus of the RBC, $\epsilon_s = (\lambda^2 - \lambda^{-2})/4$ represents the shear deformation at constant surface area, λ being the extension ratio of the membrane.
The first-order viscous relation between shear resultant T_s^v and the rate of shear deformation of a "Newtonian" surface liquid is defined as:

$$T_s^v = 2\eta_{memb} V_s = \frac{2\eta_{memb}}{\lambda}\frac{\delta\lambda}{\delta t} \tag{2.6}$$

where η_{memb} is the membrane viscosity and $V_s = \frac{1}{\lambda}\delta\lambda/\delta t$ is the rate of membrane shear deformation per unit of time.
Consequently, equation 2.4 becomes the first-order constitute equation for a viscoelastic membrane solid :

$$T_s = \frac{\mu}{2}(\lambda^2 - \lambda^{-2}) + \frac{2\eta_{memb}}{\lambda}\frac{\delta\lambda}{\delta t} \tag{2.7}$$

The normalization of equation 2.7 by 2 μ gives:

$$\frac{T_s}{2\mu} = \frac{1}{4}(\lambda^2 - \lambda^{-2}) + \frac{\eta_{memb}}{\mu}\frac{\delta ln\lambda}{\delta t} \tag{2.8}$$

By solving equation 2.8 when the applied stress is removed ($T_s = 0$), we find an expression of the evolution of the cell shape during the relaxation process:

$$\lambda(t) = \left[\frac{\Lambda + e^{-t/\tau}}{\Lambda - e^{-t/\tau}}\right]^{1/2} \tag{2.9}$$

τ being the characteristic time of relaxation expressed as:

$$\tau = \frac{\eta_{2Dmemb}}{\mu} \tag{2.10}$$

and

$$\Lambda \equiv \frac{\lambda_m^2 + 1}{\lambda_m^2 - 1} \tag{2.11}$$

where λ_m is the maximum deformation just before the cessation of the stress, *i.e.* just before the beginning of the relaxation.

Assuming that L and W represent the length and the width of the cell respectively:

$$\frac{L}{W} = \left(\frac{L}{W}\right).\frac{\Lambda + e^{-t/\tau}}{\Lambda - e^{-t/\tau}} \tag{2.12}$$

The linearization of equation 2.9 gives:

$$\frac{\left(\frac{L}{W}\right)-\left(\frac{L}{W}\right)_{\infty}}{\left(\frac{L}{W}\right)_{m}-\left(\frac{L}{W}\right)_{\infty}}=e^{-t/\tau} \tag{2.13}$$

with the index m and ∞ representing the state of maximum deformation and the equilibrium state after relaxation, respectively.

The model described here predicts that the RBC relaxation time is a constant which only depends on RBC intrinsic mechanical properties which are its elastic shear modulus μ and its membrane viscosity η_{memb} (see equation 2.10). We can notice that the relaxation is dominated by the membrane viscosity, the cytoplasm and the external viscosities having been neglected.

CHAPTER 3

CELL MECHANICAL PHENOTYPING

Contents

Several techniques have been developed to characterize the mechanical phenotype of cells. These different methods can be classified into two categories:
(i) The "**collectives**" techniques (illustrated Figure 3.1-a), which are performed on diluted (or not) suspensions of Red Blood Cells (RBCs), such as viscosimetry [39], rheometry [40] and ektacytometry [41], are techniques which deliver an averaged measurement on a large cells population.
(ii) The "**single cell**" techniques (Figure 3.1-b), as for example the famous micropipette aspiration technique [35], optical tweezers [30] and Atomic Force Microscopy (AFM) [42], allow carrying out mechanical characterization on individual cells.
Although conventional techniques allowing the quantification of cellular viscoelastic properties, such as AFM, micropipette aspiration and optical tweezers [43] are well-established, they require sophisticated equipments and skilled personal and most importantly are low throughput (of the order of several tens of cells per day). Due to a match between cellular length scales and typical sizes accessible by microfabrication methods, microfluidic technologies propose attractive engineered microenvironments for the study of cellular mechanics which are compatible with high throughput. Therefore, during the past twenty years or so, we have witnessed the emergence of a third category of techniques, based on **Microfluidics and Micro-Electro-Mechanical Systems (MEMS)** technologies as illustrated in Figure 3.1-c. This new category combines measurements on individual cells to high throughput.

The present chapter begins with a brief overview of "collective" and "single cell" techniques, then we describe recent advances in microfluidic assays for single cell biomechanical characterization.

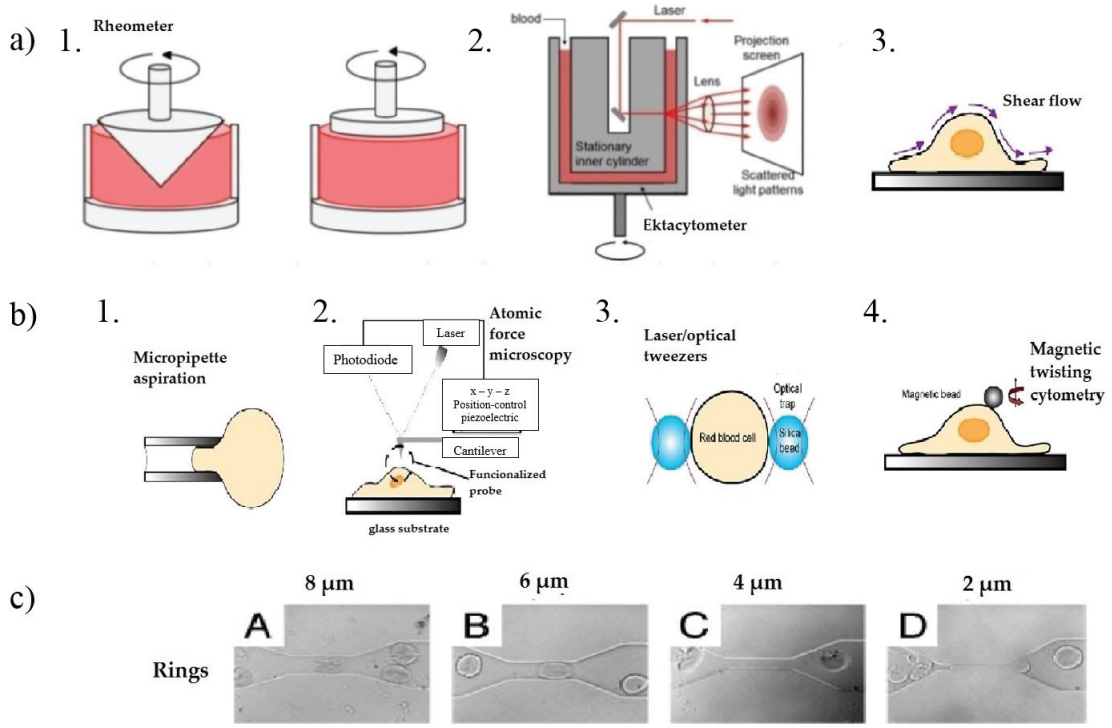

Figure 3.1: Illustration of the three categories of techniques, developed to perform mechanical phenotyping of cells, and that are reported in literature: (a) collective techniques: (a.1) rheometer, (a.2) ecktacytometer or (a.3) shear flow assays (from [20, 43]), (b) Single cell techniques: (b.1) micropipette aspiration, (b.2) AFM, (b.3) optical tweezers and (b.4) MTC (from [43]) and (c) An example of the microfluidic techniques: constriction channel assays (from [44]).

3.1 Collective techniques

Among the collective methods to characterize blood cells and which are directly performed on blood samples, we can cite the viscosimetry, the rheometry and the ektacytometry.

Measurements by **viscosimetry** can be done either by keeping the fluid stationary and by moving an object through it, or by immobilizing the object and flowing the fluid around it. The observation of the flow allows evaluating the drag force which is related to the viscosity of the solution η_{out} by:

$$\vec{F}_{drag} = 6\pi\eta_{out}R_{obj}\vec{V}_{obj} \tag{3.1}$$

where R_{obj} is the object radius and V_{obj} its speed relative to that of the solution.
This technique was used to evaluate η_r, the ratio between the internal viscosity of RBCs in suspension and that of the external fluid of different viscosities η_{out} such as dextran [39]. We can connect η_r and

the viscosity of the RBC cytoplasm η_{in}, using the Taylor viscosity equation[39]:

$$\eta_r = 1 + 2.5CTa \tag{3.2}$$

C, representing the hematocrit[1] and Ta, the Taylor factor equal to $(\frac{\eta_{in}}{\eta_{out}} + 0.4)/(\frac{\eta_{in}}{\eta_{out}} + 1)$.
This technique was applied by Dintenfass et al. [39] to evaluate the internal viscosity of the RBC and they found a range of values η_{in} = 1-6 mPa.s depending on experimental conditions.

The use of a **rheometer** allows applying a stress to the RBC suspension using plates which are rotating relative to one another (rheometer configuration can be plate/plate, cone/plate, couette... as illustrated in Fig. 3.1-a.1). Observation of the cell deformation between the two moving plates, while varying the applied shear rate, permit the measurement of the overall blood viscosity [45, 46]. This technique can also be used to estimate the relaxation time of RBCs after the stop of the moving plate [10]. Another variant of rheometry (Figure 3.1-a.3) uses the stress induced by a **shear flow** to stretch RBCs previously bonded to a substrate and allows the estimation of cell deformation, or the cell relaxation time [47].

Ektacytometry (Figure 3.1-a.2) uses a laser diffraction method combined with a "Couette" rheometer to measure the deformability of RBCs. The deformation of the cells is deduced from the diffraction pattern issued from the interaction of a laser beam and the cells in the blood sample. Indeed, while RBCs deform in response to the applied stress, the pattern shows an elliptic shape [48] (Figure 3.1-a.2) whereas in absence of deformation this same pattern is roughly circular. Measurements of $l_{ellipse}$ and $s_{ellipse}$, respectively the major and minor axes of the elliptic pattern, allowed calculating a deformation coefficient $D_{ellipse}$ = ($l_{ellipse}$ - $s_{ellipse}$)/($l_{ellipse}$ + $s_{ellipse}$). It has been shown that the measurements of $D_{ellipse}$ are correlated to measurements of the deformation coefficient of the cells D, defined as D = ($2a$ - $2b$)/($2a$ + $2b$), where $2a$ and $2b$ are respectively the major and minor axes of the stressed cells. Baskurt et al. [49] studied the evolution of $D_{ellipse}$ as a function of time after stopping the rheometer and managed to extract a cell shape relaxation time τ = 97 ± 15 ms, for an external viscosity η_{out} = 24.8 mPa.s [49]. The authors showed that the relaxation time τ of RBCs varies with η_{out}. Indeed, as presented in Figure 3.2, they have reported that when suspended in a buffer of external viscosity $\eta_{out} \leqslant$ 10 mPa.s, the relaxation time τ of RBCs was increasing from 60 ms at η_{out} = 3 mPa.s to 120 ms at 10 mPa.s. Whereas above 10 mPa.s, it was decreasing from 110 to 30 ms when η_{out} is increased from 16 to 29 mPa.s. Such variations of τ is contradictory with the Kelvin-Voigt model which predicts that the RBC relaxation time depends only on intrinsic properties of the cells *i.e.* its elastic shear modulus μ and its membrane viscosity η_{memb} (as already stated in Chapter 2). The model does not take into account the dissipation in external buffer.

These collective methods, mostly used between the 70's and the mid 90's, provide access to averaged measurements of the properties over a large population, *i.e.* the whole blood sample.

[1] Volume of RBCs relative to the total volume of blood.

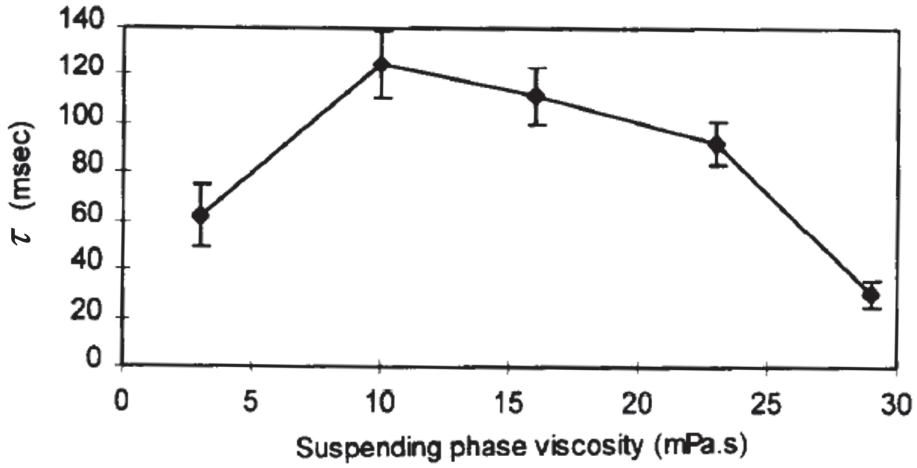

Figure 3.2: Evolution of the shape relaxation time τ of RBCs measured by ektacytometry as a function of the viscosity η_{out} of the external buffer. Measurements reveal that for $\eta_{out} \leqslant 10$ mPa.s, τ increases with η_{out}, whereas, for $\eta_{out} > 10$ mPa.s, it decreases with increasing η_{out}. From [49].

Therefore, they are not able to detect the variation of behavior of a small portion of the population and thus are not adapted to the medical diagnosis of diseases such as malaria where the number of mechanically affected cells in a blood sample may be as low as 0.02 %. Hence, techniques able to perform mechanical phenotyping of cells at the scale of the single object needed to be developed.

3.2 Single cell techniques

3.2.1 Micropipette aspiration

Micropipette aspiration is one of the most widely spread methods for measuring the mechanical properties of the RBC membrane. The technique uses a glass micropipette of internal diameter ~ 1-3 µm, to suck a tongue of RBC membrane by applying a negative pressure in the pipette [50]. Measurement techniques may vary, either by measuring the pressure required to suck a tongue of membrane which length is equal to the diameter of the micropipette (Fig. 3.3-a), or by measuring the ratio between the aspirated length and the diameter of the micropipette at a given pressure (Fig. 3.3-b). Finally, the measurement of the pressure necessary to aspirate the whole cell inside the micropipette (Fig. 3.3-c) can also be used to extract information about RBC properties [29].

The micropipette aspiration technique allows measuring the extension modulus k of the RBC using equation (3.3) linking k to the difference of pressure applied to the pipette and using aspirated cell dimensions of both the aspirated cell and the pipette [19]:

$$k = \frac{R_0^2}{1 - R_p/R_0}\left(\frac{\Delta P}{\Delta L}\right) \tag{3.3}$$

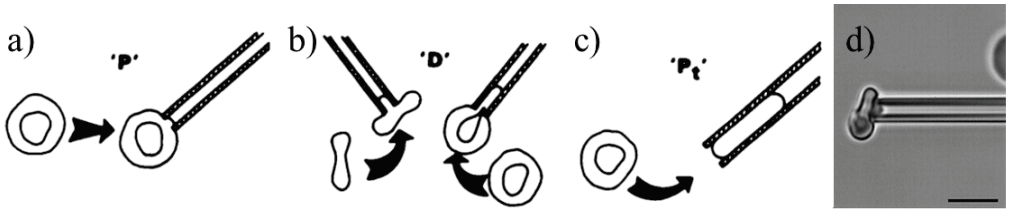

Figure 3.3: (a),(b) and (c) represent schematic illustrations of the three different variants of the micropipette aspiration technique, from [20]. (d) Microscopic image of a RBC being sucked in a micropipette, from [51]. The scale bar represents 10 µm.

where R_0 is the cell radius before aspiration,R_p the micropipette radius, ΔL the RBC aspirated length and ΔP the applied difference of pressure in the pipette. Values of k for the RBC membrane have been reported in the literature in the order of 300 to 500 mN.m^{-1} [28, 29], while values of k for the lipid bilayer alone are reported to be ~ 200-300 mN.m^{-1} [26].

Micropipette aspiration has also been used to evaluate the RBC shear modulus μ using the length of the aspirated membrane tongue defined as D_p:

$$\mu \sim \Delta P R_p^2 / D_p \tag{3.4}$$

where R_p is the radius of the micropipette and ΔP the applied pressure [29, 52].
The values of μ measured by micropipette are of the order of 9 ± 1.7 µN.m^{-1} [33].

The elastic curvature modulus B of the RBC membrane can also be recovered from micropipette aspiration measurements according to the following relationship:

$$B \sim A \Delta P . R_p^3 \tag{3.5}$$

A being equal to $\frac{1}{135}$ or $\frac{1}{55}$ as a function of the ratio between the radius of curvature of the RBC and the diameter of the micropipette [29].
Values of B extracted are in the order of 43.5 $k_b T$ (k_b being the Boltzman constant and T the temperature) [34]. In addition to the dependence of B regarding the radius of the micropipette, the curvature modulus also depends on the applied pressure.

Finally, the relaxation time τ of RBCs can be measured by micropipette aspiration. As the negative pressure inside the pipette is stopped, the cells relax and return to their initial discocyte-like shape. τ was estimated to be 100 ms [27], which is in good agreement with the Kelvin-Voigt model.

Micropipette aspiration is a gold standard technique that allows measuring the different elastic moduli of the RBC. However, the need for skilled staff, difficulty to automate the measurements and the fact that it remains a low throughput technique - with about ten cells processed per day - makes it hardly compatible with diagnosis applications.

3.2.2 Atomic force microscopy (AFM)

Invented in 1985 [53], atomic force microscopy (AFM) is a near-field microscopic technique that offers the opportunity of imaging biological sample topography as well as probing its mechanical properties locally without damaging it. The technique relies on the physical contact of a very fine tip, positioned at the end of a flexible cantilever, and the surface to be scanned. The vertical movement of the tip induces small flexions of the cantilever which are detected precisely by photodiodes, through the reflection of a laser beam on the cantilever, as illustrated in Figure 3.4-a. This technique makes it possible to analyze variations of height as low as few nanometers and to measure forces of the order of nN. Figure 3.4-b presents the 3-D topographic image of a RBC made by AFM.

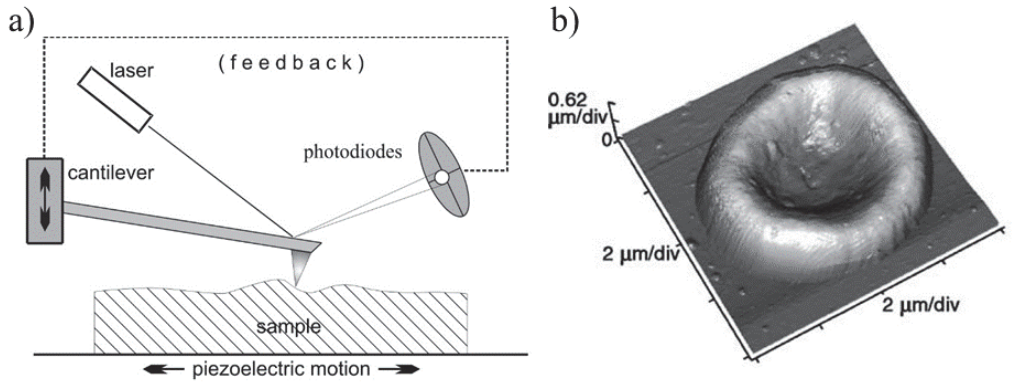

Figure 3.4: (a) Schematic illustration of the principle of AFM, from [54]. (b) 3-D topographic image of a RBC made by AFM, from [55].

Different types of tips can be used, depending on the force to be applied or the sensitivity of the specimen [56]. For a spherical or parabolic tip with a radius of curvature R_c, the applied force F is connected to the relative Young modulus E^* and the indentation Δz by [56]:

$$F = \frac{4\sqrt{R_c}}{3}.E^*(\Delta z)^{3/2} \tag{3.6}$$

where E^* is defined as:

$$E^* \sim \frac{E_{RBC}}{1-\nu^2} \quad \text{for} \quad E_{RBC} \ll E_{tip} \tag{3.7}$$

E_{RBC} and ν being the RBC Young modulus and its Poisson's ratio, respectively.
The relation (3.7) is only valid for a tip much more rigid than the object under study, which is the case for most biological samples (typically, for a tip in Si_3N_4, $E_{tip} \sim 150$ GPa). The Young modulus of RBC was measured by AFM to be of the order of 4.4 ± 0.6 kPa [55].

Another variant of the AFM measurement consists in using a colloidal probe, 10 to 100 µm in diameter, attached to the cantilever in order to deform the overall cell under study, in contrast to the nanometric tip where the response is local (Figure 3.5). By knowing exactly the geometry of the

colloidal probe, and using equation (3.6) where R_c becomes the radius of curvature of the colloid, the cell mechanical properties can be extracted (Figure 3.5-b).

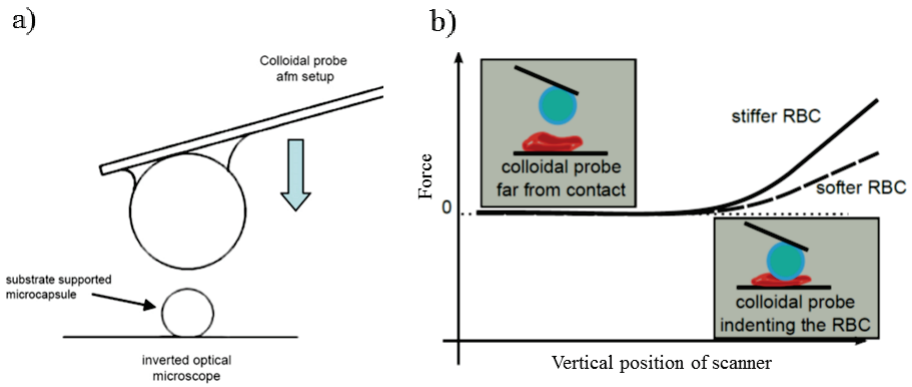

Figure 3.5: (a) Schematic representation of the principle of the colloidal probe technique, from [57]. (b) Illustration of a typical force measurement curve obtained for a rigid RBC and a deformable one, from [58].

AFM allows precise measurements of the mechanical properties of biological cells, but with a relatively slow rate of acquisition. It requires heavy equipment (AFM microscope) and qualified staff, hence preventing its use for Point-Of-Care applications; this technique is therefore incompatible with routine medical diagnosis.

3.2.3 Optical tweezers

Optical tweezers rely on the use of highly focused laser beams to optically trap and deform micro- or nanometric spherical particles [59]. In a first implementation of the technique, a particle is subjected to a strong highly focused gradient of light as illustrated in Figure 3.6-a. The optical forces associated to incident rays of light ($\vec{F_A}$ and $\vec{F_B}$) are proportional to the light intensity (if B is brighter than A, then $\vec{F_B} > \vec{F_A}$) (Figure 3.6-a). The resulting force ($\vec{F_{res}} = \vec{F_A} + \vec{F_B}$) tends to displace the sphere in the direction of the brightest ray of light [60]. $\vec{F_{res}}$ is governed by the size of the particle, its refractive index, that of the surrounding environment and the power of the laser (gradient of the light)[20].
The light gradient can be used to trap the beads, using a focused gaussian light beam [61]. As illustrated by the schematic in Figure 3.6-b, the light gradient generates two forces $\vec{F_A}$ and $\vec{F_B}$ of equal intensity but of opposite directions exerting thus a trapping effect on the cell.
In a second implementation, optical tweezers can also be used to probe mechanical properties of cells by manipulating diametrically opposed microspheres bonded to the cellular membrane (Figure 3.6-c) [30]. The opposed displacement of these microbeads by the use of two different optical traps allows the stretching of the cell. Knowing the applied stress, changes in the cell diameter can be converted into an elastic modulus or shear modulus of the cell.

The same type of measurements can be performed with other types of stimuli: by the use of an electric field gradient [62], a magnetic field gradient or even an acoustic field gradient [63], thereby providing dielectrophoretic, magnetic or acoustic tweezers, respectively.

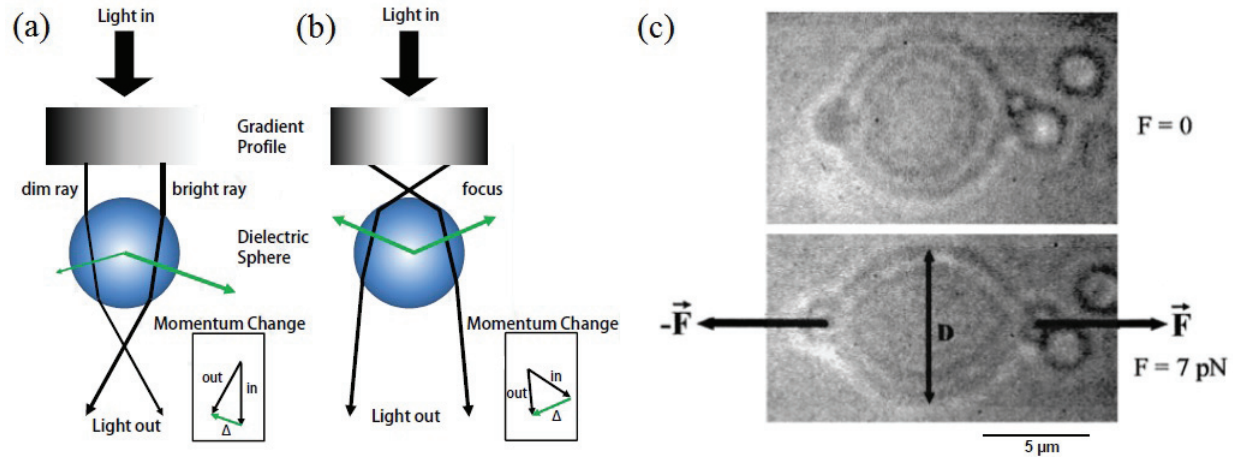

Figure 3.6: Schematic representation of: (a) optical tweezer setup configuration for particle displacement using a gradient of light, (b) trapping effect of a gaussian distribution of light on a microbead. (c) Microscopic images illustrating a RBC with two microparticles diametrically attached to its membrane, (top) at rest. (bottom) during stretching induced by the displacement away from each other of the microbeads, from [20]. The change in RBC diameter allows the estimation of its elastic or shear moduli.

3.2.4 Magnetic twisting cytometry (MTC)

Magnetic twisting cytometry (MTC) is based on the application of static and oscillating magnetic fields on ferromagnetic microbeads attached to the surface of the cell [64]. Under the effect of the applied magnetic field, the microbeads react by translating or rotating, thus applying a torque to the membrane of the cell it is attached to. The movement of the beads is recorded and analysed, enabling then to extract the mechanical parameters of the membrane [65].

This technique was applied to the mechanical characterization of RBCs by Marinkovic et al. [65]. The authors report the measurement of a complex elastic modulus g^* defined as

$$g^* = g' + ig'' \tag{3.8}$$

where g' is the storage modulus (real part) and g" is the loss modulus (imaginary part) defined as:

$$g' = (\Delta T_m/\Delta d)cos\Phi \tag{3.9}$$

and:

$$g" = (\Delta T_m/\Delta d)sin\Phi = 4A/\pi\omega\Delta d^2 \tag{3.10}$$

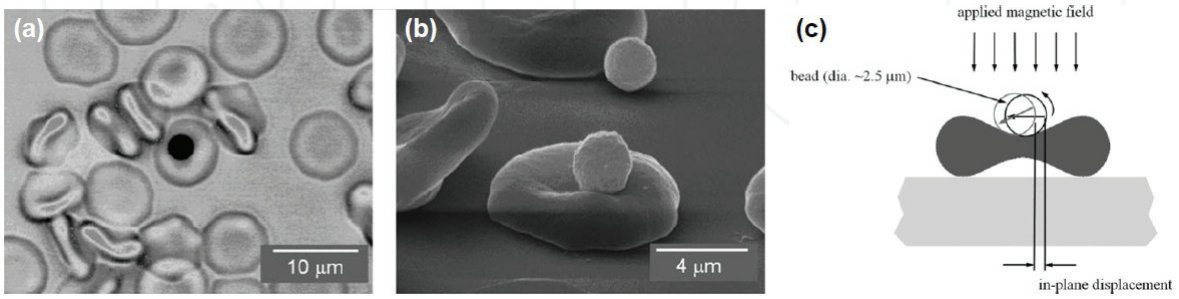

Figure 3.7: (a) Microscopic and (b) scanning electron microscopic images of a magnetic bead attached to the membrane of a RBC to perform magnetic twisting cytometry. (c) Illustration of the principle of the MTC. From [65].

with ΔT_m, the mechanical twist applied to the bead, Δd, the translational displacement of the microbead, ω, the radian frequency and Φ, the phase difference between the stress and the response. By scanning a frequency range from 0.1 to 100 Hz, the authors found that the storage modulus is independent of the frequency of stress and is equal to $\sim 10^{-3}$ Pa/n.m at, while the loss modulus increases with the frequency according to a power law of 0.64 with increasing frequency. RBC parameters were measured in raw units (Pa/n.m) which need a model of membrane deformation to be converted to traditional RBC moduli [65].

Magnetic twisting cytometry requires the bonding of a unique magnetic microbead to the RBC surface, as well as the precise monitoring of the magnetic field applied. Moreover, it has a low acquisition rate. Therefore, this technique is hardly compatible with a diagnosis application.

3.2.5 Study of cell membrane thermal fluctuations

Because the bending modulus B of biological membrane is usually small (of the order of a couple of $k_b T$), the curvature of the cellular membrane can be changed easily, leading to the apparition of thermal fluctuations. The dynamic fluctuations of cellular membrane consist in submicrometric displacements of the cell envelop, which are directly linked to the deformability of the cell, thus making it possible to extract its mechanical properties [66]. The observation of membrane fluctuations of a RBC can be carried out by several optical techniques. For example, the quantitative phase imaging (QPI) relies on the phase change of a laser beam as it passes through the cell, optically denser than the surrounding medium, using the principle of interferometry (Figure 3.8-b). Similarly, phase diffraction microscopy (PDM), which is a highly stable technique derived from the QPI, allows the measurement of dynamic spatiotemporal fluctuations of the membrane [67].

The measurement of these fluctuations, combined with a mathematical model [20], makes it possible to measure: the RBC shear modulus μ = 7.5 ± 2.5 µN.m^{-1} [67], its curvature modulus B = 10 $k_b T$ (~ 10-22 J) [68], as well as the extension modulus of its membrane, k = 0.02 mN.m^{-1}) [69, 70].

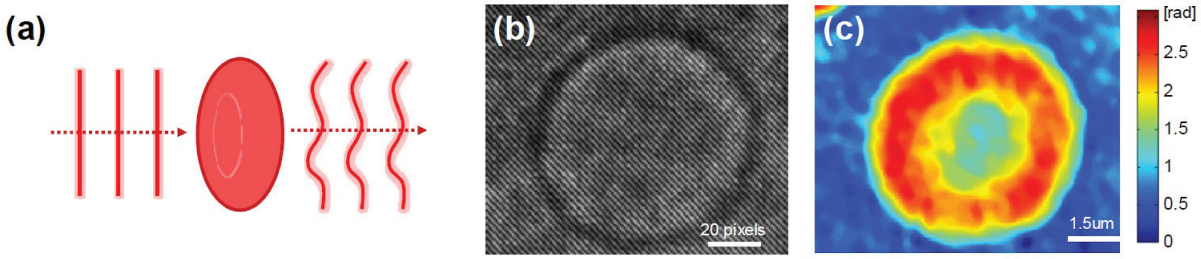

Figure 3.8: (a) Schematic illustration of the principle of quantitative phase imaging to visualize thermal fluctuations of the RBC membrane. (b) An example of an interferogram obtained on a RBC and (c) the corresponding phase image calculated by phase diffraction microscopy. From [20].

Single-cell techniques require bulky equipments and qualified staff. Some of these techniques (magnetic twisting cytometry, optical or magnetic tweezers, etc...) require the integration of colloidal probes on the cell membrane, which adds an additional step and complicates their automation. But their main drawback is their low analytical throughput which makes them hardly compatible with an application in the domain of medical diagnosis.

3.3 Microfluidic techniques

The development of microfluidics for cell deformability measurements combines the advantages of single-cell methods while treating a large population of cells in a reduced time. This approach has also the advantage of providing biomimetic environment, for example by reproducing as well as possible the physiological conditions of the RBC flow in the blood microcirculation. In this section, we present the wide variety of experimental biophysical assays, using fluidic microsystems and micro-electro-mechanical systems (MEMS), that have been reported in the literature to probe the deformability of living cells (RBCs and other cell types). Advantages and limitations of current systems and strategies to overcome the latter are then discussed.

As stated earlier, microfluidic techniques can be divided into two categories. The active ones that relies on the application of an external field force to manipulate or deform cells, the field force can be either electric [71], optical [61] or even by the use of ultrasounds [63]. We can also find the passive ones, based on use of the geometry of the channel and the associated hydrodynamic force to mechanically probe cells. These techniques can be applied to static [62][63] or flowing cells [61], allowing the study of a large population of cells in parallel or in series, respectively.

3.3.1 Active microfluidic techniques

3.3.1.1 Optical stretcher

Guck et al. [72] have developed a microfluidic automation of the optical tweezers, the device was called the optical stretcher. It is constituted of a two-beam laser trap in a microfluidic channel designed to serially deform isolated cells as they flow across the optical field (Fig. 3.9a). The stretching forces to which cells were individually exposed were in the range of 200-500 pN, which is still not sufficient to produce large deformations. Using optical forces, the technique was sensitive enough to detect changes in deformability between cancerous (MFC-7), metastatic (modMCF-7) human breast epithelial cells and even non-malignant (MCF-10) [72]. The technique throughput was relatively high (1 cell/min), neverthless, it remains far from the practical throughput. The technique advantage was its ability to perform mechanical phenotyping of cells without any contact or modifications. The elasticity of malaria infected RBCs (iRBCs) was measured by the same group using this optical stretcher [73]. The throughput of the technique was enhanced comparing to the conventional single-cell version, while maintaining the selectivity and sensitivity of single-cell elasticity measurements. The cells exposure to the laser beam during stretching may be considered as a drawback of the technique, however, the short residence time of cells in the beam path minimizes their exposure.

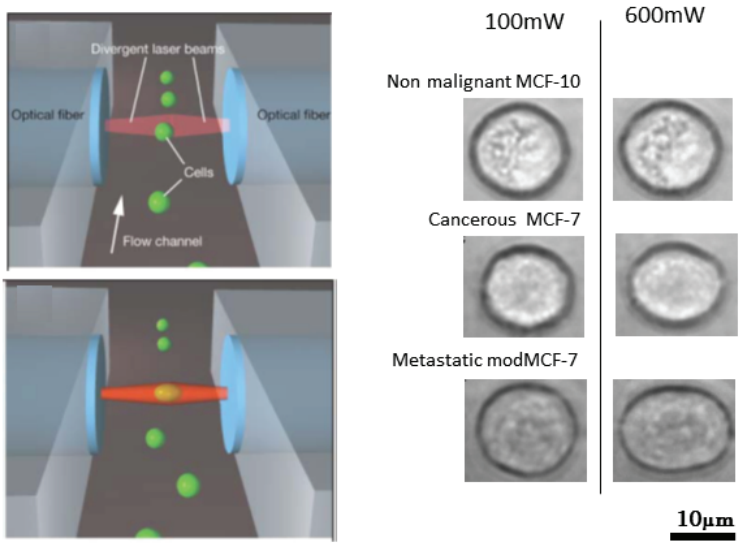

Figure 3.9: Visual representation of the working principle of the optical stretcher showing elongation of cells crossing the optical field. Micoscopic images of different cellular types elongations at different optical field intensities. Adapted from [72].

3.3.1.2 Electrodeformation

Shear elastic modulus and viscosity of plasma membranes of healthy RBCs (hRBCs) can be evaluated using the transient deformation of cells in a high-frequency electrical field [74]. Obtained estimations, based on analytical models or numerical simulations, of hRBCs shear modulus and membrane viscosity ($\mu = 6.1.10^{-6}$ N/m and $\eta_m = 3.4.10^{-7}$ N.s/m, respectively)showed a good agreement with the micropipette results of Evans et al. [75]. The deformability of individual eucaryotic cells was also quantified using electro-deformation [62, 76]. The technique was used on RBCs with an enhanced throughput[77]. Authors used an array chip of single-cell microchambers to trap and deform individual RBCs (Fig. 3.9-a), typical sequence of deformation of a RBC in an electrodeformatio assay is shown on Figure. 3.9-b. To perform electro-deformation the cells need to be suspended in a buffer of low conductivity. Such type of buffers lead to rapid ageing of the cells [74], and constitutes an additional step to the sample preparation which may be seen as a drawback of the technique.

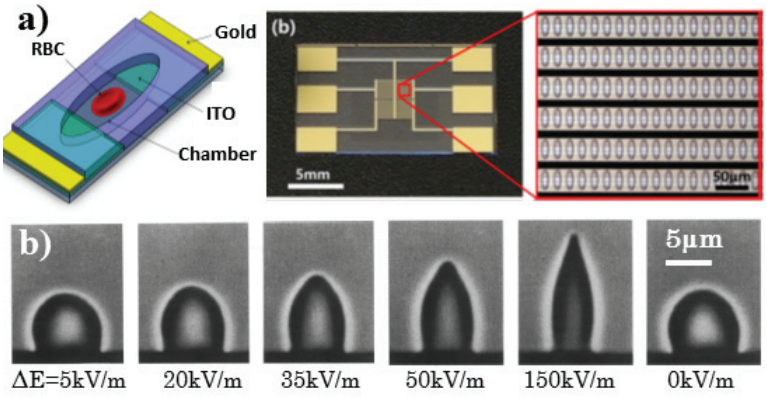

Figure 3.10: . (a) Schematic view and pictures of the single-cell microchamber array device for mechanical characterization of RBCs, from [77] (b) Microscopic images of an electrodeformation experiment showing the deformation state of RBCs elongated at different applied electrical field intensities [74].

3.3.1.3 Compression experiments

The compression experiments principle relies on the study of the deformation and relaxation of cells initially placed beneath an actuated flexible membrane (Fig. 3.11). When the membrane is actuated the cells get deformed before relaxing back to their stationnary shape when the compression is stopped. The quantification of cells relaxation times τ allows the discrimination of two different cell types (neutrophiles and fibroblasts) known to have different cytoskeletal structures [78]. To our knowledge, this type of experiments has not been used on RBCs, however, we do not perceive any limitation to such application.

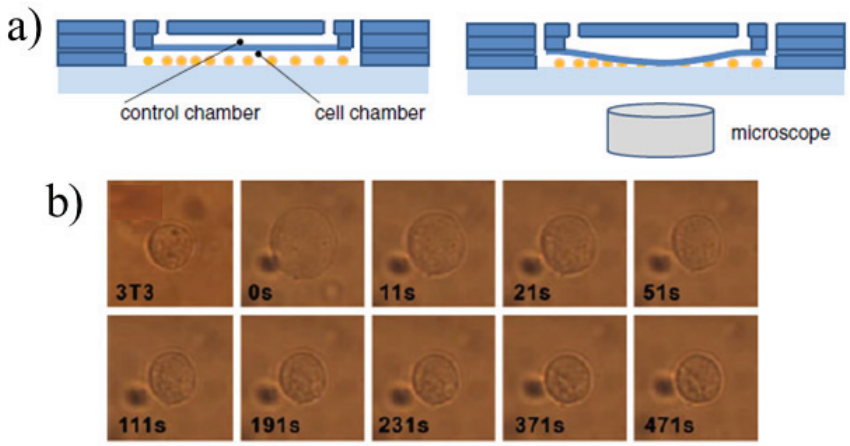

Figure 3.11: (a) Schematic reprsentation of the compression assay setup. Cells are compressed by the deflection of the flexible membrane induced by the pressurization of the control chamber. (b) Microscopic pictures showing the shape relaxatio n process of 3T3 cells when the compression is ceased. Adapted from [78].

Micro Electro Mechanical Systems (MEMS) have been used to perform compression experiments and study cell deformation [79, 80]. Such experiments usually use the controlled displacement of a moving actuator to compress the cell against a fixed part. For example, yeast cells deformability has been studied by Barazani et al. [80]. Authors developed an AC driven electrothermal micro actuator to compress the cells against a reference back spring. Cell stiffness relative to the reference spring constant is obtained by estimating the ratio between the motion of the reference spring and cell deformation. Authors reported values of yeast cells average stiffness of 9.3 ± 3.1 N.m^{-1}, they also reported yeast cell's membrane fracture for forces around 0.47 ± 0.1 µN. Gnerlich et al. [79] performed compression experiments on NIH 3T3 mouse fibroblasts using an equivalent MEMS equiped with a calibrated piezo-driver. They reported the decrease of the associated forces (38 nN to 5 nN) during the compression, such behavior is well described by a visco-elastic cell model. Lafitte et al. [81] developed the use of silicon nanotweezers (SNT) to evaluate the mechanical properties of biological samples (DNA and cells). Basically, the sample undergoes a periodic solicitation by fixing one tip of the tweezer and alternatively opening the opposite one. The changes of the resonance frequency of the SNT are directly linked to the added rigidity and viscosity of the cell. Consequently, the mechanical properties of the cells can be estimated in real-time by monitoring the evolution of this frequency. Despite their use on a single cell level, the use of MEMS for the mechanical phenotyping of large populations of cells is still to be demonstrated.

3.3.2 Passive microfluidic techniques

Fluid-based deformability assays, which are perhaps the simplest methods to measure cellular mechanical properties while achieving high-throughput, rely on the monitoring of cell deformations

as they flow through microfluidic channels. Cellular deformability can be challenged either by the walls of the device or by the associated shear stress without any contact, thus limiting the impact of cell membrane adhesion with channel boundaries.

3.3.2.1 Fluid stretching

RBCs are highly deformable and their deformability can therefore be challenged using shear stress generated by microfluidic channels wider than the typical size of the cell. Forsyth et al. [82] have studied the effect of RBC rigidification on their behavior under flow in a microchannel with a larger diameter than their typical cell size. They reported different dynamic behaviors of RBCs in a pressure-driven flow, according to the shear rate: tumbling [2], tanktreading [3], swinging [4] and stretching (Figure 3.12-a). Upon chemical treatment with glutaraldehyde, which is known to rigidify both cell membrane and cytoplasm, RBCs presented lower deformation and increased occurrence of tumbling, which is a motion typical of rigid bodies. They also measured an adimentionalized strain rate, $\dot{Y}$ defined as:

$$\dot{Y} = \Delta L / \Delta t L_{in} \dot{\gamma} \tag{3.11}$$

where ΔL is the change in length of the RBC, L_{in} being its initial length, $\dot{\gamma}$ is the shear rate and Δt is the time of change in length.

Ỳ obtained from healthy RBCs is compared with measurements performed on rigidified samples using two different chemical treatments: glutarhaldehude (GA), which is a non-specific stiffener and diamide, which acts only on the cytoskeleton. They found that the GA rigidified RBCs (GA-rRBCs) show a deformation rate lower than that of the control (Figure 3.12-b); the difference being less significant for the diamide rigidified samples. They concluded that the viscosity of the cytoplasm and/or the lipid bilayer has a dominant effect on the dynamic response of the RBC.

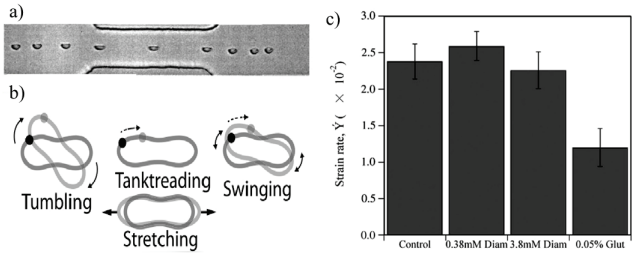

Figure 3.12: (a) Sequence of deformation of a RBC flowing through the constriction. (b) The different types of movements undergone by a RBC under confined flow, according to its mechanical properties. (c) Strain rate Ỳ measured for healthy RBCs, as well as chemically rigidified RBCs with diamide and gluraraldehyde. Adapted from [82].

[2] Tumbling is a solid rotation-like motion.

[3] Tanktreading corresponds to the motion of rotation of the membrane around the cytoplasm.

[4] Swinging describes the motion of tanktreading associated with oscillations of the RBC main orientation.

Lee et al. [83] reported the monitoring of RBC deformation in a hyperbolic converging microchannel. They showed that the extensional flow is more efficient to induce cell deformation than a shear flow, as RBCs presented deformation index of 0.51 and 0.29 at 3 Pa, in extensional and shear flow respectively. Such approach was used to detect the decrease in deformability of RBCs following heat treatment. Gosset et al. [84] proposed an automated microfluidic tool using inertial focusing to uniformly deliver cells to a stretching extensional flow (Fig. 3.13-a) where cells are deformed at high strain rates (Fig. 3.13-b). They characterized the deformability of populations of leukocytes and malignant cells in pleural fluid samples. They predicted disease state in patients with cancer and immune activation with a sensitivity of 91% and a specificity of 86% at high throughput (~ 2000 cells/s). Both lymphocyte activation and stem cell pluripotency were found to be associated with increased deformability [84].

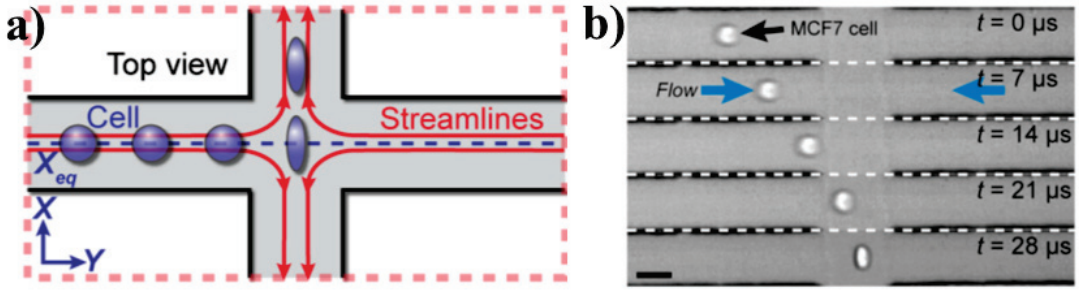

Figure 3.13: (a) Schematic representation of the principle and (b) deformation sequence of an MCF7 cell being stretched when entering the extensional flow region, adapted from [84]).

Tomaiuolo et al. [85–88] reported the study of the transient time necessary to the RBC, initially at rest in a capillary of about 8 µm in diameter, to adopt a stationary shape during the start-up flow as illustrated in Figure 3.14. At rest, the cell undergo a biconcave shape and deform to adopt a parachute-like shape (Figure 3.14-a) while moving. The authors have evaluate i_o and i which are respectively the mean gray level of the cell body at rest and during start-up flow and Δi, the maximum variation of gray level during the acquisition of the steady shape. Then, they estimated the transient time associated to the shape evolution, which can be assimilated to the RBC shape relaxation time τ, by calculating the characteristic time of the exponential evolution of $(i\text{-}i_o)/\Delta i$ as a function of time (Figure 3.14-b). They reported typical relaxation time τ of ~ 0.1 s which is in good agreement with values from literature, measured by micropipette aspiration [27]. They also demonstrated that glutaraldehyde stiffened RBCs showed faster relaxation time and lower stationnary deformations, as already reported by ektacytometry [49].

Prado et al. [89] used the same approach to study experimentally and analytically the relaxation time of RBCs. They correlate the characteristic time necessary to reach a steady shape during start-up flow with the characteristic time to reach a steady speed, assimilated to the RBC relaxation time. The authors demonstrated that τ depends on both the buffer velocity and its viscosity. Indeed, they reported a linear relationship of $1/\tau$ as a function of the buffer velocity and the decrease of

τ with increasing outer viscosity as presented in Figure 3.14-c. Moreover, they revealed as showed in Figure 3.14-d that diamide-treated RBCs experience a shorter relaxation time than their healthy counterpart as previously reported in literature [49]. Thanks to their analytical interpretation of the experimental data, they reported an estimation of the effective membrane viscosity η_{mem} = 10^{-7} N.s.m^{-1} [36]. They explained the difference with previously published values (~ 0.5-1.10^{-6} [27, 85]) by the fact that they take into account both the viscosity of the surrounding buffer and the cytoplasm which are usually neglected, the viscous effect being predominantly attributed to the membrane viscosity.

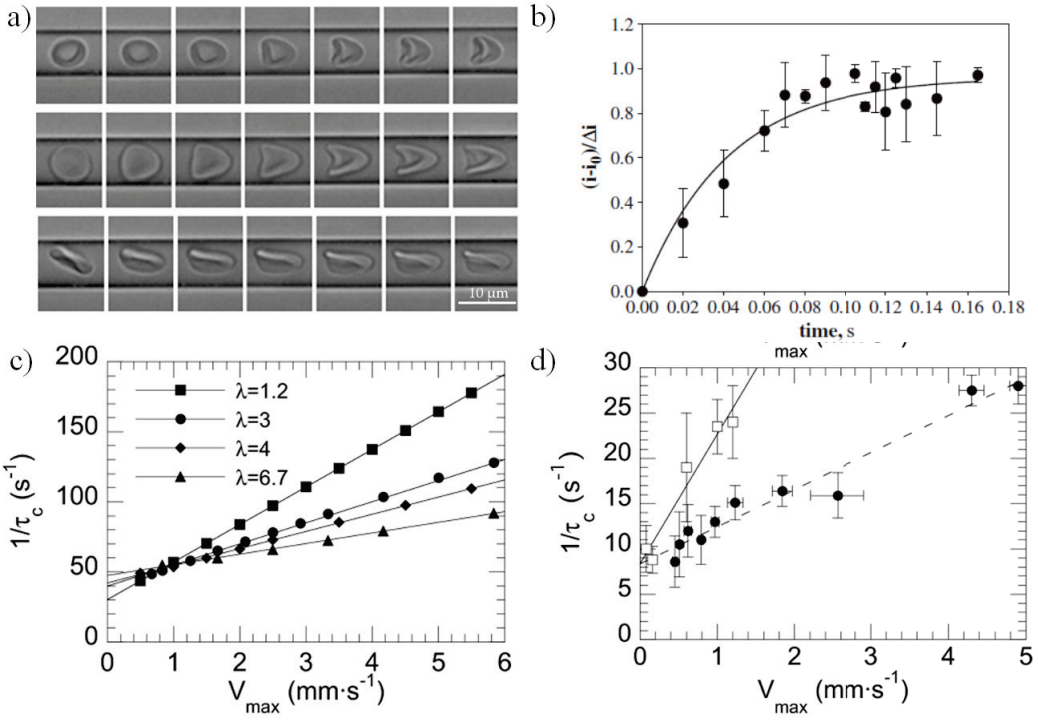

Figure 3.14: (a) Sequences of deformation of three RBCs initially at rest, in a capillary of about 8 µm in diameter, to adopt a stationary shape during the start-up flow. (b) Evolution of the grey level traducing the RBC shape as a function of time. From [85]. (c) Computed and (d) experimental evolution of $1/\tau$ versus the maximum flow speed for different buffer viscosities. (d) (solid circles) correspond to PBS and (open squares) to PBS + 10%w Dextran 40kDa. (d) $\lambda = \eta_{in}/\eta_{out}$, where η_{in} and η_{out} are the RBC internal and the external viscosities respectively. From [89].

3.3.2.2 Constriction channels

A simple and powerful mean to probe cell deformability can be through the study of their flow inside capillaries with typical sizes smaller than those of the cell. While using readouts such as the transit time, deformation index or relaxation time. Several designs of geometric restrictions have been reported in the literature to probe cell mechanical phenotype. For instance, Selby et al. [44] developed a design with geometrical constrictions ranging from 2 to 8 µm in width using a pressure drop flow in

order to discriminate malaria infected from healthy RBCs. Authors concluded that infected RBCs clogged when entering smaller constrictions as parasites develop within the host cell increases their rigidity. Fig. 3.15-a shows the clogging of a 6 µm wide channel by schizontes infected RBCs, whereas a hRBC (in red) manages to deform past the barrier formed by diseased cells.

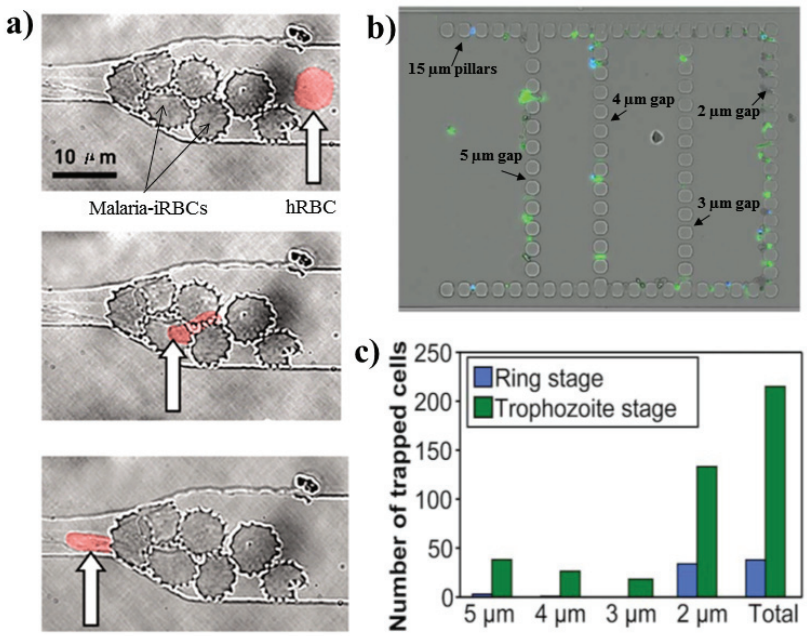

Figure 3.15: (a) Video-microscopic images of malaria infected RBCs clogged at the entry of a geometric constriction, images show a healthy cell (in red) able to deform past the clogging. Flow is from right to left. From [44]. (b) Illustration of the deformability-based separation of malaria infected RBCs at different maturation stage of the parasite. Depending on their stiffness, iRBCs clogg at different dimensions of the . (c) Quantification of the number of cells trapped in the device according to the spacing between the pillars for the two populations. Adapted from [90].

The dynamic behavior of RBCs flowing through arrays of 15 µm pillars, either slowly through 5 to 2 µm wide gaps or rapidly along 10 µm wide channels has been studied [90]. Authors observed that mechanically impaired RBCs - either due to heat treatment, issued from malaria infected samples or from patients with hereditary spherocytosis - tend to accumulate in narrow slits more frequently than normal RBCs, hence demonstrating their increased rigidity (Fig. 3.15-b). Similarly, Bow et al. [91] monitored dynamic mechanical responses of 10^3 to 10^4 individual RBCs using converging or diverging obstacles (Fig. 3.16-a). They experimentally demonstrated that differences in deformability - demonstrated by differences in transit velocity - of gluraraldehyde treated or malaria infected RBCs, are enhanced in geometries with sharper corners, for a given pressure difference (Fig. 3.16-b); the difference between the transit speeds of the different populations being more pronounced using divergent obstacles. The influence of an anti-malaria drug (Artesunate) on the dynamic deformability

of ring-infected RBCs was also evaluated [92]. After Artesunate treatment, they observed a 50% decrease in the transit velocity of iRBCs whereas only 10% in speed reduction is observed for hRBCs.

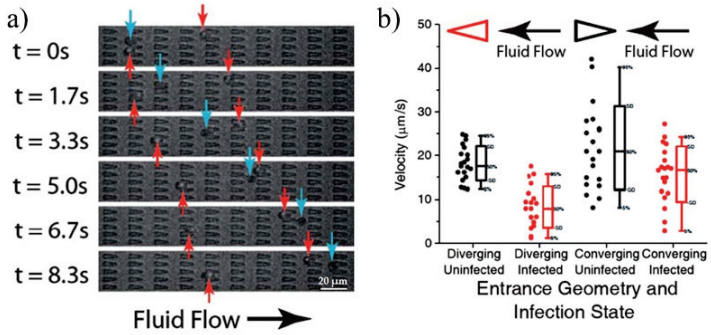

Figure 3.16: (a) Time-lapse images of (red arrows) ring stage infected RBCs and (blue arrows) healthy RBCs, flowing in the device. The hRBC travels faster than the infected ones for the same pressure gradient of 0.24 Pa.µm^{-1}. (b) Transit velocities of (black) normal and (red) parasited RBCs in a network of obstacles. From [91].

Braunmüller et al. [93] have studied the relaxation times of RBCs flowing out of a microchannel (Figure 3.17-a). They reported the existence of two relaxation times. The first relaxation time τ_1 corresponding to the time necessary to change from the compressed shape inside the microchannel to adopt the parachute-like shape which ranged from $0.11 < \tau_1 < 0.52$ s. The second time $\tau_{1/2}$, corresponding to the time necessary to deform from the parachute-like shape to the discoidal shape which was measured to be ($9 < \tau_{1/2} < 49$ s). They found that the two times vary linearly with respect to each other. The authors then studied the effect of ATP on the deformability of RBCs and showed that the depletion of ATP significantly reduces the deformability of the cell cytoskeleton and consequently decreases the relaxation times [93].

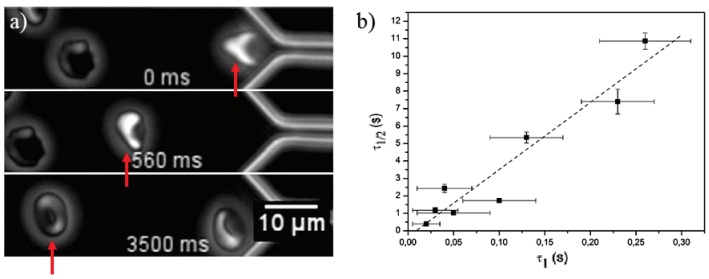

Figure 3.17: (a) Videomicroscopic recording of the two relaxation phases of a RBC (red arrow) flowing out of a microfluidic constriction. First, the cell deforms from the compressed shape inside the constriction to the parachute-like shape in a characteristic time τ_1. Then it relaxes from the parachute-like shape to its native discoidal shape in a characteristic time $\tau_{1/2}$. Flow is from right to left. (b) Measurements of the two relaxation times $\tau_{1/2}$ and τ_1 on RBCs submitted to various conditions of ATP depletion, reveals a proportional relationship between the two timescales. Adapted from [93].

3.3.2.3 Pressure drop measurements

The passage of individual cells in confined microchannels is linked to pressure-drop variations. To probe these fluctuations, Abkarian et al. [94, 95] proposed a high-speed microfluidic approach. The microfluidic system is constituted of two identical channels (Fig. 7.2-a) that merge into one single channel on the right side of the chip. The cell suspension is injected in the upper channel whereas a solution of contrast agent is injected in the lower one. The monitoring of the co-flow interface at the exit allows the visualization of the pressure drop in the microchannel containing the cells. When the upper channel is empty $i.e$ no flowing cells, the pressures in the two channel are equivalent and the virtual interface is centered. In contrast, when a cell flows in the upper channel, the local pressure is modified by adding an additional resistance to the channel and the interface at the exit is shifted. The shift of the interface can be converted into a pressure drop measurement through a calibration curve. Authors have shown that both the volume and the deformability of the studied cells impact the amplitude of the pressure drop (Fig. 7.2-b). Examples in literature showed that this technique is able to discriminate WBCs from RBCs, as well healthy and chemically-rigidified RBCs [94]. Using this approach, mechanical properties of healthy and cancerous brain cells have also been characterized by Khan et al. [96].

Authors reported that brain tumor cells have a slower entry time than their healthy counterparts, thus suggesting that the well-spread idea that cancer cells are more deformable than benign cells may not apply to brain cancer cells [96].

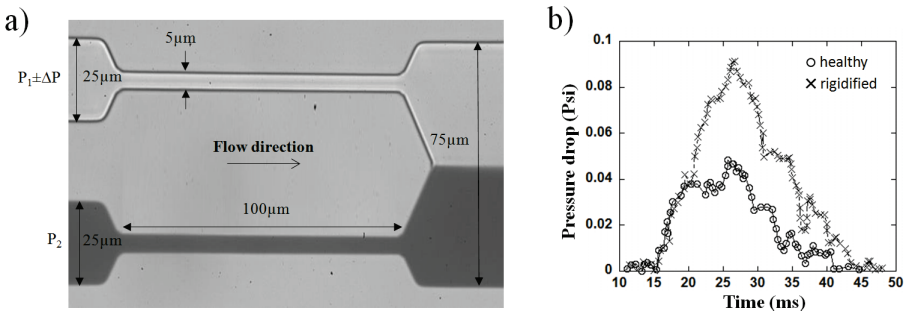

Figure 3.18: (a) Microscopic image of the pressure drop measurement device with its respective dimensions. The fluctuations of the virtual interface are converted to pressure drop measurements through a calibration curve (b) Measured pressure drop versus time for (×) a hRBC and (○) a rigidified RBC after 0.001% glutaraldehyde treatment. Adapted from [95].

3.3.2.4 Microfluidic micropipette aspiration

Guo et al. [97] proposed an adaptation of the conventionnal micropipette aspiration technique into microfluidic format. Figure 3.19-a presents the geometry of the microfluidic micropipette aspiration device implementing multiple funnel-shaped constrictions with openings ranging from 5 down to 1 µm. As a cell is flowing in the device, it gets trapped at the nozzle of a funnel, the pressure difference is manually increased until the RBC is allowed to squeeze past the restriction. The threshold pressure

is used to determine the intrinsic stiffness of each cell, using the same mathematical model as in conventional pipette aspiration technique - *i.e.* considering the RBC as a Newtonian liquid-drop with constant volume - allowing extracting the cell cortical tension T_c.

$$P_{treshold} = T_c \left(\frac{1}{R_a} - \frac{1}{R_b} \right) \tag{3.12}$$

with $P_{treshold}$, the pressure gradient to be applied to cause the cell to flow through the funnel restriction, R_a and R_b, the front and rear radii of curvature of the RBC as it passes through the geometric constriction, respectively.

The same principle was used by Myrand et al. [98] in another embodiment of the same approach, using a parallelization of several channels in order to ensure that the same pressure is applied to all the cells. Then an oscillating pressure is applied at the entry of the system and the threshold pressure (refered to as normalized pressure) necessary for the passage of the RBC is measured. Both variants were tested with healthy and glutaraldehyde rigidified RBCs at various concentrations. They showed that both T_c and the normalized pressure increased with the glutaraldehyde concentration. Indeed T_c is found to be 3-fold higher and the normalized pressure is two-fold higher, for 0.003% GA-rRBCs than for hRBCs (Fig. 3.19-b.c). Finally, malaria infected RBCs by early (ring) through late (schizont) developmental stages of the parasite were shown to be 1.5 to 200-fold stiffer than uninfected cells (Fig. 3.19-d) as already reported in literature [99]. However, the rectangular cross-section of the geometry can rise some concerns about the validity of applying conventional micropipette models to retrieve cellular mechanical properties.

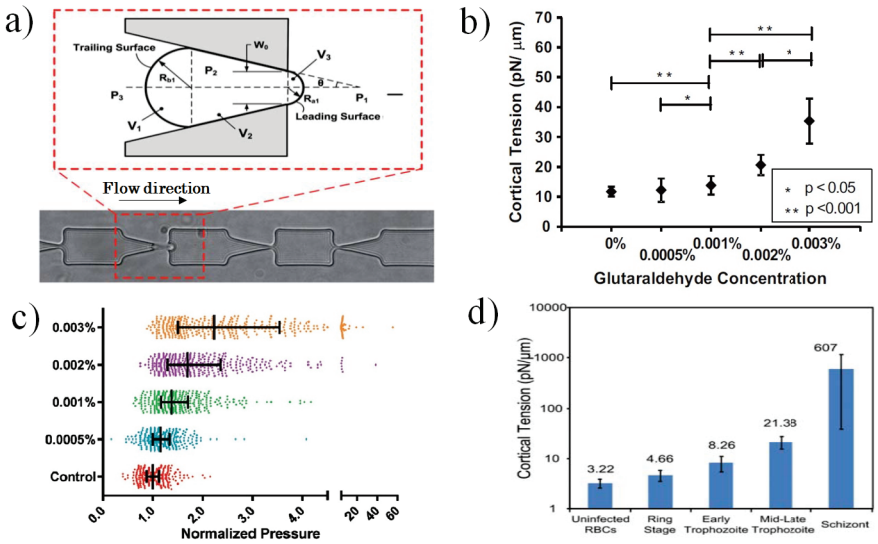

Figure 3.19: (a) Image illustrating a RBC being deformed when passing the funnel constriction and the associated geometric model. (b) Evolution of the cortical tension versus the concentration of glutaraldehyde used to rigidify RBCs, from [100]. (c) Normalized pressure necessary for the passage of RBCs in the funnel restriction for various concentrations of glutaraldehyde used to rigidify the cells, from [98]. (d) Cortical tension of hRBCs and malaria-infected RBCs in various stages of infection. From [97]

3.4 Assessment

Throughout the previous sections, we highlighted various experimental techniques developed to probe RBC mechanical properties. Microfluidic techniques seem to be the most promising ones as they allow single cell measurements while remaining reasonably compatible with the high throughput needed for POC applications and automation. Among these microfluidic techniques, some have never been applied to the characterization of RBC mechanical properties.

The following table 3.1 summarizes the different mechanical characterization techniques and the associated RBCs mechanical parameters or readouts when reported in literature:

	Collective techniques	Micropipette	AFM	IQP	CTM	Optical tweezers	Passive microfluidics
Membrane viscosity[N.s/m]	10^{-6}	$0.6-1.10^{-6}$					6.10^{-6}
Cytoplasm viscosity[mPa.s]	3.5						
Shear modulus [$\mu N/m$]		9 ± 1.7		7.5 ± 2.5		2.5 ± 0.4	√
Bending modulus [k_bT]		43.5	√	7.5 ± 2	√		
Stretching modulus [mN/m]		300-500		0.01-1		√	
Young modulus [kPa]			4.4 ± 0.6				
Deformation index	√						√
relaxation time / Transcient flow time [ms]	√	100 ± 30	√		√	206 ± 100	300 ± 200
Cell speed							√

Table 3.1: Summary of the different techniques used in the measurement of RBCs mechanical properties with the various parameters and readouts measured.

As it can be seen from table 3.1, some measurements can vary significantly when measured with one technique or another, depending on the amplitude of the stress and its duration. For example, the extension modulus can vary by a factor 10^4 depending if it is measured using micropipette aspiration or IQP. These two techniques sample mechanical responses of the RBC under very different loading conditions and they involve different components of the cell [20]. Another challenge that still need to be addressed is the translation of raw parameters such as relaxation time or deformation index into cellular intrinsic mechanical characteristics such as Young's modulus or cortical tension. Indeed, intrinsic deformability parameters are independent of the setup (viscosity, flow speed, etc...) and allow the comparison of data obtained with various techniques and by various research groups. Therefore there is a strong need for theoretical framework and mechanical modelling of the cellular response in order to extract intrinsic mechanical properties.

CHAPTER 4

MATERIALS AND METHODS

Contents

In this chapter, the different materials and methods used in the experiments are described. It includes the preparation of the solutions and blood samples, the fabrication of polydimethylsiloxane (PDMS) microfluidic channels for passive experiments and the protocol developed to obtain ITO electrodes used in electrodeformation (ED) assays. The two experimental setups for microfluidic and ED experiments are presented and finally we detail the different image analysis routines developed for cell detection.

4.1 Solutions and blood samples preparation

Unless otherwise stated, all chemicals were obtained from Sigma-Aldrich® (St. Louis, MO, USA) and used as received without further purification.

4.1.1 Solution preparation

a) PBS solutions: For passive microfluidic experiments, Phosphate-Buffered Saline (PBS) was used as buffer. PBS 10x was purchased from Biosolve chemicals BV and diluted in sterilized deionized water to obtain a PBS 1x solution (300 mOsmol/kg, pH=7.4). In order to prepare solutions with various viscosities (PBS/Dextran solutions), Dextran polymer ($M_w = 2 \times 10^6$ g.mol^{-1}) was diluted in PBS 1x.

The Dextran concentration was varied to obtain different buffer viscosities, η_{out}, ranging from 1.3 to 31.5 mPa.s. The viscosities of the different solutions were measured using a Brookfield ® viscometer (LVDV-I), and are presented in Table 4.1.

Dextran concentration in PBS (% w/v)	0	1	4	7.5	9
Viscosity η_{out} (mPa.s)	1.30	2.8	8.6	20.3	31.5

Table 4.1: Viscosities of the different PBS/Dextran solutions as a function of Dextran concentration in PBS 1x buffer. Measurements were performed at room temperature.

PBS/Dextran/BSA solutions were obtained by dissolving Bovine Serum Albumine (BSA) 2% w/v in PBS/Dextran, this solution was used as an external buffer in passive microflow to avoid cell adhesion to the microchannel walls.

b) Glu/Suc solution: Electrodeformation experiments need to be performed in very low conductivity solutions, while maintaining an osmolarity compatible with biological cells. Thus, we used an aqueous solution containing glucose and sucrose (16.7 mmol/L and 255.6 mmol/L respectively [101]) diluted in sterilized deionised water as an external medium. Parameters characterizing this solution are presented in Table 4.2. The external medium viscosity was also varied through the dissolution of Dextran in this Glu/Suc solution to obtain Glu/Suc/Dextran solutions and thus reach viscosity values of 16.4 and 31.5 mPa.s.

Conductivity σ	2 µS.cm^{-1}
pH	7.4
Viscosity, η_{out}	1.3 mPa.s

Table 4.2: Physical properties of the Glucose/Sucrose (Glu/Suc) solution. The viscosity was measured at room temperature.

Prior to each use, all solutions (PBS 1x, PBS/Dextran, PBS/Dextran/BSA, Gluc/Suc and Glu/Suc/Dextran solutions) were filtered using a 0.2 µm pore filter.

4.1.2 Blood sample preparation:

4.1.2.1 Healthy RBCs (hRBCs)

For the preparation of blood samples, 30 µL of fresh whole blood was obtained from healthy volunteers by finger prick and diluted in 970 µL of PBS 1x solution. The obtained suspension was then centrifuged to isolate RBCs from other blood components. After centrifugation, supernatant was withdrawn and hRBCs were re-suspended in 1 mL of PBS 1x. This washing step was repeated three times in order to wash the cells and so avoid coagulation. Finally, the washed hRBCs were

re-suspended in 1mL of PBS 1x to constitute the mother solution (M) at a cell concentration ~ 150.10^6 hRBCs/mL.

a) Passive microfluidics samples: Starting from the mother solution prepared as explained above, a diluted suspension of hRBCs (~ 19.10^6 RBCs/mL of PBS) was obtained by adding 125 µL of M in 875 µL PBS 1x. This dilution was necessary to avoid the flow of several cells simultaneously in the microchannel. This solution was centrifuged and the cells were finally suspended in the PBS/Dextran/BSA solution, corresponding to the desired viscosity.

b) Electrodeformation samples: For the ED experiments, we used a more diluted suspension than in microfluidics experiments (4.10^6 RBCs/mL of Glu/Suc). This solution was obtained by adding 30 µL of M in 970 µL of PBS 1x. After centrifugation, the supernatant was removed and replaced by 1mL of Glu/Suc solution. This high dilution was meant to avoid the attraction of excessive numbers of RBCs on the border of ITO electrodes in order to study single hRBCs. To investigate the influence of the surrounding medium viscosity, this last step was done by replacing the 1 mL of Glu/Suc solution by 1 mL of Glu/Suc/Dextran solution at the targeted viscosity.

4.1.2.2 Rigidified RBC samples

To test the impact of the modification of cell mechanical properties, rigidified samples (rRBCs) were prepared and compared to healthy samples (hRBCs). Two rigidification processes were tested: a chemical treatment with Glutaraldehyde and a thermal heating one.

a) Glutaraldehyde (GA) process: GA is a known non-specific fixative, that acts on all the cell components, reducing its overall deformability [82]. To prepare GA rigidified samples (GA-rRBCs), 1 to 5 µL of GA solution (25% v/v) were added to 1 mL of a suspension of hRBCs prepared in PBS at a concentration of 19.10^6 RBCs/mL as described in section 4.1.2.1a. After mixing, the solution was then incubated for 5 min at room temperature. Afterwards, the cells were washed 3 times in PBS 1x and finally resuspended in 1 mL of PBS/Dextran solution. Experiments with GA-rRBCs were carried out only at η_{out} = 31.5 mPa.s and for passive microfluidic experiments.

b) Thermal heating process: Several articles in literature [83, 90] reported that heat treatment induces irreversible rigidificaton of RBC membrane. This decrease in deformability is likely due to a denaturation of its membrane proteins structure [102].
To prepare thermally rigidified samples (T-rRBCs) in PBS 1x, a hRBC suspension at the desired concentration depending on the type of experiment (either 19.10^6 hRBCs/mL for passive microfluidics or 4.10^6 hRBCs/mL for ED) was prepared in PBS/BSA solution (2% w/v). Then, the suspension was heated at $50 \pm 2^\circ$ C for 15 min in a thermal bath. After incubation, the solution was left for 3-5 min to cool down to room temperature, the suspension was then centrifuged and the T-rRBCs were

re-suspended in 1 mL of desired solution Glu/Suc or PBS/Dextran depending on the experiment. Microscopic images of RBCs rigidified using both protocols explained above are presented in Fig 4.1 in comparison with a hRBCs sample. Images were taken using a ×40 magnification.

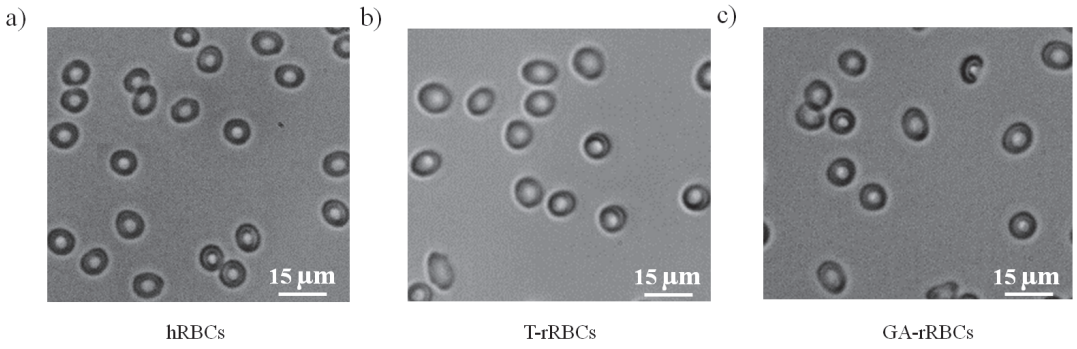

Figure 4.1: Videomicroscopic images of RBCs prepared according to the different rigidification protocols: (a) hRBCs, (b) GA-rRBCs at 0.125% v/v concentration, (c) T-rRBCs at 50° C for 15 min.

Recent studies in literature have pointed out a decrease in RBCs volume after a rigidification using the thermal heating process [90]. In order to check the impact of our rigidification protocol on the RBCs size, we performed measurements of cell projected surface area on the videomicroscopic images presented Figure 4.1. A mean projected surface area was calculated for the three samples using 15 cells per condition and is presented in Figure 4.2. We notice a small decrease yet not significant of rigidified RBCs projected surface area compared to the hRBCs sample. These results show that our rigidification processes does not affect significantly the cells volume. Any differences in behavior of the rRBCs compared to hRBCs (Chapter 7) will therefore be attributed to their mechanical properties and not their volumes.

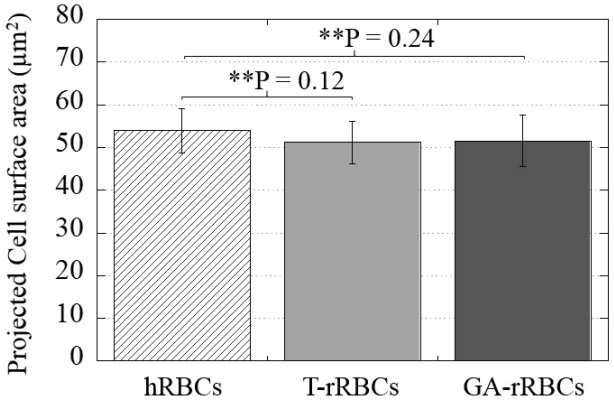

Figure 4.2: Measurements of RBCs mean projected surface area on microscopic images of hRBCs, T-rRBCs sample (50° C for 15 min) and GR-rRBCs sample (0.125% v/v).

4.2 Device fabrication

In the following sections, we will describe the protocols used for the fabrication of the devices used in the two approaches presented in this work: passive microfluidics and electrodeformation. First, we will explain the fabrication route used for the PDMS passive microfluidic channels. Next, we will detail the procedure developed to obtain the ITO electrodes used in electrodeformation experiments.

4.2.1 Channels for passive microfluidic experiments

PDMS microfluidic channels were prepared using standard soft lithography technique (replicate molding) [103]. First, a mold was prepared using laser lithography. Briefly, we spin-coated SU8-2005 photoresist (MicroChem®) on a silicon substrate to obtain a 5 µm thick layer. Next, we put the substrate at 95°C for 3 min to perform the soft pre-bake step. Then, a laser lithography machine (µPG 101 from Heidelberg Instruments®) was used to irradiate this photoresist layer. The lithography system is equipped with a diode laser at 405 nm operating at a writing speed of 5 mm^2/min. The focusing of the laser beam was automatically adjusted using the pneumatic function of the machine and the power was set at 70% of 10 mW (filter off). These parameters were optimized to obtain the most satisfying results in terms of patterning resolution of our channel designs. Subsequently to the laser exposure, we put the substrate at 95°C for 3 min to perform a post-bake step. Finally, we developed the patterned SU8 photoresist using Propylene Glycol Methyl Ether Acetate (PGMEA) solution for 1 min. The mold was silanized under vacuum for 3 h using Trichloro(perfluoro-octyl)silane to facilitate the demolding process. The mold was replicated in Polydimethylsiloxane (PDMS). Fluidic inlets and outlets were punched (diameter of 0.75mm) and then the PDMS slab was sealed on glass substrates. The sealing was realized by O_2 plasma bonding (Harrick Plasma®) for 3 min at 900 mTorr with 40 sccm O_2.

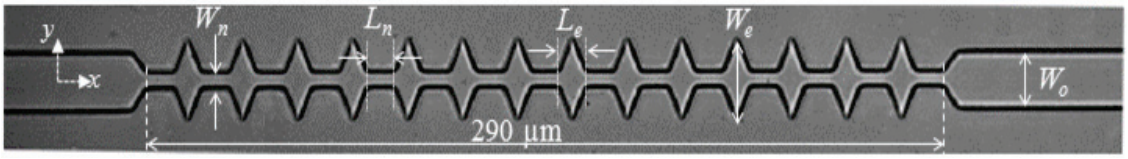

Figure 4.3: Microscopic image of the microfluidic channel used to study the relaxation of hRBCs under confined flow in Chapter 5. The dimensions are W_o = 15 µm, W_n = 5 µm, L_n = 10 µm, L_e = 10 µm and W_e = 25 µm.

Figure 4.3 illustrates a typical geometry used in Chapter 5 for the investigation of RBC mechanical response using a passive microfluidic configuration where the main width of the channel W_o was varied between 15, 25 and 50 µm and the height was set to 5 µm. In this geometry, referred to as the oscillating width channel (OWC), a succession of 14 tooth-like constrictions, each constriction combining a narrowing followed by a widening aperture, was implemented in the median part of the channel. The narrowing width W_n was set at 5 µm while the enlargement width W_e was at 25 µm. Both widening and narrowing lengths L_n and L_e were 10 µm. This specific design was

first used by M. Abkarian [95] and then F. Quemeneur [104] to study the flow of RBCs and lipid vesicles respectively. Multiple microfluidic channel geometries were investigated. Apart from W_o, they presented also various oscillating width constriction geometries. These geometries and their dimensions are presented in Appendix B and are used in Chapter 7.

To increase the number of systems per replication, we patterned several copies of the same geometry within the same wafer. However, differences in photoresist thickness can exist, especially radially, leading to a difference in channel height. For example, using profilometry, we measured a typical difference of 300 nm between the centered copy and the one positioned at the periphery of the wafer. Using 3-D Comsol Multiphysics® simulations, we estimated the sensitivity of the flow speed to variation in channel thickness. The simulations were performed using the geometry shown in Fig 4.3 with a main width W_o of 50 µm. Figure 4.4 shows that the flow speed component u (in the x-direction), represented here as a function of y, decreases by 10% from 210 to 190 µm.s^{-1} when we decreased the channel depth by only 300 nm. In order to avoid any bias induced by such depth difference, we decided to always use PDMS replicate obtained from the same structure on the wafer. By applying this restriction, we managed to enhance our velocity repeatability for most cases. However, despite this improvement, in some cases we still noticed significant velocity differences attributed to partial channel clogging, inducing flow rate reduction.

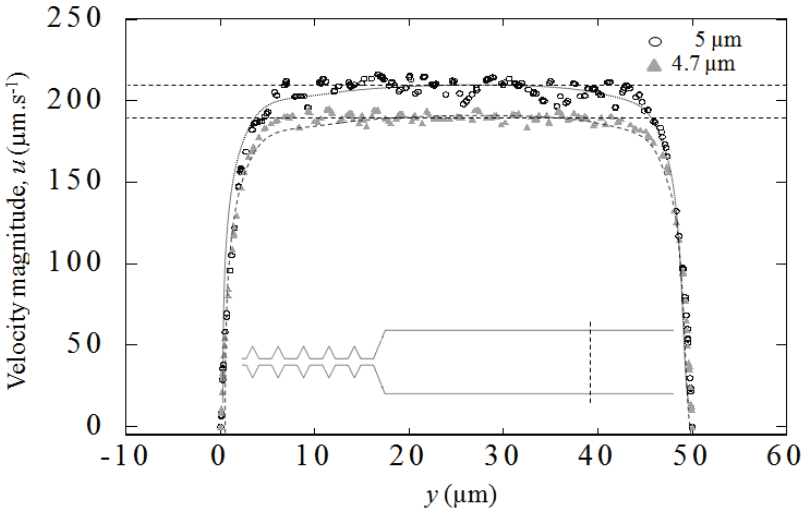

Figure 4.4: Poiseuille profile of the flow speed component u versus y position at 200 µm downstream of the last constriction (see dashed line), for microchannels with 5 µm and 4.7 µm in depth. A pressure driven flow was simulated in both geometries using Comsol Multiphysics® at 200 mbar using external viscosity corresponding to PBS/Dex 9% solution.

4.2.2 ITO electrodes

ED experiments were carried out using Indium Tin Oxide (ITO) electrodes presenting a coplanar and interdigitated geometry (IDE electrodes) (Fig. 4.5). These electrodes were patterned on 150 µm thick cover glass slides. The electrodes were designed to contain 50 electrode fingers that were 5 mm long, 100 µm wide and with an inter-electrode gap of 85 µm (Fig. 4.5-a). The thickness of the ITO layer on the glass slide was 370 nm and was obtained from Solems®. A PDMS layer was bonded to the cover glass *via* O_2 plasma treatment to ensure mechanical stability for the thin cover glass and to define a reservoir around the IDEs (Fig. 4.5-b). Finally, electrode connections were made using an electrically conductive silver-filled epoxy paste (EPO-TEK E 4110).

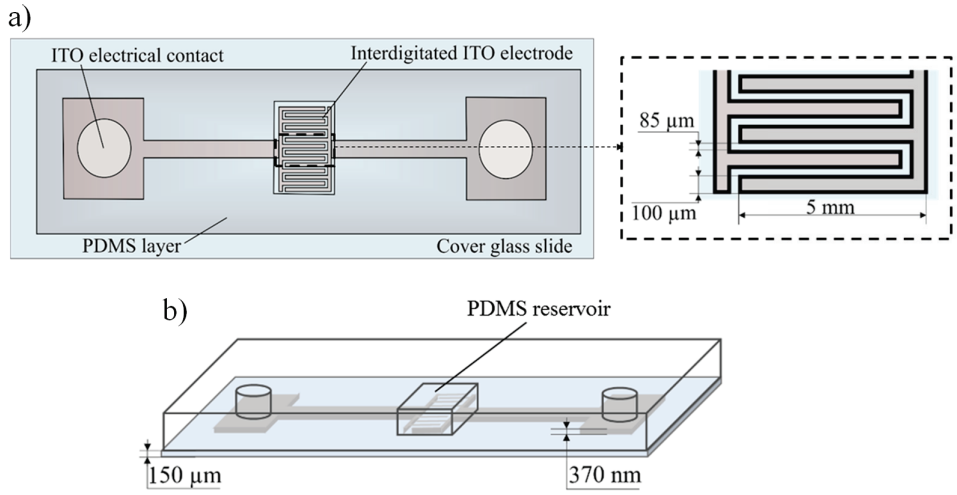

Figure 4.5: Schematics representing (a) a 2-D top view and (b) a 3-D side view of the ED setup. It consisted in a glass slide with ITO interdigitated electrodes bounded with a PDMS reservoir. The design of the interdigited electrodes presents the different dimensions. Drawings are not to scale.

ITO electrodes were prepared by combining photolithography, e-beam evaporation, lift-off and Reactive Ion Etching (RIE) of ITO. Figure 4.6 illustrates the different steps of the protocol (adapted from previous work in litterature [105]) to fabricate ITO interdigitated electrodes on cover slides. The first step was the spin coating of 1.3 µm of Shipley 1813 photoresist (MicroChem®) on the ITO covered glass slide. Then, after irradiation and development, a 200 nm Cr layer was deposited by e-beam evaporation (Evap 300 from Alliance concept®). A lift-off step was then used to reveal the Cr pattern on the glass slide. The role of this Cr layer was to protect locally ITO from unwanted etching during the subsequent RIE step. This etching was carried out in two steps using a RIE machine (Oxford instruments®). In the first step, we used a mixture of CH_4 and H_2 gaz (at 08 sccm and 75 sccm respectively, 100 mTorr pressure and 150 W power) to etch ITO for 40 min. In the second step, we used a mixture of Ar and O_2 gaz (60 sccm and 35 sccm respectively, 300 mTorr of pressure and 300 W power) for 20 min to clean the amorphous carbon issued from the first step. Finally, the remaining Cr layer was removed in a Cr etching solution for few minutes and ITO electrodes were revealed.

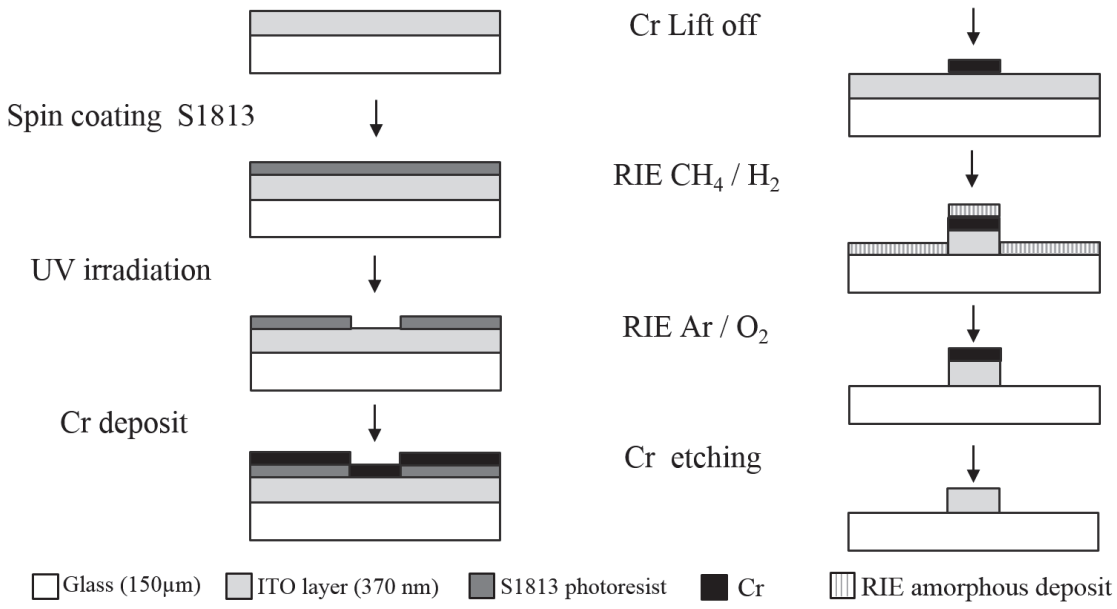

Figure 4.6: Schematic representation of the various steps used to prepare ITO electrode on 150 µm cover glass slides. Schematics are not drawn to scale.

4.3 Experimental setups

All the experiments (passive microfluidics and ED) were performed on an inverted microscope (Leica® DMI 4000B, Germany) with a ×40 magnification for microfluidic experiments and a ×63 magnification for ED assays. The cell behavior was recorded using a high speed camera (Mikrotron® EoSens MC1362, Germany) at 2000 frame.s^{-1} with 400 µs exposure time. Camera Tool and Hiris softwares were used to command the camera.

4.3.1 Passive microfluidic set-up

We used a pressure driven flow to inject the RBCs in the microchannels. Two methods were used to apply the pressure gradient (ΔP from 13 to 500 mbar) between the inlet and outlet of the systems.

First, in the study of the mechanical response of hRBC in passive microfluidics (Chapter 5), we used a pressure regulator (Type 10, Bellofram) connected to a manometer (BD Sensors, Baroli) with a precision of 2 mbar to control the applied pressure (for ΔP >100 mbar). To apply lower pressures (ΔP <100 mbar), we used a hydrostatic pressure difference between the sample reservoir and the outlet.

Second, in the study of the geometry effects (Chapter 7), we used a Fluigent® $MFCS^{TM}$-EZ device with a precision of 0.3 mbar to generate difference of pressure. For experiments requiring to monitor the flow rate in the systems, we used a Fluigent® Flow-Unit S in addition to the pressure actuators.

4.3.2 Electrodeformation set-up

A waveform generator (Agilent® 33521 A) combined to a voltage amplifier (FLC electronics® A880) were used to apply a sinusoidal signal as described in Fig 4.7 at the ITO electrodes, using a home-made Labview® script. RBCs were first attracted towards the electrodes using a signal of amplitude $\Delta V_0 = 2$ V and a frequency of 1 MHz. Then, at the same frequency, the signal amplitude was increased to a value ΔV_1 in order to elongate the cells (stretching). The parameter ΔV_1 was varied from 2 to 48 V. The duration of the applied solicitation, t_{sol} and the resting period, t_{rest}, were varied from 100 to 5000 ms and 500 to 5000 ms, respectively. The number of solicitation cycles (N) ranged from 1 to 400 cycles.

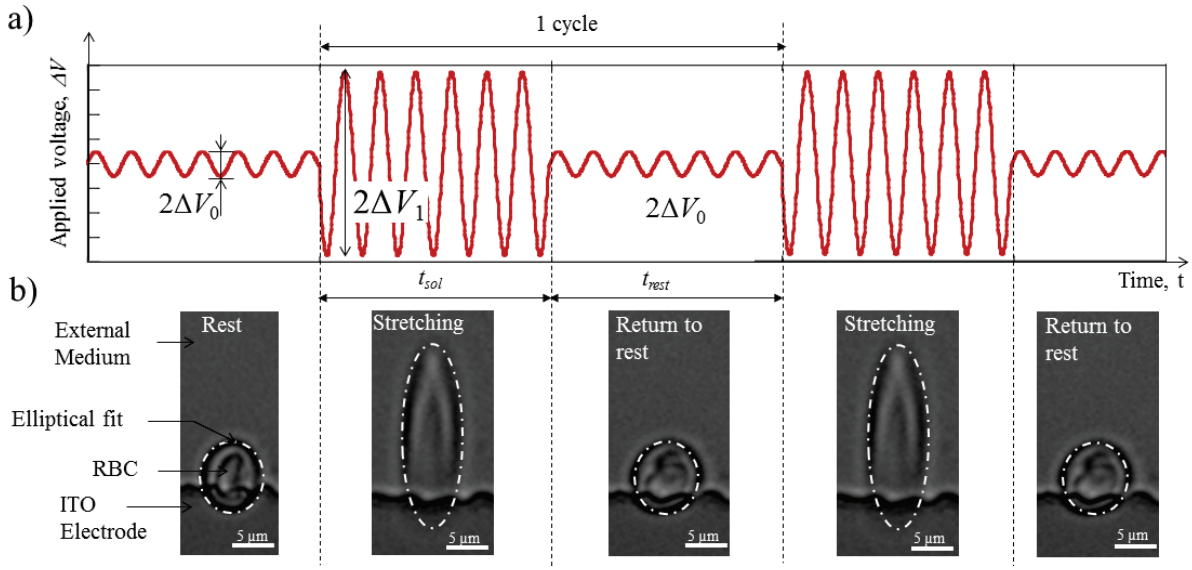

Figure 4.7: (a) Schematic representation of the sinusoidal signal $\Delta V(t)$ applied during the ED experiments. Schemes are not to scale. (b) Microscopic images of a hRBC before stretching ($\Delta V_0 = 2$ V), during stretching ($\Delta V_1 = 32$ V) and after relaxation ($\Delta V_0 = 2$ V).

4.4 Image analysis

The video-microscopic recordings were processed using Matlab® self-made routines. Two different routines were adapted to each application (passive microfluidics and ED) depending on each experiment specifications. The two processes are described below.

4.4.1 Passive microfluidic image processing

For passive microfluidic image analysis, the movies were automatically processed using a self−edited Matlab® code to study cell dynamics and deformation[1].

[1]This code was inspired from the original code developed by M.Abkarian and W.Ristenpart.

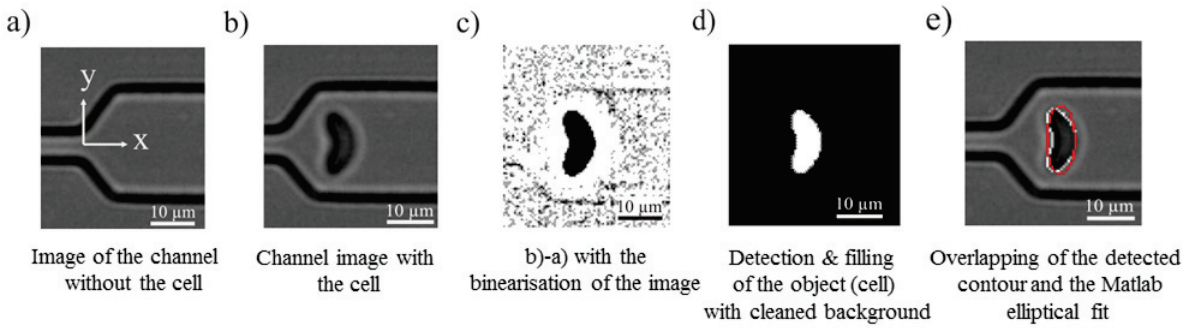

Figure 4.8: Illustration of the Matlab® image processing: (a) the background image without the cell, (b) the image of interest with the cell, (c) the subtracted image (b)-(a), (d) the image (c) after object detection, filling and cleaning of the background, (e) the Matlab® detected contour (white) and elliptical fit (red) superimposed to the original image.

Figure 4.8 illustrates the different steps of the analysis for the cell contour detection. First, we subtract the background image of the channel without the cell (a) from the image of interest (b) to isolate the cell (c). Then, an edge detection is performed and the detected contour is filled while the rest of the image is cleaned (d), *i.e.* elimination of parasite single pixels. (e) represents the object contour (in white) and the elliptical fit (red ellipse) superimposed to the original image. This procedure is repeated for all the images of the recording.
For each image, the position of the ellipse center of mass was retrieved, giving access to the cell position x as a function of time, as represented in Figure 4.9-a. In the inlet area (1) and outlet (3), the cell advances linearly with time along the channel. In the median area (2), the position of the cell seems to depend also linearly with time. However a close-up of the curve shows that cell velocity oscillates, due to the series of constrictions and enlargements. From this curve, we can extract the velocity of the cell passing through the three areas of the OWC microfluidic geometry, V_1, V_2 and V_3 respectively, by calculating the slope of the linear fit in each areas, as illustrated in Figure 4.9-a.

Figure 4.9-b illustrates typical values for cell velocities across a OWC microchannel. Cell velocity in the median zone of the microchannel, V_2, is roughly 9 times higher than V_1 and V_3. The global mean cross section of the tooth-like structure is smaller than the one of the inlet and outlet and can thus explain this difference of cell velocities; the fluid velocity adapts in order to respect flow rate conservation. When the channel section decreases, the flow speed increases and the cell velocity follows. We can also notice that V_3 is slightly higher than V_1 as all cells are centered at the exit compared to the inlet where cells can be on different y positions of the Poiseuille flow and have thus different velocities, as explained later in Chapter 5. This is also coherent with the fact that error bars are smaller for V_3 than V_1.

The lengths of both axes of the elliptical shape were also measured, $2a$ being the axes along the

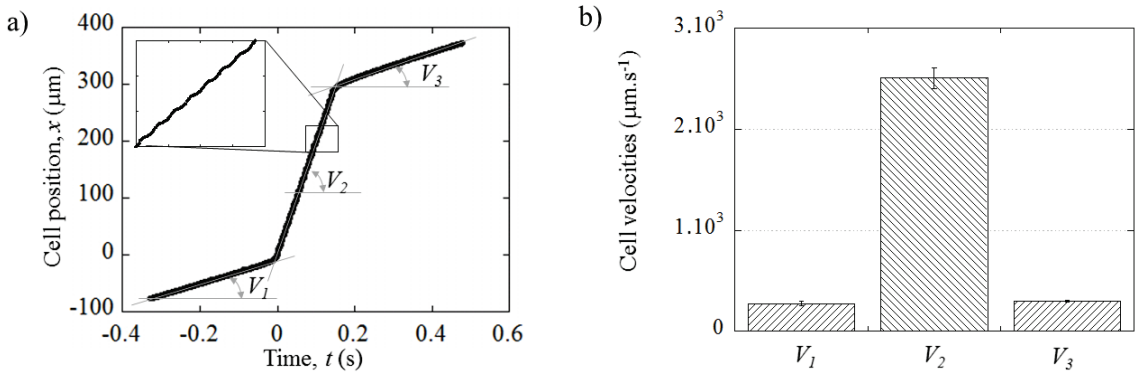

Figure 4.9: (a) Cell position x as a function of time while flowing in the OWC geometry. Velocities V_1, V_2 and V_3 are extracted by calculating the slope of the linear fits. (b) Representation of the three cell velocities in the different parts of the microfluidic channel. ΔP = 200 mbar, η_{out} = 31.5 mPa.s and W_o = 50 µm.

flow direction (x-direction) while $2b$ is the axis perpendicular to the flow (y-direction). Figure 4.10-a illustrates an example of the evolution of $2a$ and $2b$, the axes of the ellipse-assimilated cell, with the flow of a hRBC through the OWC geometry with W_o = 50 µm. The origin of the cell displacement along the x axis has been arbitrarily set to the entry of the first constriction. We can note that, before the entry of the OWC (x < 0 µm), both axes have the same value ~ 8μm, leading to a projected area roughly circular. In the median part of the geometry (0 µm < x < 290 µm), we notice that both axes oscillate in counter phase. Inside the constrictions, $2a$ increases and $2b$ decreases. In contrast, when the cell flows inside the enlargement, $2a$ decreases and $2b$ increases. After the exit of the last constriction (x > 300 µm), the cell is stretched with respect to the y-direction. Hence, the axis $2b$ reaches a maximum whereas $2a$ attains a minimal value, before both axes recover close values when the cell relaxes to reach its equilibrium shape (~ 8 µm for x > 340 µm).

The values of $2a$ and $2b$ were used to calculate the deformation index D defined as:

$$D = (a-b)/(a+b) \tag{4.1}$$

The deformation index D reflects the shape of the cell. Indeed, for D = 0 (*i.e.* a=b) the projected shape of the cell is circular, while for D < 0 (*i.e.*a < b) the cell is elongated according to the y-direction. Conversely, for D > 0 (*i.e.* a > b) the cell is stretched in the x-direction. The deformation index D associated with the axes presented in Fig. 4.10-a is presented in Figure 4.10-b and shows a similar behavior as $2a$. Indeed, D is constant around a value of 0 prior the first constriction inlet. Then in the median part, its value oscillates between its maximal and minimal values D_{max} and D_{min} respectively, allowing the calculation of the amplitude of deformation $\Delta D = D_{max} - D_{min}$. At the last constriction exit, D reaches its minimal value untitled D_{out} corresponding to the cell stretching, before relaxing to its stationary value D_∞ (x >340 µm). An exponential fit of the D = f(t) curve corresponding to the exit, *i.e.* between D_{out} and D_∞, allows the estimation of cell relaxation time τ.

Figure 4.11 represents a typical example of the evolution of the deformation parameters (D_{max},

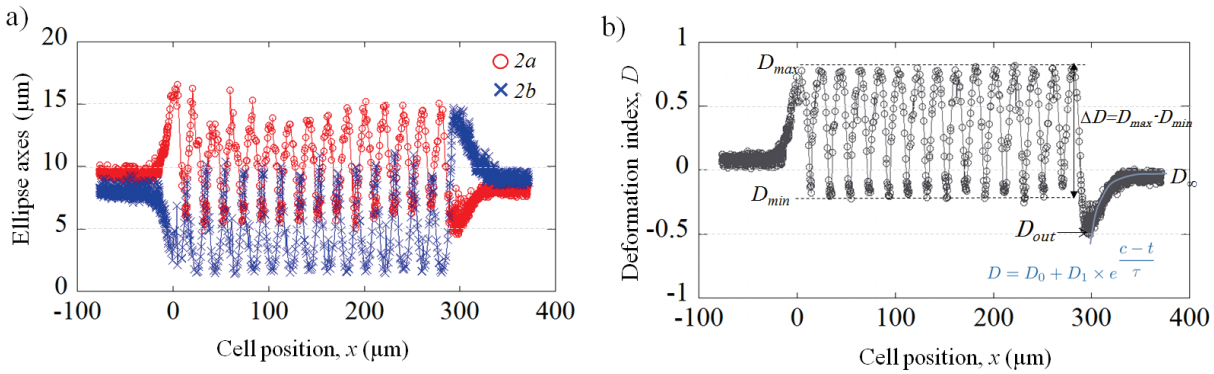

Figure 4.10: (a) Evolution of the axes along and perpendicular to the flowing direction (2a) and (2b) respectively, as a function of x for a healthy RBC flowing in a OWC geometry. (b) Evolution of the corresponding deformation index D=$(a-b)/(a+b)$ versus cell position in the microchannel. All the measured deformation parameters are reported in the figure. η_{out} = 31.5 mPa.s, V_2 = 1980 µm.s^{-1} and W_o = 50 µm. The origins of the two graphs, x=0, have been arbitrarily set to be the entry of the first narrowing.

D_{min} and ΔD) associated with the flow of hRBCs inside the OWC geometry, as a function of the applied pressure P. We can notice from the graph that D_{max}, D_{min} and ΔD do not vary with the applied pressure, hence highlighting that cell deformation inside the OWC geometry is pressure, and thus velocity, independent. Therefore, in the rest of this work, for a specified sample, we will pool the deformation parameters obtained at different pressure and present a unique average value.

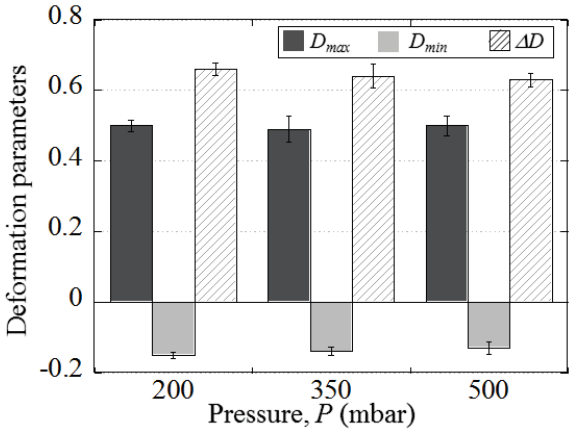

Figure 4.11: Evolution of deformation parameters D_{max}, D_{min} and ΔD versus the applied pressure for hRBCs flowing in the OWC geometry with W_o = 50 µm.

4.4.2 Electrodeformation image processing

Despite the use of transparent electrodes, the videomicroscopic images still showed a border between the ITO and the glass slide, as highlighted in Figure 4.12-a. Accordingly, the automatic image process-

ing of the recordings was not possible due to incorrect edge detection. Therefore, for ED experiments, cell contour detection (Fig. 4.12-b) was made manually using a semi-automated Matlab® routine. The elliptical shape was manually adjusted to best fit the cell contour, while Matlab® automatically stored the elliptical fit information (center of mass, length of both axes) for each image and calculated D according to equation (4.1).

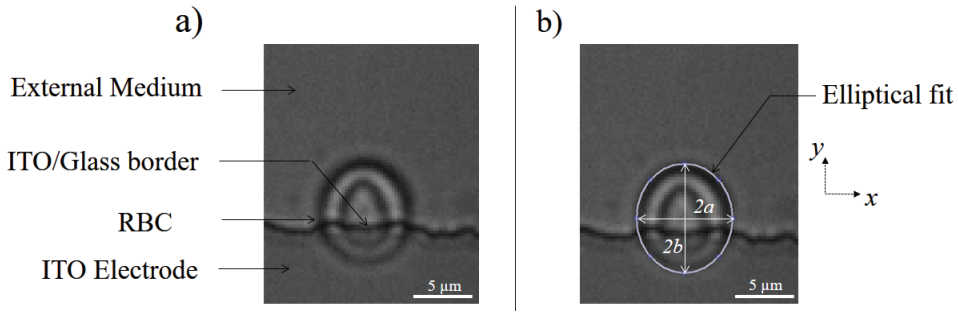

Figure 4.12: Cell contour fitting in ED experiments showing: (a) the cell attracted to the electrodes (the ITO/glass frontier can be clearly distinguished) and (b) the manually adjusted elliptical fit of the cell contour with the two axes.

CHAPTER 5

CHARACTERIZATION OF THE MECHANICAL RESPONSE OF RED BLOOD CELLS IN PASSIVE MICROFLUIDICS

Contents

In the present chapter, we propose to evaluate a passive microfluidic technique to characterize healthy human RBC mechanical response. We first present the design and advantage of the microfluidic geometry used in our study. Then, we investigate thoroughly the shape recovery of healthy RBCs at the exit of the geometry from experimental and theoretical point of view. Finally, we document how experimental parameters may influence the deformation of RBCs both inside and during the relaxation at the exit of the geometry. Several parameters have been examined such as cell speed V_3 after the exit of the last geometrical constriction, the exit channel width W_o and the external buffer viscosity η_{out}.

5.1 The Oscillating Width Channel geometry (OWC)

5.1.1 Channel design and dimensions

We used an oscillating width channel geometry (OWC, already described in Chapter 4) to study the mechanical response of RBCs in passive microfluidics. The geometry and its dimensions are reported

in Figure 5.1. Throughout the study, the main width of the channel inlet/outlet, W_o, has been varied between W_o = 15, 25 and 50 µm while keeping a fixed height of 5 µm. In the median part, a succession of 14 tooth-like shaped geometrical constrictions - composed of a narrowing followed by a widening - has been implemented. In this median part, the channel width decreases from W_o at the entry to W_n = 5 µm and then increases up to W_e = 25 µm. This width oscillation is repeated over a total length L = 290 µm, each restriction and widening has a length of 10 µm.

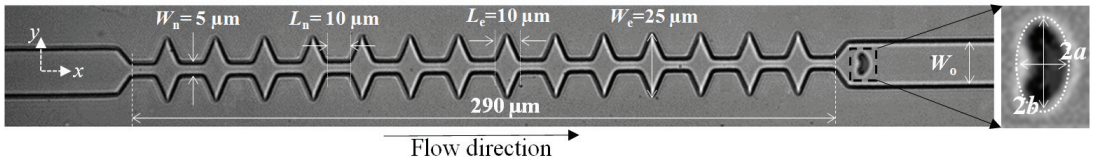

Figure 5.1: Optical image of the microfluidic channel used in the passive microfluidic approach. This microchannel is composed of 14 tooth-like shaped constrictions. The different dimensions of the tooth-like constrictions are reported on the picture, and during the study, W_o has been varied between 15, 25 and 50 µm. The insert shows the close-up of a RBC indicating the two axes along and normal to the flow direction, respectively $2a$ and $2b$.

5.1.2 Choice of the geometry

The OWC geometry principle is similar to that of a microfluidic rheometer. When a RBC flows through the OWC channel, it undergoes a series of stretching along and perpendicular to the flow direction (inside the constrictions and enlargements respectively). The frequency of this periodic solicitation can be adjusted by controlling the flow speed of RBCs through modulating the speed of the external buffer.

Moreover, OWC geometry offers a great advantage for the study of cells deformation and shape recovery at the exit of the last narrowing. Indeed, cells can enter the geometry at various positions, noted y_i, that cannot be controlled. When using a channel implementing a single 10 µm long constriction with 5 µm width, cells entering uncentered tends to rotate when exiting in order to retrieve their initial position y_i, resulting in cells exiting also at various positions, noted y_f. The uncentered exit y_f position and cell rotation complicate the data analysis in two possible ways. In the first place, a cell exiting at a position y_f close to the channel wall does not witness the same speed, and therefore the same hydrodynamic stress, than a cell exiting at a centered position. In the second place, the cell rotation may be considered by the automated Matlab® image analysis routine as a deformation, leading to false measurements.

On the contrary, our OWC geometry has a centering effect on RBCs at the exit. Figure 5.2 shows three examples (one for each tested channel width W_o) of cells entering the channel close to the wall and exiting well centered after undergoing the series of deformation in the median part. One may notice from Figure 5.2, that whatever its position when entering the microchannel, the RBC tends to get centered when exiting the channel hence insuring a symmetrical deformation and relaxation and

thus an easier fit of the data. We also note that this centering effect, is even more pronounced when the channel width W_o is wide (typically 50 µm). Indeed, we can see that the centering amplitude $\Delta y = y_i - y_f$ is larger for W_o = 50 µm (Figure 5.2). This centering effect is especially important for the study of cell shape recovery at the exit of the channel as it implies a symmetrical relaxation of cells, as well as equivalent speed conditions. This centering effect using the OWC geometry was reported in the literature in the case of viscous vesicles flowing in close-fitting channels in the thesis of F. Quemeneur[104], and for RBC flowing in wider constrictions in the thesis of M. Faivre [106]. Authors explained this phenomena by a lift force that pushes deformable object away from the walls; this lift force is undergone by the objects within the constrictions where the shear stress is maximum [104]. In our case, the constriction width being too small, RBCs series of deformation favors the centering of its center of mass with the median flow line and thus centering the RBC at the exit.

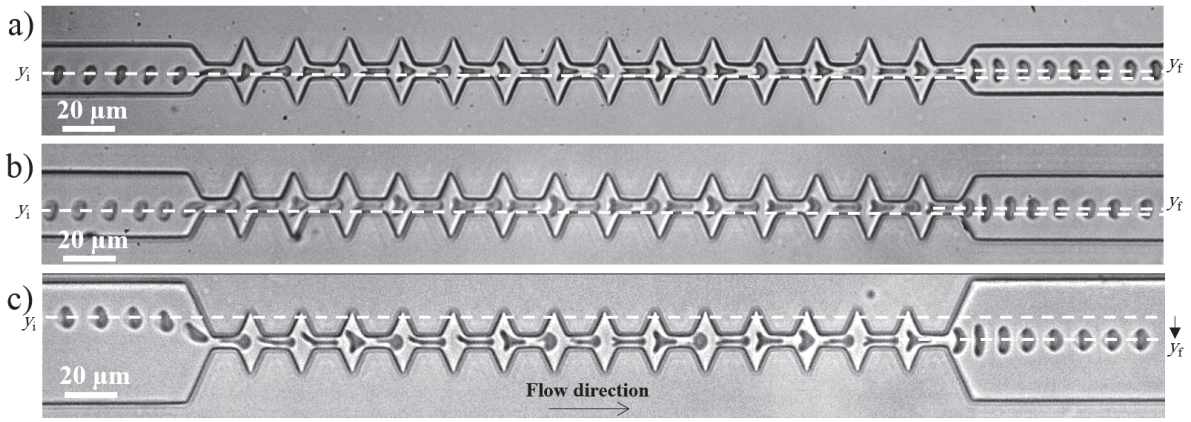

Figure 5.2: Time lapse microscopic images of cell passage in the microfluidic channels illustrating the centering effect of the OWC geometry for: (a) W_o = 15 µm (η_{out} = 31.5 mPa.s and V_3 = 1820 µm.s^{-1}), (b) W_o = 25 µm (η_{out} = 31.5 mPa.s and V_3 = 2194 µm.s^{-1}) and (c) W_o = 50 µm (η_{out} = 31.5 mPa.s and V_3 = 1979 µm.s^{-1}). Dashed lines highlight the shift between the initial position y_i and the final position y_f of the cells.

5.2 Two relaxation behaviors for RBCs flowing out of an OWC

Video-microscopic recordings allowed the visualization of the cell deformation as they flow inside the microfluidic device, as illustrated by the sequences of deformation of healthy RBCs presented in Figure 5.3. Two different behaviors of the cell at the exit of the last constriction have been observed according to the experimental conditions.

5.2.1 Stretching versus unfolding

The cell entering the 15 µm wide channel presents a parachute-like shape, typical of RBC confined flow. As it approaches the first tooth, the cell gets compressed which is traduced by its elongation in the flow direction (Figure 5.3-a and b). Then it undergoes a stretching along the y-axis when

entering the widening. However, before reaching its maximum deformation, the cell is already compressed by the next constriction, leading to a triangular shape inside the enlargements. This cycle of compression-elongation is repeated due to the series of teeth. Finally, as it exits the last narrowing, the cell relaxes to its parachute-like shape in two possible ways, depending on the experimental conditions:

- At high speed and high viscosity of the carrier fluid, the first relaxation mode - **the stretching behavior** - is characterized by a sudden increase of $2b$ (axis normal to the flow direction) as it exits the last constriction, before relaxing back slowly to its equilibrium shape as illustrated in the schematic and the time lapse close-up (Figure 5.3-a).

- At lower speed and lower viscosity, the cell undergoes the same compression-elongation cycles and behaves qualitatively similarly, even if the resulting deformation is less important than in the previous mode (Figure 5.3-b). However at the exit, the cell which is compressed due to the last narrowing, relaxes directly to the parachute-like shape, without being stretched in the y-direction. This mode is referred to as **the unfolding behavior**.

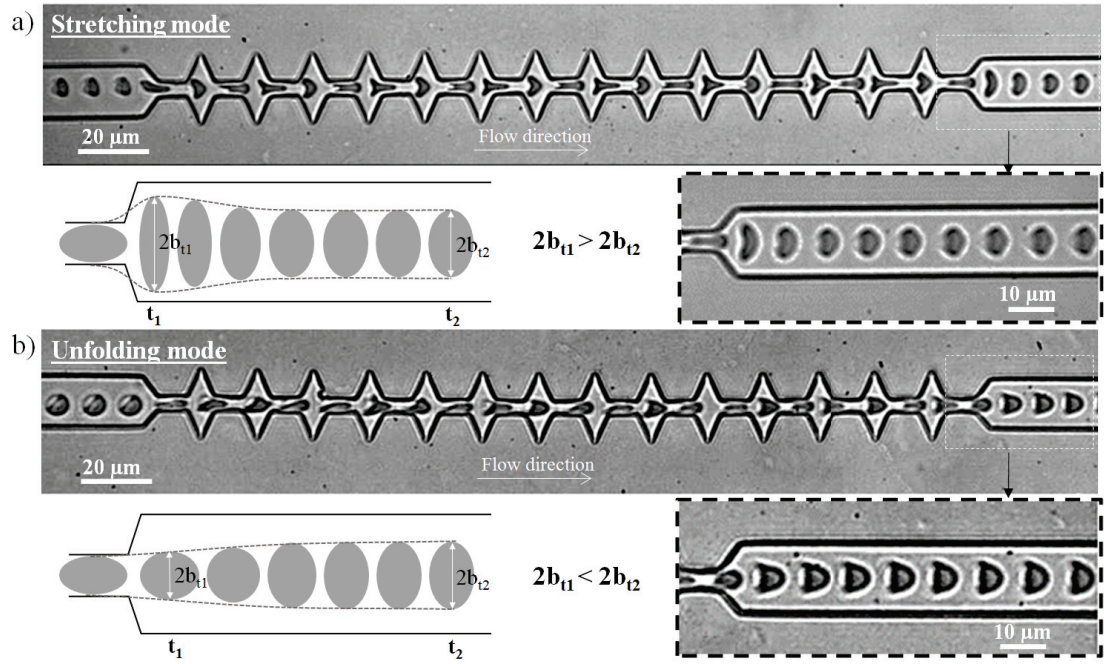

Figure 5.3: Sequences of deformation of two hRBCs under flow (a) at high and (b) at low speed and viscosity of the external medium. Along the geometry, both cells get compressed and elongated perpendicular to the flow direction when entering each narrowing and widening respectively. As they exit in the stretching mode, the cell is stretched by the extensional flow before relaxing to the parachute-like shape, unlike in the unfolding mode where the cell relaxes directly from the compression without being stretched. The external viscosity and the mean speed of the cell at the exit are respectively (a) η_{out} = 31.5 mPa.s and V_3 = 533 µm.s^{-1} and (b) η_{out} = 1.3 mPa.s and V_3 = 483 µm.s^{-1}. The schematics show a representation of the typical deformation in the two behaviors at two different times t_1 and t_2.

The actual deformation of the RBCs flowing in our geometry can be quantified using the deformation index $D = (a-b)/(a+b)$. As an example, the variation of D associated with the sequences of deformation presented in Figure 5.3 are reported Figure 5.4. As the RBC maintains its parachute-like shape, in the 15 µm wide zone of the channel, the corresponding deformation index is relatively constant and nearly close to zero, hence traducing a projected area roughly circular. The following oscillations in D traduce the deformation undergone by the RBC in response to the oscillating width of the channel. Indeed, D increases to positive values ($2a > 2b$) due to the cell compression by the constriction (see upper snapshot) leading to its elongation in the flow direction. In the contrary, when entering an enlargement, it tends to be stretched in the y-direction (see lower snapshot) corresponding to a decrease in D which can reach negative values ($2a < 2b$) depending on the experimental conditions.

In the stretching behavior (Figure 5.4-a), after reaching a maximum value at $x = 285$ µm (corresponding to the cell compression inside the last narrowing), the sudden drop of D traduces the large cell stretching due to its flow out of the last narrowing. Finally, after reaching a minimum at a position $x \sim 295$ µm (corresponding to the maximum stretching once out of the last narrowing), D returns to its initial value and reaches a plateau ; this corresponds to the cell relaxation. In the case of the unfolding behavior presented in Figure 5.4-b, D reaches a maximum at $x = 285$ µm, however, it decreases directly according to an exponential decay to reach the plateau corresponding to the equilibrium shape.

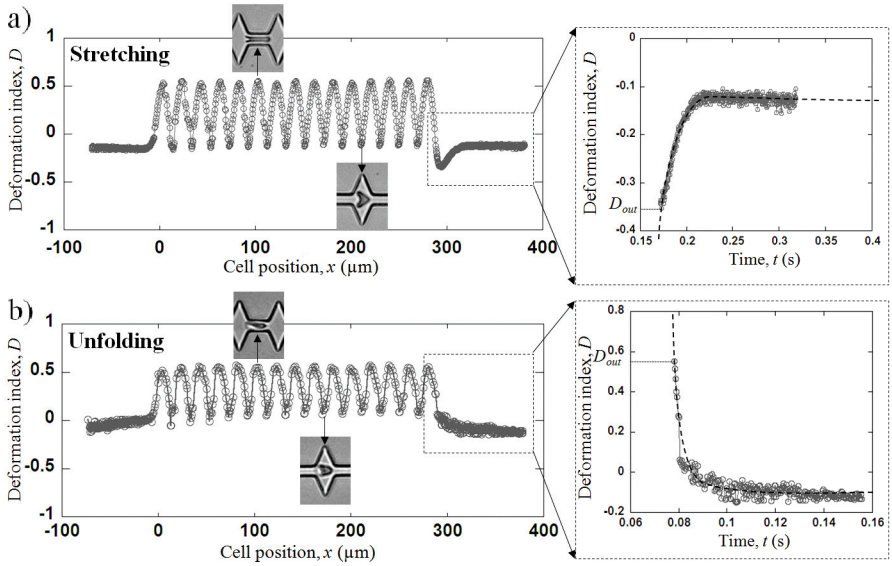

Figure 5.4: Variation of the deformation index $D = (a-b)/(a+b)$ versus the position of the cell's center of mass for (a) the stretching and (b) the unfolding behaviors. The origin of the graphs has been arbitrarily chosen to be the entry of the first narrowing. Close ups represent the variation of D versus time of the two previous curves. Only the time window corresponding to the relaxation is reported. The exit of the last narrowing has been arbitrarily chosen to be $t = 0$. The dashed lines are exponential fits allowing the determination of the relaxation time τ.

In order to extract the relaxation time τ, the variation of D between the maximum deformation at the exit, noted D_{out}, and the equilibrium shape corresponding to the plateau value is represented as a function of time (see close-up Figure 5.4). The experimental data are fitted using an exponential growth or decay depending on the relaxation mode, stretching or unfolding respectively, thus giving τ values.

We evaluated the influence of external flow parameters on the relaxation behavior of healthy RBCs, by varying buffer viscosities and cell velocities. We scanned a range of cell speeds from 100 to 2000 $\mu m.s^{-1}$ and the external viscosity was varied from 1 to 31.5 mPa.s. We gathered experimental results in a relaxation diagram (Fig. 5.5), where the relaxation mode is plotted as a function of η_{out} and V_{cell}. For $V_{cell} \geq 400\ \mu m.s^{-1}$, stretching was observed experimentally for $\eta_{out} \geq 5$ mPa.s, whereas unfolding was obtained for $\eta_{out} \leq 2$ mPa.s. Thus, in this range of cell speed, the transition between the two relaxation modes is mainly dictated by η_{out}. In the frontier zone (highlighted by the dashed line in Figure 5.5), we noticed experimentally a mixed behavior, where a portion of the RBC population experienced stretching, while the other one experienced unfolding. The percentage of the stretching behavior increased with the cell velocity, hence highlighting that the transition depends also on V_{cell}. At lower cell speed, $V_{cell} \leq 350\ \mu m.s^{-1}$, the transition between the two relaxation modes depended strongly on both V_{cell} and η_{out}.

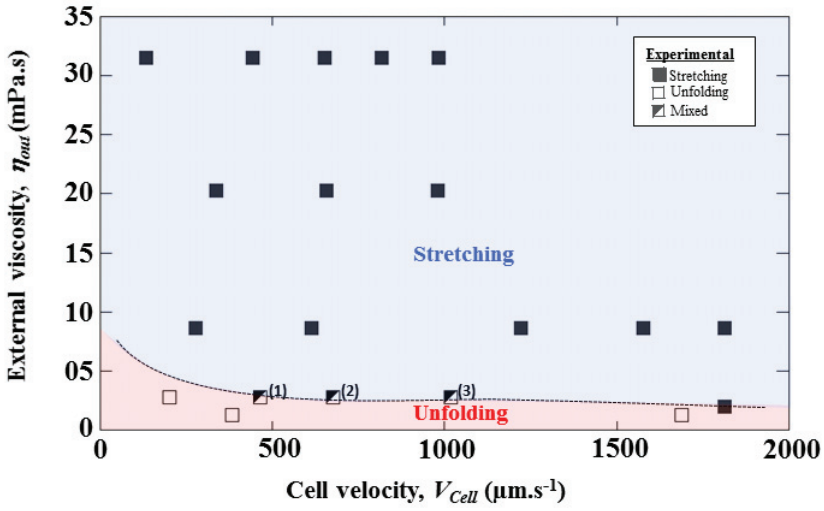

Figure 5.5: Experimental relaxation diagram representing unfolding (open squares) or stretching (solid squares) behaviors according to the cell velocity V_{cell} and the viscosity of the surrounding medium η_{out}. The mixed behavior refers to a mode where a portion of the RBCs experiences unfolding whereas the rest of the population undergoes stretching. The percentages of stretching were (1) 27%, (2) 50% and (3) 55% respectively. The dashed line is a guide for the eyes representing the transition between the two modes.

5.3 Numerical simulations of RBC relaxation flowing out of a geometrical constriction

The mechanical characteristics of RBCs are vital to simulate them in microchannel flow. Over the past decades, many works have been conducted to describe the mechanics of RBCs, these studies have produced several numerical and mathematical models (see [107, 108] for a review of different approaches). These models are built with physical approximations relevant to cell constitutions, geometrical form and membrane characteristics. Some of them use a continuum description [75, 109], while others employ RBCs spring-based membrane models at mesoscopic scale [110, 111] and/or at the molecular level (to model spectrin fibers for example) [111, 112]. The continuum approach is easier and more straightforward to use in simulating RBC mechanics in capillary flow [108]. In this approach, solid models based on membrane linear elastic or hyperelastic mathematical descriptions [75, 113, 114], including viscoelastic effects [89, 114], are used to simulate RBC deformations in microfluidic channels.

To compare with the obtained experimental results, 2-D numerical simulations based on the finite element method have been performed using Comsol Multiphysics®. We described the RBC with a 2-D linear viscoelastic solid model as used previously by [114, 115]. Computation costs and simple implementation of the whole system (*i.e.* RBC and microfluidic physics) in Comsol Multiphysics® environment are the principal reasons for choosing this RBC modeling approach.

For computed resources reasons, a simplified version of our experimental geometry was chosen for the simulations: a 15 µm wide and 170 µm long channel implementing a 5 µm wide geometric constriction which is 10 µm long was used to build the model. The cell was initially placed 30 µm upstream of the narrowing.

The carrier fluid was assumed to be homogeneous, incompressible and Newtonian with a density ρ_{out} of 1000 kg.m^{-3}. Simulations were performed with different external viscosities η_{out} ranging from 1 to 40 mPa.s. At the microchannel inlet, a parabolic profile velocity was applied which maximum velocity V_{max} has been varied between 100 µm.s^{-1} and 1 mm.s^{-1}, while at the outlet, a zero pressure was specified. A no-slip condition was set up along the rigid and fixed walls of the microchannel. The mesh of the external fluid was chosen to be 2-D triangular elements of 2 µm maximum size and was refined at the vicinity of the constriction. The RBC was defined as a linear viscoelastic membrane enclosing a cytoplasm made of an incompressible Newtonian fluid with a dynamic viscosity η_{in} = 6 mPa.s [19] and a density ρ_{in} = 1000 kg.m^{-3}. We imposed a cell with an elliptical shape at rest, with its minor and major axis being $2a$ = 2 µm and $2b$ = 7 µm respectively. The RBC membrane was assumed to be 0.1 µm thick, with a Young's Modulus E_{RBC} = 2.6 kPa [35, 115], a Poisson's ratio ν = 0.49 [35, 115], a density ρ_{memb} = 1125 kg. m^{-3} and a membrane viscosity η_{memb}=5.5 Pa.s [35]. The RBC membrane was meshed with 2-D triangular elements of 0.01 µm.

The interaction of the RBC membrane with both the carrier and internal fluids, belongs to the class of the fluid-structure interaction (FSI) problems. To avoid important distortion of fluid mesh

elements -for example in the constriction - we have used arbitrary langragian-eulerian method (ALE) [116] with automatic remeshing, which is particularly well suited for coupling problems such as FSI with large deformations.

Both the buffer and the cytoplam were described by the Navier-Stokes equation in the case of incompressible and Newtonian fluid with laminar flow as follows:

$$\rho_{out}\left[\frac{\partial \vec{V}_{fluid}}{\partial t} + (\vec{V}_{fluid}.\nabla)\vec{V}_{fluid}\right] = -\nabla P + \eta_{out}\nabla^2\vec{V}_{fluid} + \vec{F}_v \tag{5.1}$$

$$\rho_{out}\nabla.\vec{V}_{fluid} = 0 \tag{5.2}$$

where $\vec{V}_{fluid}$ being the fluid velocity vector, ρ_{out} the fluid density, η_{out} the external medium dynamic viscosity, P the pressure and $\vec{F}_v$ represents the external volumetric force vector (gravity, magnetic field...).

The RBC membrane is considered as a Kelvin-Voigt viscoelastic material [35] which is represented by a spring connected in parallel with a damper. Equation 5.3 describes the dynamical behavior of the RBC membrane :

$$\rho_{RBC}\frac{\partial^2\vec{u}_{RBC}}{\partial t^2} - \nabla.\sigma = \vec{F}_v \tag{5.3}$$

where ρ_{RBC} is the cell density, u_{RBC} is the displacement of the RBC membrane. σ and ϵ represents the stress and strain tensors given by the following equation where η_{mem} is the membrane viscosity:

$$\sigma = \epsilon E_{RBC} + \eta_{mem}\frac{\partial \epsilon}{\partial t} \tag{5.4}$$

To take into account the influence of the flow on the RBC membrane and in return, its perturbation due to the cell presence, equation 5.5 and 5.6 were solved at the fluid-membrane interface:

$$\vec{V}_{fluid} = \vec{V}_{memb}, \text{ with } \vec{V}_{memb} = \frac{\partial \vec{u}_{memb}}{\partial t} \tag{5.5}$$

with $\vec{V}_{memb}$ the membrane velocity at the fluid-membrane interface.

$$\sigma.\vec{n} = \Gamma.\vec{n}, \text{ with } \Gamma = -PI + \eta_{out}(\nabla\vec{V}_{fluid} + (\nabla\vec{V}_{fluid})^T)) \tag{5.6}$$

where Γ is the viscous stress tensor of the fluid at the fluid-membrane interface and I is the identity tensor.

The simulated results were converted into sequences of deformation of the cell as it flows through the constriction and analysed with the same image analysis routine than the experimental data, in order to avoid any bias.

Moreover, in order to be able to compare the simulated results with our experimental data, we had to check if the historic of deformation, *i.e.* number of narrowings in series did not impact the cell relaxation at the exit. Experimental results presented in Appendix A demonstrate that the measurement of τ does not seem to be influenced by the change in the constriction number. Thus, numerical results could be compared to the experimental data, even though the geometry was not identical.

5.3.1 Numerical results

Numerical results of RBC flowing out of a single constriction using the previously described model are presented in Figure 5.6. Depending on η_{out} and V_3, we retrieve numerically the two relaxation modes observed experimentally. Figure 5.6-a and b present the sequence of deformation undergone by a RBC in the stretching and unfolding mode respectively, and the evolution of the deformation index D associated, allowing the calculation of τ. We can note that the very sharp protrusions in the cell shape at the exit of the constriction illustrated in the time-lapse sequence in Figure 5.6-a, have also been observed experimentally in equivalent experimental conditions.

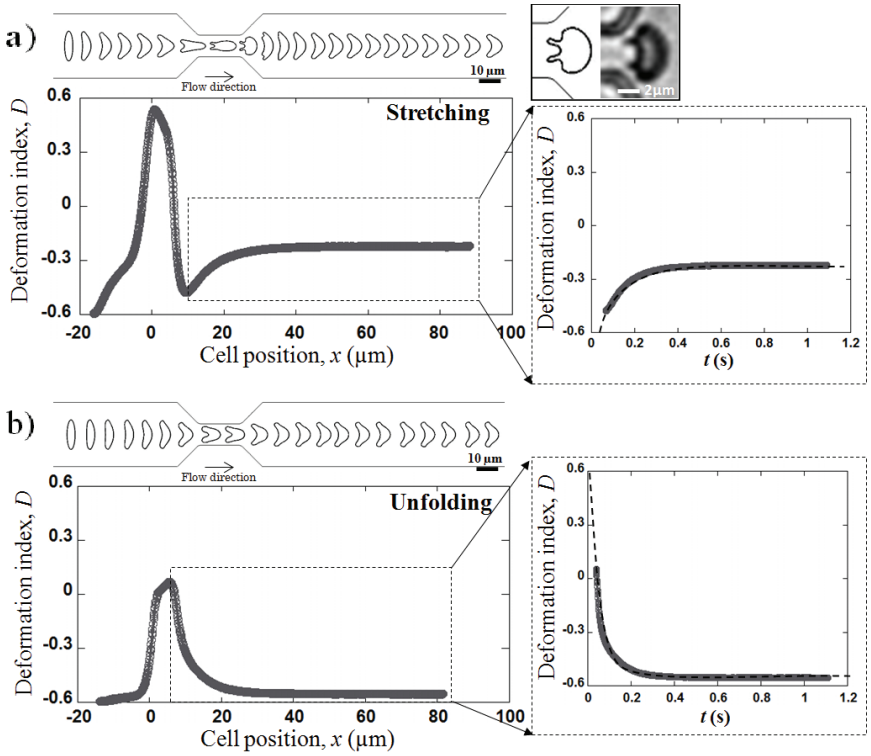

Figure 5.6: Numerical results illustrating (a) the stretching (η_{out} = 20 mPa.s and V_3 = 100 µm.s^{-1}) and (b) the unfolding behaviors (η_{out} = 1 mPa.s and V_3 = 100 µm.s^{-1}). The sequences of deformation and the associated evolutions of the deformation index D are presented.

Similarly to experimental findings, numerical results illustrate that the same types of relaxation modes are observed depending on the viscosity and velocity of the suspending medium(Figure 5.6). We notice that the unfolding behavior is observed at very low viscosities (typically PBS) and low flow rates while we get the stretching behavior at higher viscosities.

The numerical results allowed establishing a numerical relaxation diagram, which is presented in Figure 5.7. Similarly to the experimental observations, at high η_{out} and V_{cell}, the stretching mode is privileged, whereas the unfolding mode is mainly associated to low η_{out} and V_{cell}. For η_{out} = 2 mPa.s and V_{cell} around 1400 µm.s^{-1}, an intermediate behavior is observed, where the evolution of D as a

function of t can be associated either to unfolding or to stretching. We believe that this intermediate behavior is typical of the transition between the two modes. Both experimental and numerical diagrams are in good agreement. Although the 2D model does not depict the whole mechanics of the RBCs. Indeed, in a 2D model, there is no shear modulus in the membrane.

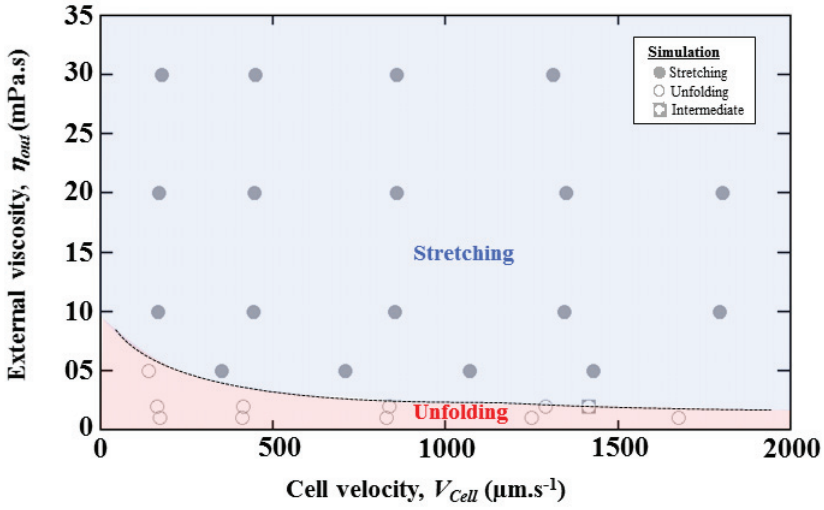

Figure 5.7: Numerical relaxation diagram representing unfolding (open circles) or stretching (solid circles) behaviors according to the cell velocity V_{cell} and the viscosity of the surrounding medium η_{out}. An intermediate behavior which can be associated either to unfolding or to stretching is observed. The dashed line is a guide for the eyes representing the transition between the two modes. The young modulus was set at E=2.6 kPa.

5.4 Theoretical analysis of RBC flowing out of a fluidic micro-constriction

In passive microfluidics, the change in shape undergone by cells is defined by both the geometry and the associated flow. In this section, we present a theoretical analysis of the flow of a RBC at the exit of a geometrical constriction. This interpretation aims at elucidating the transition between the two relaxation behaviors described in the upper section, from a fluidic perspective. First, we define the velocity gradients $\nabla\vec{V}$ at the origin of this flow induced deformation. Then, we apply this analysis to the case of a RBC at the exit of a geometrical constriction. We used Comsol Multiphysics® software to calculate the local velocity gradients at this location, which we used to evaluate the stress probed by RBCs. Finally, a threshold stress is retrieved from the transition between the two modes and used to evaluate the Capillary numbers corresponding to each mechanical property of the RBC in order to determine the dominant one.

5.4.1 Velocity gradients and their contributions

In flow induced deformations, both the deformation and rotation of objects in a flow are directly linked to velocity gradients. These velocity gradients are summarized in $\nabla\vec{V}$ as explained below. We focused our study on a 2-D domain $[x, y]$ as the velocity gradient in z direction is only limited by the Poiseuille flow (the depth of the channel z being constant). In a 2-D Cartesian coordinate system, we define the fluid velocity vector $\vec{V}$ with components u and v as the fluid velocity in x and y directions respectively:

$$\vec{V} = u\vec{i} + v\vec{j} \tag{5.7}$$

where $\vec{i}$ and $\vec{j}$ are the unitary vector in x and y directions respectively.

Its gradient $\nabla\vec{V}$ is given by a matrix:

$$\nabla\vec{V} = \begin{pmatrix} \partial(u,x) & \partial(u,y) \\ \partial(v,x) & \partial(v,y) \end{pmatrix} \tag{5.8}$$

This matrix can be separated into two parts. A symmetrical part, S, which represents the strain tensor:

$$\mathbf{S} = \begin{pmatrix} \partial(u,x) & \frac{1}{2}[\partial(u,y) + \partial(v,x)] \\ \frac{1}{2}[\partial(u,y) + \partial(v,x)] & \partial(v,y) \end{pmatrix} \tag{5.9}$$

and an anti-symmetrical part, Ω, which represents the rotation tensor:

$$\Omega = \begin{pmatrix} 0 & \frac{1}{2}[\partial(u,y) - \partial(v,x)] \\ \frac{1}{2}[\partial(v,x) - \partial(u,y)] & 0 \end{pmatrix} \tag{5.10}$$

Figure 5.8-a represents schematically the local velocity gradients in and at the exit of the microfluidic constriction, as well as their contributions to cell deformation and rotation. We can notice that prior to the exit, we have a Poiseuille flow in the x direction where the velocity is unidirectional, *i.e.* $\vec{V} = u\vec{i}$. The same velocity profile can be observed in the area away from the exit, in the large section of the microchannel. However, the velocity amplitude is smaller due to the flow rate conservation. At the constriction exit, where the channel width abruptly increases, the orthogonal velocity v is no longer zero and we observe a perpendicular flow in the y direction.

Figure 5.8-b illustrates the contributions of each velocity gradient to the cell deformation/rotation. First, we have $\partial(u,x)$ which represents the decrease of amplitude u in the x direction due to the section enlargement. $\partial(u,x)$ induces the compression of the cell as shown in figure 5.8-b. Then, the widening of the channel section induces the appearance of the gradient $\partial(v,y)$. This latter produces the elongation of the cell in the y direction. The combination of both $\partial(u,x)$ and $\partial(v,y)$ is responsible of the cell elongation at the exit of the geometrical constriction.

Previous studies in literature have estimated the fluid dynamic action in a long small angled-divergent channel to be $St \sim 3\eta_{out}\partial(u,x)$ [86]. In our case, the elongational applied stress can similarly be estimated as :

$$St \sim 3\eta_{out}\left[|\partial(u,x)| + |\partial(v,y)|\right] \tag{5.11}$$

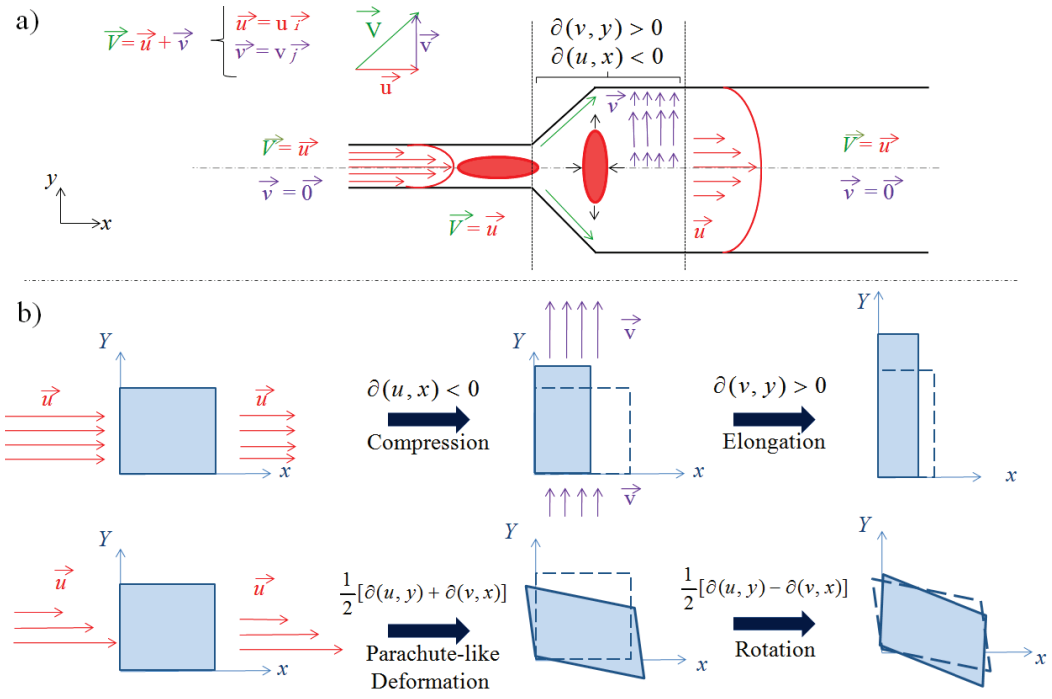

Figure 5.8: (a)Schematic representation of the flow induced deformation of RBCs at the exit of the fluidic constriction. (b) The contribution of velocity gradients to cell deformation and rotation, broken lines represent the state of the object prior to deformation/rotation.

On the other hand, due to the Poiseuille flow, a gradient $\partial(u,y)$ is also present in the channel and is associated with $\partial(v,x)$. Both terms are responsible for the typical parachute-like shape of RBCs in a microchannel. Finally, the rotation tensor is null as the velocity profile is symmetrical with respect to the y axis for in both u and v components.

5.4.2 Theoretical calculation of the applied stress

In order to have an estimation of this local stress St probed by the cell at the channel exit, we used Comsol Multiphysics® to perform simulations of the flow of Dextran solutions in the OWC geometry. We evaluated this stress for various experimental conditions: η_{out} = 2.8, 8.6 and 31.5 mPa.s and for three applied pressures at the channel inlet ΔP = 20, 100 and 200 mbar. For each condition, we evaluated the two velocity gradients at the position x = 297 µm (at the exit of the constriction) and we calculated the local elongational stress according to equation (5.11). An example of the velocity profiles is presented in Figure 5.9. First, we have the geometry layout (5.9-a) illustrating the locations where the velocity gradients $\partial(u,x)$ and $\partial(v,y)$ were calculated (cut lines green and red respectively). Next, we show the typical velocity profiles: $u(x)$ and $v(y)$ in Fig 5.9-b, d respectively and their derivatives $\partial(u,x)$ and $\partial(v,y)$ in Fig 5.9-c, e. We notice that for $u(x)$ plotted in the x direction (red line), in the oscillating width part, the amplitude swings between a maximum and a minimum value corresponding to the narrowing and the widening respectively before it reaches a plateau after

the exit of the constrictions. This amplitude oscillation is reflected on the $\partial(u,x)$ which also fluctuates between a positive and a negative zone corresponding to the increase/decrease in the u amplitude. As for the $v(y)$ plotted over the y direction (green line), we notice a double Poiseuille profile around $y = 0$ as v increases in both directions(y>0 and y<0) starting from $y = 0$ to reach a maximum before decreasing back to zero near the channel wall. The corresponding gradient $\partial(v,y)$ can be divided into 2 parts around $y = 0$, a positive part where v increases and a negative part where v decreases.

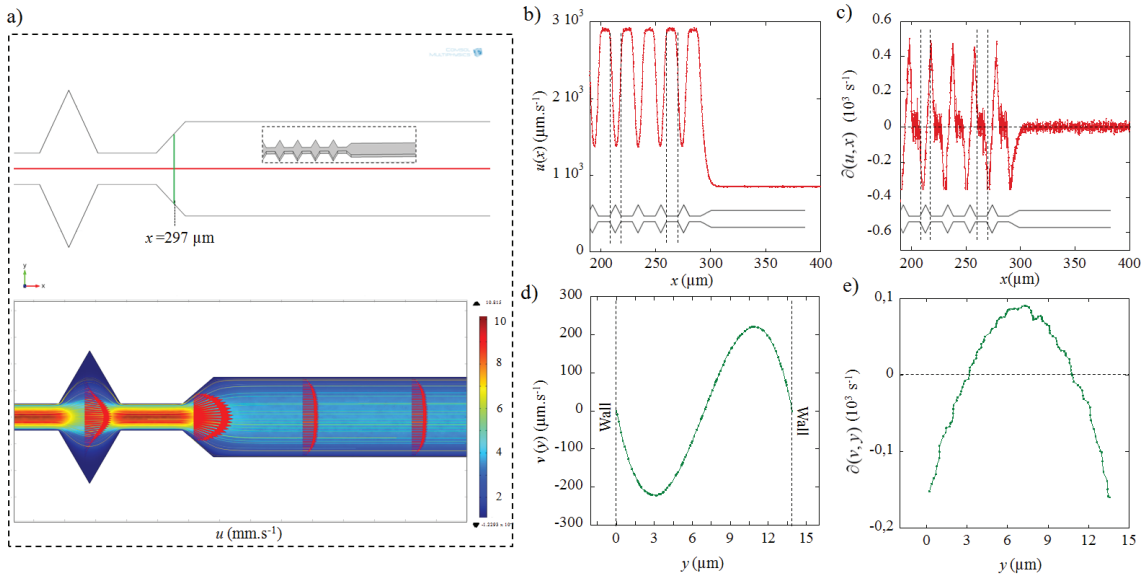

Figure 5.9: Comsol Multiphysics® 3-D simulations of the hydrodynamic flow at the exit of the final constriction in the OWC geometry (η_{out} = 2.8 mPa.s and V_{max} = 900 µm.s^{-1}): (a) the geometry layout and the representation of the velocity profile in the geometry in colormap, (b) the x-component of the velocity u = f(x), (c) the derivative of u with respect to x direction ($\partial(u,x)$), (d) the y-component of the velocity v = f(y), (e) the derivative of v with respect to the y-direction ($\partial(v,y)$).

Estimation of the elongational local stress: Figure 5.10 illustrates the evolution of St as a function of the fluid velocity at the exit. V_{max} corresponds to the maxima of the parabolic velocity profile. We notice that St increases linearly with the flow rate as the velocity gradients increase with the flow rate, as well as with η_{out}.

Using these simulations, we estimated the value of St for the experimental conditions corresponding to the frontier between the unfolding and the stretching behaviors. For η_{out} = 2.8 mPa.s and V_{max} ranging from 460 to 1018 µm.s^{-1} (extracted from the relaxation diagram presented in Figure 5.5), we found 0.6 < $(St)_{transition}$ < 1.38 Pa. To elucidate which elastic property dictates the experimental relaxation behavior of healthy RBCs, we aim at calculating the three Capillary numbers $Ca_{bending} = \frac{St.2b}{B}$, $Ca_{shear} = \frac{St.2b}{\mu}$ and $Ca_{stretching} = \frac{St.2b}{K}$, associated with the bending modulus B, the shear modulus μ and the stretching modulus K respectively, $2b$ being the typical size of cells. Therefore, we use the already estimated viscous stress St undergone by RBCs at the exit.RBC elastic moduli have been previously reported in literature to be $B = 1.8 \times 10^{-12}$ µN.m^{-1} [34], μ = 2.5–9 µN.m^{-1} [29, 30]

and K = 200 mN.m^{-1} [35]. These values allow the calculation of the associated Capillary numbers to be of the order of $Ca_{bending} \sim 10^9$, $Ca_{shear} \sim 1$ and $Ca_{stretching} \sim 10^{-6}$ respectively. Therefore, we can conclude that the shear modulus drives the transition between the relaxation behaviors of RBCs. The study of RBC relaxation behavior at the exit of a microfluidic constriction could be a novel way to evaluate RBC elastic shear modulus.

We can also conclude from these results that the unfolding behavior may occur starting from $V_{max} \sim 140$ µm.s^{-1} for η_{out} = 8.6 mPa.s and at $V_{max} \sim 0$ µm.s^{-1} for η_{out} = 31.5 mPa.s. These values were not reached experimentally ($(V_{max})_{min} \sim 277$ and 133 µm.s^{-1} for η_{out} = 8.6, 31.5 respectively) due to technical limitations, which could explain why we only observed stretching behaviors for both viscosity values.

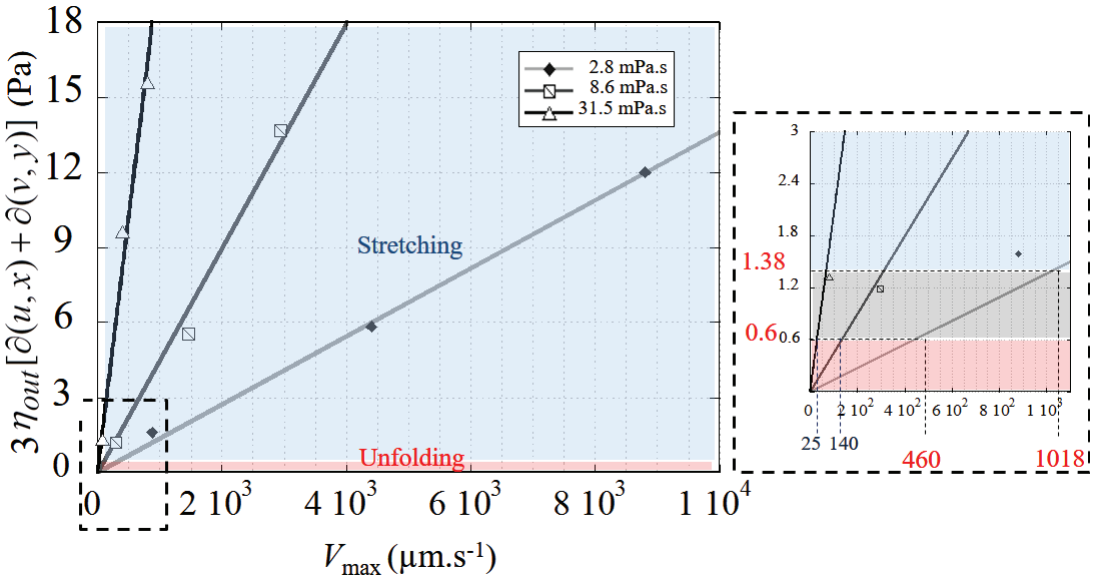

Figure 5.10: Representation of the applied stress at the exit of the geometrical constriction versus the flow velocity at the exit V_{max} and the external medium viscosity η_{out} showing the two behaviors regions (unfolding/stretching) as well as the threshold stress ($St_{transition}$(threshold)). Numerical simulations were performed using W_o =15 µm. The insert shows a close-up on the origin of the plot. Gray zone represents the transition zone.

In order to consolidate our theoretical analysis, we studied numerically the impact of the RBC mechanical resistance on the unfolding/stretching transition zone. To do so, we performed numerical simulations of RBC flowing out of a single micro-constriction using the same model detailed in section 5.3 with different values of RBC Young modulus (E_{RBC}) ranging from 1 to 26 kPa. Figure 5.11 represents the relaxation diagrams for 2 tested values of E_{RBC} (1 and 26 kPa). The results highlight the dependency of the threshold zone upon this parameter E_{RBC}. Although the frontier between the two modes is curved for small cell velocities, a plateau value of η_{out} is observed at higher cell speed. We notice that when E_{RBC} increases, this η_{out} plateau value at which the transition occurs also increases. The frontier being curved, we were not able to determine a specific value of η_{out} for each

E_{RBC}. However, for an arbitrary value of V_3 = 500 µm.s^{-1}, the transition occurs around η_{out} = 2 and 17 mPa.s for E_{RBC}= 1 and 26 kPa respectively, as shown in Figure 5.11 (in red). Numerical simulations were conducted for several E_{RBC} at V_3 = 500 µm.s^{-1}. The obtained values show a linear correlation between the RBC Young modulus and the external viscosity η_{out} at which the transition between the two relaxation behaviors occurs as illustrated in Figure 5.11-c. This observation corroborates correctly with the previously proposed analysis, when E_{RBC} and thus μ increases, the cell becomes more resistant to deformation and necessitates higher stress values (a higher η_{out} for a given velocity) to switch from an unfolding to a stretching behavior. Although the numerical model doesn't include the shear elasticity of the RBC, we still retrieve the transition between the two modes. This transition is directly influenced when we artificially increase cell's rigidity trough the Young modulus.

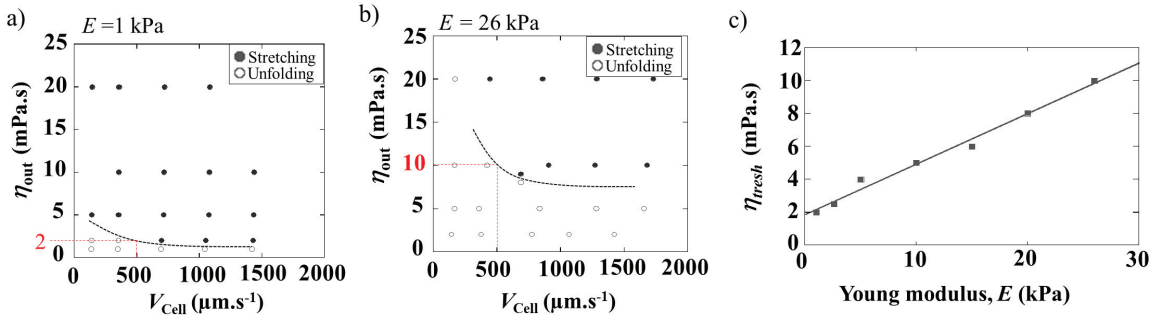

Figure 5.11: Dependency of the transition zone (unfolding/Stretching) upon the variation of the Young modulus of RBC simulated for (a) E_{RBC} = 1 kPa, (b) E_{RBC} = 26 kPa. The guidelines represent a guide for the eyes highlighting the frontier between stretching and unfolding. (c) Evolution of the transition zone between the unfolding and stretching behavior versus the RBC young modulus used in Comsol Multiphysics® simulations.

In figure 5.12 we show experimental relaxation diagrams for two channel widths, W_o= 15 and 50 µm. We may notice from the results that the transition zone between the two relaxation behaviors is slightly higher for the 15 µm geometry than the 50 µm (3 mPa.s and 1 mPa.s respectively). This can be explained by the hydrodynamic stress corresponding to both geometries, the 50 µm wide channel being larger, it produces higher velocity gradients (both $\partial(u,x)$ and $\partial(v,y)$) and thus higher hydrodynamic stress for an equivalent viscosity which explains the lower transition zone. Indeed, at W_o = 50 µm the hydrodynamic stress produced at η_{out} = 2 mPa.s is sufficient to elongate the cells at the exit resulting in a stretching behavior.

This technique could be used to determine the elastic shear modulus of cells which remain to be demonstrated experimentally. Using a combination between the experimental determination of the transition zone between the two relaxation behaviors and the corresponding hydrodynamic forces issued from simulations, we can evaluate cell's elastic properties and eventually distinguish mechanically impaired samples.

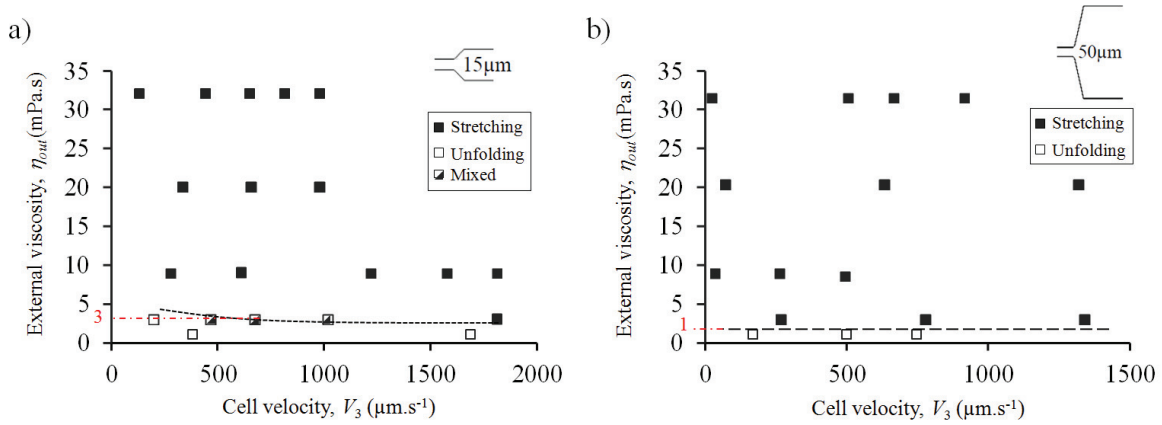

Figure 5.12: Evolution of the transition zone versus channel width for: (a) W_o=15 µm, (b) W_o=50 µm.

5.5 Influence of the experimental parameters on the mechanical response of RBCs

In this section, we performed several experiments in order to understand the impact of each experimental parameter individually on the relaxation time τ as well as on the deformation index D_{out} at the exit of the OWC geometry for both the stretching and unfolding modes.

5.5.1 Effect of the cell velocity V_3

To assess the influence of cell velocity on its mechanical response, we varied the cell speed in the range V_3 = 100-1600 µm.s^{-1} by tuning the applied pressure. The experimental results are presented in Figure 5.13. We notice that - for a fixed external medium viscosity η_{out} and a channel width W_o - the cell deformation at the exit D_{out} is not influenced by the cell speed in the tested range. Figure 5.13-a shows that D_{out} remains constant when we varied the flow rate. We explain this result by the fact that although the applied stress St increases with the flow rate, RBC transits through the high stress region more rapidly when V_3 increases. Consequently, the increase of St is counterbalanced by the short time RBC spends in this region.

In contrast, we noticed a dependency of τ upon the cell velocity. Figure 5.13-b illustrates the linear relationship of $1/\tau$ versus cell speed. We can see from the results that $1/\tau$ increases (τdecreases) with the cell speed. Previous studies in the literature have observed such behavior and explained it through energy dissipation [49]. The relative velocity between the cell and the surrounding medium increases when rising the flow velocity. We think that this increase in relative velocity impacts energy dissipation and thus the relaxation time. Cells take less time to relax to their stationary shape after the deformation D_{out}.

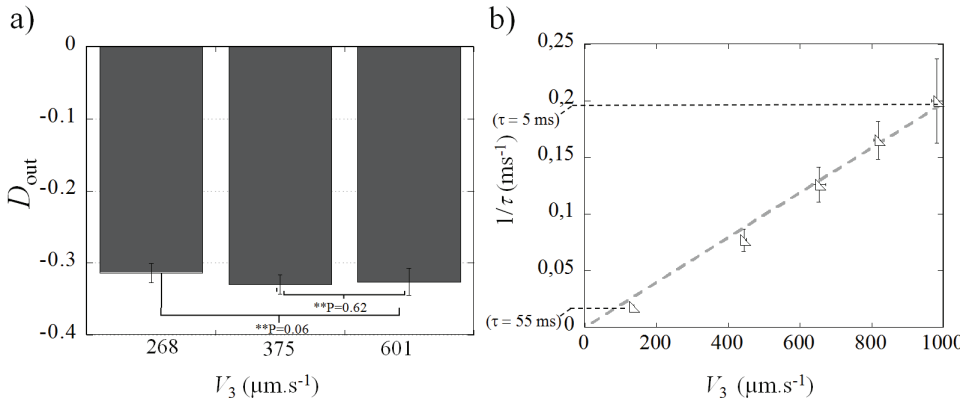

Figure 5.13: (a)Dependency of cell's maximal deformation at the exit D_{out} upon the cell speed V_3. (b) The inverted relaxation time $1/\tau$ versus cell speed V_3. Error bars represent the standard deviation.

5.5.2 Effect of the main channel width W_o

Experiments have been performed at various η_{out} and cell speed V_3 after the last constriction of the OWC, using three different main widths of the channel : W_o = 15, 25 and 50 µm. All the other parameters (dimensions and number of constrictions) being maintained constant. When modifying W_o, we retrieve qualitatively the two relaxation behaviors: stretching for high velocity and high viscosity and unfolding for low viscosity and low cell speed. RBCs maximum deformation D_{out} and the associated relaxation time τ have been extracted.

We first present in Figures 5.14-a and b, the results obtained for cells experiencing an **unfolding relaxation**. As illustrated in Figure 5.14-a, the maximum deformation D_{out} experienced by cells flowing through the last geometric restriction, is independent of both the V_3 and W_o. Indeed, in the unfolding behavior, D_{out} corresponds to the cell compression in the last narrowing, hence only depending on the constriction dimensions which is identical in each of the three geometries. Figure 5.14-b presents the evolution of $1/\tau$ as a function of V_3, η_{out} being fixed at 1.3 mPa.s, for the two values of W_o. The results show that $1/\tau$ is increasing linearly - thus τ is decreasing - with increasing V_3. Such behavior has already been reported by Prado et al. [89] where authors evaluated the time necessary for RBC, initially at rest in a capillary, to adopt a steady shape when the flow is suddenly started. Data issued from different geometries (different W_o) collapse on the same linear regression, hence demonstrating that the relaxation time in the unfolding mode is not impacted by the width of the channel (Fig. 5.14-b).

Then, Figures 5.14-c and d highlight results obtained for cells undergoing the **stretching relaxation** mode. Figure 5.14-c reveals that, for a fixed external viscosity (η_{out} = 31.5 mPa.s), cells are more stretched at the exit of a 50 µm wide channel than when W_o = 15 µm. Regarding the relaxation time, we retrieve in the stretching behavior, the linear relationship between $1/\tau$ and V_3 (Figure 5.14-d). The graph also reveals that for a given cell velocity, $1/\tau$ increases - *i.e.* τ decreases - when W_o is decreased, which is consistent with the fact that cells take longer times to relax from a more deformed state.

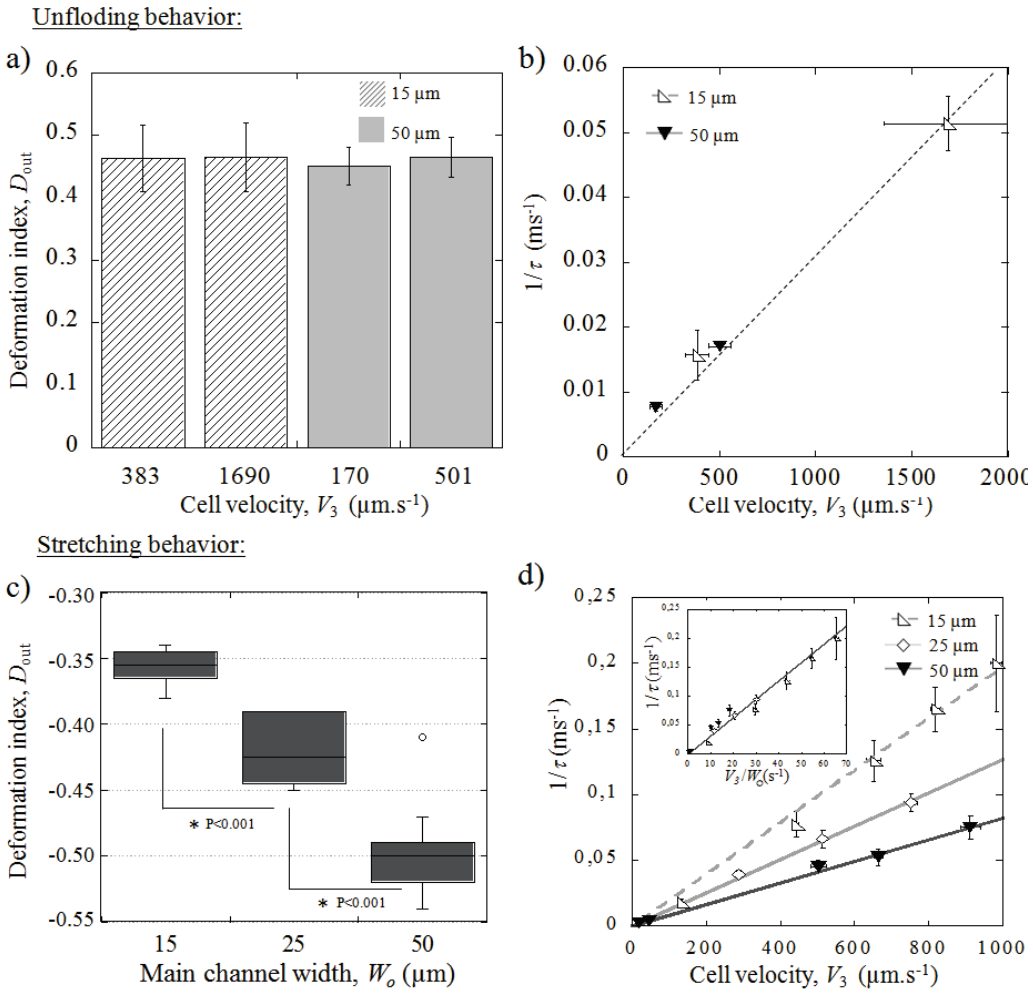

Figure 5.14: Evolution of (a) the cell deformation D_{out} at the exit of the last constriction and (b) $1/\tau$ with the cell speed V_3, for healthy RBCs experiencing the unfolding behavior in channels of different main widths W_o. The external viscosity η_{out} was set at 1.3 mPa.s. (c) Evolution of D_{out} versus the main channel width W_o, for the stretching behavior (η_{out} = 31.5 mPa.s). (d) $1/\tau$ as a function of V_3, for healthy RBCs undergoing stretching at the exit of channels with different widths W (η_{out} = 31.5 mPa.s). The close up highlights that with the representation $1/\tau$=f(V_3/W_o) all data points collapse. For both relaxation mode, each point represents a statistic of at least 20 RBCs.

Moreover, by plotting $1/\tau$ versus V_3/W_o, we can collapse all the data on a single line as illustrated by the inset of Figure 5.14-d.

We observed in Figure 5.14-c that D_{out} values were directly linked to the channel width. Indeed, RBCs maximal deformation at the exit D_{out} increased with the increase of W_o. This can be explained by the increase of the hydrodynamic stress applied to the cells at the exit. Indeed, when W_o raises, both velocity gradients ($\partial(u,x)$ and $\partial(v,y)$) increase leading to a higher applied stress St and thus a larger deformation of the cells. For the relaxation time, we also noticed a variation of τ values when we increase W_o. Figure 5.14-d illustrates that, when W_o increases $1/\tau$ decreases (τ increases).

Indeed, when we raise W_o, D_{out} increases and thus RBCs take longer times to relax. This result was also obtained using an non-hydrodynamic solicitation, electrodeformation for which the results are presented in Chapter 6.

5.5.3 Effect of the external medium viscosity η_{out}

Finally, we report the effect of the external medium viscosity, η_{out}, on the relaxation time of healthy Red Blood Cells. To do so, we performed experiments varying the viscosity of the external medium from 1.3 mPa.s to 31.5 mPa.s and the cell speed from 100 to 1600 µm.s^{-1}. Figure 5.15 presents the variation of D_{out} versus η_{out} and $1/\tau$ as a function of V_3/W_o, for various conditions of external viscosity η_{out}.

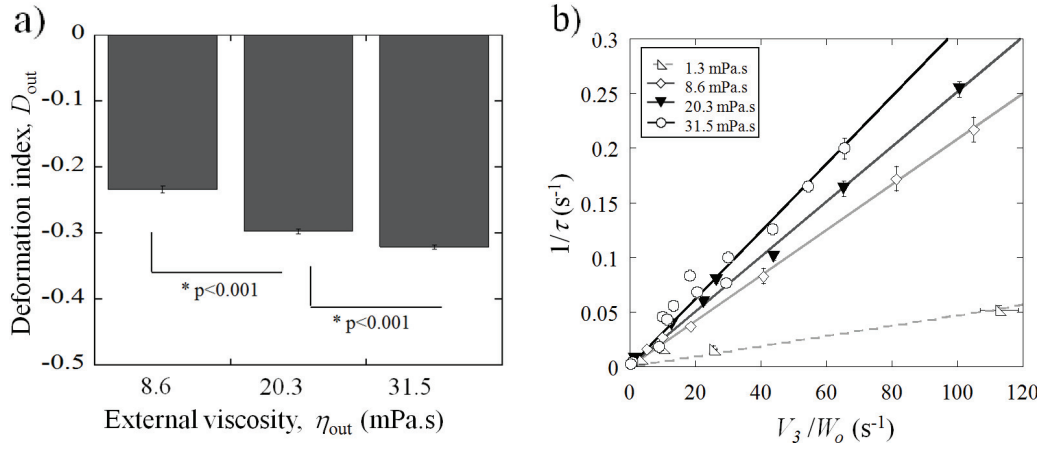

Figure 5.15: Evolution of (a) D_{out} versus the viscosity of the external buffer η_{out} (b) Variation of $1/\tau$ as a function of V_3/W_o, for various conditions of η_{out}. Each point represents a statistic of at least 20 RBCs.

First, we notice from Figure 5.15-a that cell elongation at the exit D_{out} increases with the external medium viscosity. Indeed, when we increase η_{out}, the local stress at the exit St increases leading to a larger elongation of the cells at the exit. Figure 5.15-b represents the results of $1/\tau$ versus V_3/W_o for η_{out} = 1.3, 8.6, 20.3 and 31.5 mPa.s. One may have noticed that we did not include the data obtained at η_{out} = 2.8 mPa.s. Indeed, we were not able to collapse the data obtained at this viscosity for different W_o, because cells were presenting the two different behaviors. Indeed, RBCs experienced a stretching behavior for W_o = 50 µm, whereas, for W_o = 15 µm, they experienced an unfolding behavior. As explained earlier, the relaxation times associated with both modes are very different. Collapsing the data upon representation of $1/\tau$ versus V_3/W_o was only possible if the cells undergo the same relaxation behavior according to the different conditions. Therefore we did not include the data obtained at η_{out} = 2.8 mPa.s in Figure 5.15-b.

As stated before, D_{out} increases with η_{out}. Therefore, one would expect to observe a longer relaxation time τ at high η_{out}, as cell would have to relax from a more elongated state. However, our experimental measurements reported in 5.15-b document that τ decreases (as $1/\tau$ increases) with

the viscosity of the suspension medium. One possible explanation for such behavior could be energy dissipation as already proposed by previous studies in the literature [49]. We explain our surprising results by the fact that increased external η_{out} impacts energy dissipation making the cells relax more rapidly than when η_{out} is low. Figure 5.15-b shows the results for all the tested viscosities in both modes, where we report that for a given cell speed, $1/\tau$ increases (τ decreases) when η_{out} rises, for both relaxation types.

One may notice that our measurements of τ start around 129 ms, typically for η_{out} = 1.3 mPa.s and V_3 = 170 µm.s^{-1}, which is in good agreement with values previously reported in literature [27, 30, 49, 93] and predicted by the Kelvin-Voigt model. But they can also reach values as low as 4 ms, for η_{out} = 20.3 mPa.s and V_3 = 1500 µm.s^{-1}.

These lower τ values at higher viscosities and flow speed have also been reported for the starting shape of RBC by Prado et al [89]. Authors report values of τ as low as 30 ms for η_{out} = 5 mPa.s and a flow speed of 5.4 mm.s^{-1}. Baskurt et al [49] have also reported the dependency of τ upon the external medium viscosity, using ektacytometry, authors have noticed an increase of the relaxation time when increase η_{out}. They have reached τ = 30 ms for η_{out}= 29 mPa.s.

5.6 Conclusion

In this chapter, we presented a study of the behavior of healthy RBCs flowing passively in a microfluidic channel with oscillating width. We first documented the existence of two relaxation modes for the cell to return to its equilibrium shape at the exit of the last constriction. The two behaviors observed experimentally were retrieved using 2-D numerical simulations performed using Comsol Multiphysics®. Moreover, we presented a theoretical estimation of the local hydrodynamic stress that RBCs experience at the exit of the last geometrical constriction in conditions corresponding to the frontier between the two modes. We correlate this local stress to the RBCs elastic shear modulus μ estimated to be in a range of [4.2 – 9.66] µN.m^{-1} which is in good agreement with values from the literature [29, 30]. Finally, we investigated the dependency of D_{out} and τ upon the experimental conditions such as the cell velocity V_3, the main channel width W_o, as well as the external medium viscosity η_{out}. Indeed, we reported that D_{out} increased with the external viscosity η_{out} and the channel width W_o, whereas the relaxation time τ strongly dropped according to V_3/W_o and η_{out} as already reported in the literature [49, 89].

CHAPTER 6

ACTIVE CHARACTERIZATION OF RBCS USING ELECTRODEFORMATION

Contents

In this chapter, we used electrodeformation (ED) [117] as an alternative strategy to probe mechanically RBCs. We used dielectrophoresis (DEP) to trap healthy human Red Blood Cells (hRBCs) and then, by modulating the electrical field amplitude, RBCs were submitted to elongations and relaxations. We investigated the dependency of the RBC mechanical response upon the experimental parameters, such as the viscosity of the external medium η_{out}, the amplitude of the applied voltage ΔV, the duration of the solicitation t_{sol}, the number of solicitations N as well as the resting time t_{rest} between two solicitations. The impact of these parameters was evaluated through the analysis of both RBCs deformation index, D_1 and relaxation time, τ.

6.1 Dielectrophoresis

In 1951, Pohl [118] described the dielectrophoretic phenomenon as "the motion of suspensoid particles relative to that of the solvent resulting from polarization forces produced by an inhomogeneous electric field". Over the last two decades, Dielectrophoresis (DEP) theory and technology have matured sufficiently to be used in several applications such as biosensors [119], microfluidics [120], particle filtration [121] and nanoassembly [122]. Notably, DEP has found new applications in the field of microfluidics, for the manipulation of biological cells as, for example CTCs [123], RBCs

[124], parasited RBCs [125] .... The theory of DEP will not be fully presented here. A more thorough presentation can be found in the following reviews [126, 127].

The common theory presented in literature states that, in an inhomogeneous stationary AC electrical field, the time-average DEP force applied to an homogeneous spherical particle, such as bacteria and cells, is given by :

$$< \vec{F}_{DEP} >= 2\pi\epsilon_0\epsilon_m r^3 Re[CM(f)]\nabla E^2 \tag{6.1}$$

where ϵ_m is the relative permittivity of the external medium, ϵ_0 the permittivity of free space, r the radius of the particle, E the amplitude of the applied electric field and $Re[CM(f)]$ is the real part of the Clausius-Mossotti factor [128] given by:

$$CM(f) = \frac{\epsilon_p^* - \epsilon_m^*}{\epsilon_p^* + 2\epsilon_m^*} \tag{6.2}$$

in which ϵ_p^* and ϵ_m^* are the complex permittivities (defined in Eq. (6.3)) of the particle and the external medium respectively [128] and f is the frequency.

$$\epsilon_p^* = \epsilon_p - i\frac{\sigma_p}{\omega}, \epsilon_m^* = \epsilon_m - i\frac{\sigma_m}{\omega} \tag{6.3}$$

where ϵ_p and ϵ_m are relative permittivities of the particle and medium respectively, σ_p and σ_m their conductivities, i, the imaginary number (i^2 = -1) and ω the angular frequency of the applied AC field. Equation (6.1) shows that DEP force is ineffective when the electrical field is homogeneous ($\nabla E = 0$), and the direction of DEP force is not affected by the direction of the electrical field (E^2). Indeed, the orientation of the resulting DEP force is determined by the sign of the real part of the Clausius-Mossotti factor $Re[CM(f)]$. For $\epsilon_p > \epsilon_m$ (positive DEP), the cell is submitted to a force oriented towards high electrical gradient field zone and as a result, moves in this direction (Fig. 6.1-a). In contrast, for $\epsilon_p < \epsilon_m$ (negative DEP), the direction of the DEP force is towards the region of low electrical field gradient and therefore the cell moves towards areas of low electrical field gradient (Fig. 6.1-b).

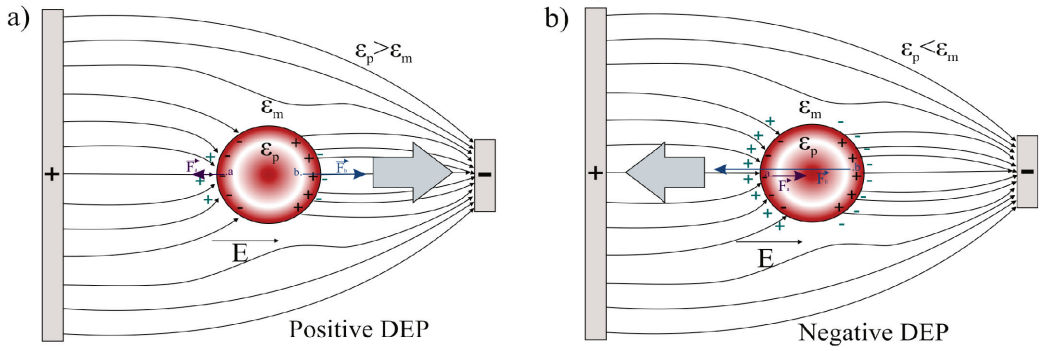

Figure 6.1: Schematic representation of (a) pDEP and (b) nDEP for a spherical particle in an inhomogeneous electrical field. Grey arrows indicate the direction of particle motion. Adapted from [129].

For RBCs, a single shell model is used [130], where an efficient effective complex permittivity ϵ_p^{*eff} is calculated using relationship (6.4) [120].

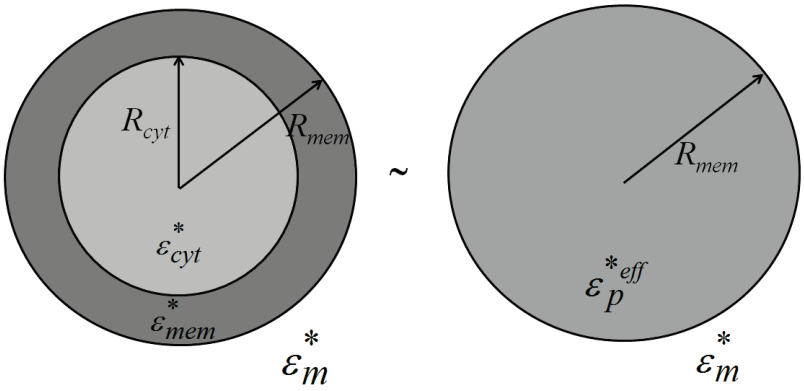

Figure 6.2: Single shell modelisation of a hRBC with permittivities ϵ^*_{cyt}, ϵ^*_{mem} in an external medium of permittivity ϵ^*_m. The RBC can equivalently be modelled as a sphere with inner effective permittivity ϵ_p^{*eff} in an outer medium of permittivity ϵ^*_m.

$$\epsilon_p^{*eff} = \epsilon^*_{mem}\left[\frac{\left(\frac{R_{mem}}{R_{cyt}}\right)^3 + 2\frac{\epsilon^*_{cyt}-\epsilon^*_{mem}}{\epsilon^*_{cyt}+2\epsilon^*_{mem}}}{\left(\frac{R_{mem}}{R_{cyt}}\right)^3 - \frac{\epsilon^*_{cyt}-\epsilon^*_{mem}}{\epsilon^*_{cyt}+2\epsilon^*_{mem}}}\right] \tag{6.4}$$

where (ϵ^*_{mem}) is the cell membrane complex permittivity, ϵ^*_{cyt} the encapsulated cytoplasm complex permittivity and R_{mem} and R_{cyt}, the external and internal radius of the cell membrane respectively as described in Figure 6.2.

Following this model, the Clausius-Mossotti factor can be expressed as [131]:

$$CM(f) = \frac{R_{mem}C_{mem}(\epsilon^*_{cyt}-\epsilon^*_m) - \epsilon^*_{cyt}\epsilon^*_m}{R_{mem}C_{mem}(\epsilon^*_{cyt}+2\epsilon^*_m) + 2\epsilon^*_{cyt}\epsilon^*_m} \tag{6.5}$$

where C_{mem} is the equivalent cell membrane capacity ($C_{mem} = 12.10^{-3}$F.m^{-2} [132]) and R_{mem} is the equivalent RBC radius ($R_{mem} = 3.5$ µm [132]).

To evaluate the impact of medium conductivity on the real part of the Claussius-Mossotti factor of RBCs ($Re[CM(f)]$), we used medium and cytoplasm permittivities equal to $\epsilon_m = 80.\epsilon_0$ and $\epsilon_{cyt} = 59.\epsilon_0$[132, 133]. The evolution of $Re[CM(f)]$ (calculated using equation (6.5) as a function of the medium conductivity is plotted in Fig 6.3. We chose the values of conductivity based on the conductivity measurements of the media used in this work. The value of 2.3 µS.cm^{-1} corresponds to the conductivity of the Gluc/Suc solution used as the DEP medium here, whereas the value 43 µS.cm^{-1} corresponds to this same DEP medium made more viscous by the addition of Dextran. As already described in literature, external medium conductivity has a fundamental impact on the real part of the Claussius-Mossotti factor. We can distinguish two main tendencies on the curves

representing $Re[CM(f)]$ as a function of f. For high conductivity value, *i.e.* for σ_m = 4300 µS.cm^{-1} in Fig. 6.3, $Re[CM(f)]$ remains negative regardless of the frequency used. In contrast for $\sigma_m \leq$ 430 µS.cm^{-1}, $Re[CM(f)]$ can have either negative or positive values depending on the frequency. As explained previously, this information is important as the sign of $Re[CM(f)]$ defines the frequency range where RBCs are submitted to pDEP and nDEP. As seen in Fig. 6.3, the frequency range where pDEP manipulation of RBCs is possible, is reduced by increasing the conductivity of the external medium. Moreover, we can also notice on the graph, that this conductivity also impacts $Re[CM(f)]$ value. The maximum value of $Re[CM(f)]$ decreases when increasing the external medium conductivity. $Re[CM(f)]$ maximum value reaches ~ 0.96 for σ_m = 2.3 µS.cm^{-1} whereas, it reaches only ~ -0.1 for σ_m = 4300 µS.cm^{-1}. As a result, the maximization of DEP forces requires to work with low conductivity medium. In this work, we were not able to measure experimentally this parameter, $Re[CM(f)]$. These measurements would permit having the real evolution of this parameter with the external medium conductivity, and thus evaluate the force to which cells are submitted during ED assays.

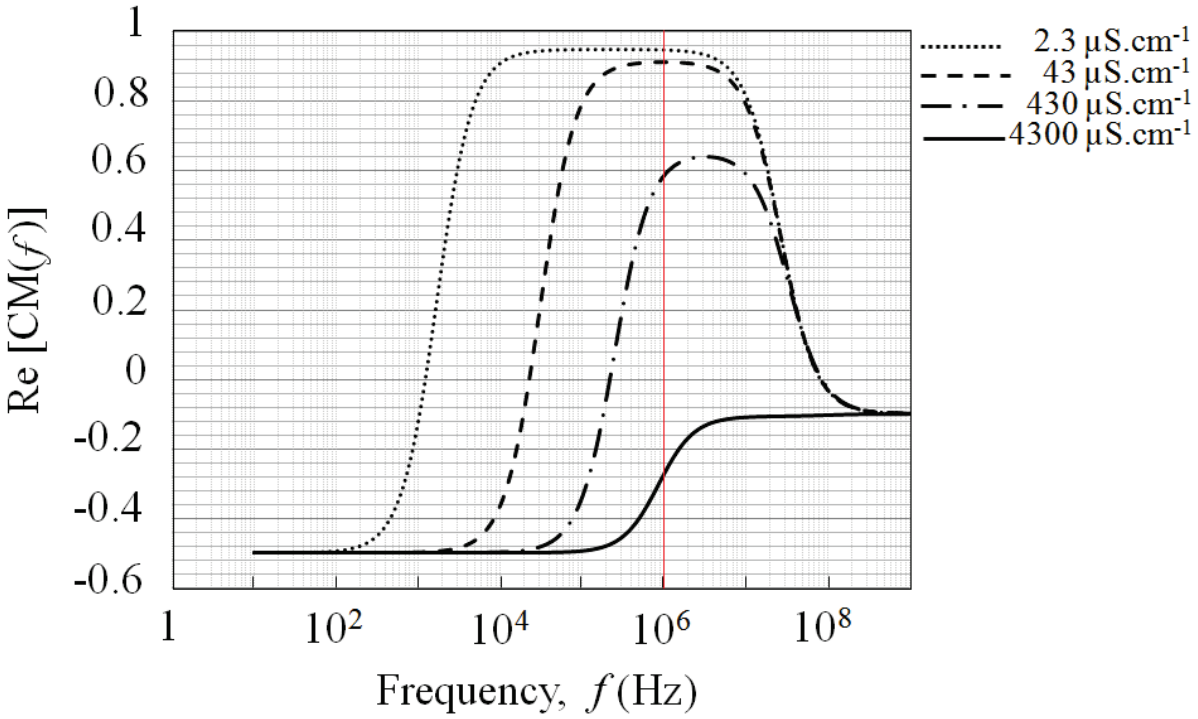

Figure 6.3: Representation of the real part of $CM(f)$ of a RBC as a function of the applied frequency for different medium conductivities. $Re[CM(f)]$ were calculated according to Equation 6.5 using Matlab®. $\epsilon_m = 80.\epsilon_0$, $\epsilon_{cyt} = 59.\epsilon_0$, $C_{mem} = 12.10^{-3}$F.m^{-2}, R_{mem} = 3.5 µm, σ_{cyt} = 0.31 S.m^{-1}.

6.2 Impact of the experimental conditions on the mechanical response of RBCs in ED assays

6.2.1 ED experiment and measurements

ED experiments were conducted at a frequency of 1 MHz where $Re[CM(f)]$ should be close to unity according to Fig. 6.3. Each ED experiment can be divided into three steps: first, cells were attracted to the electrode edges thanks to pDEP, then by increasing the signal amplitude, RBCs were elongated and finally, cells relaxed to their equilibrium shapes as the amplitude was decreased back to the initial amplitude value $\Delta V_0 = 2$ V (Fig. 6.4).

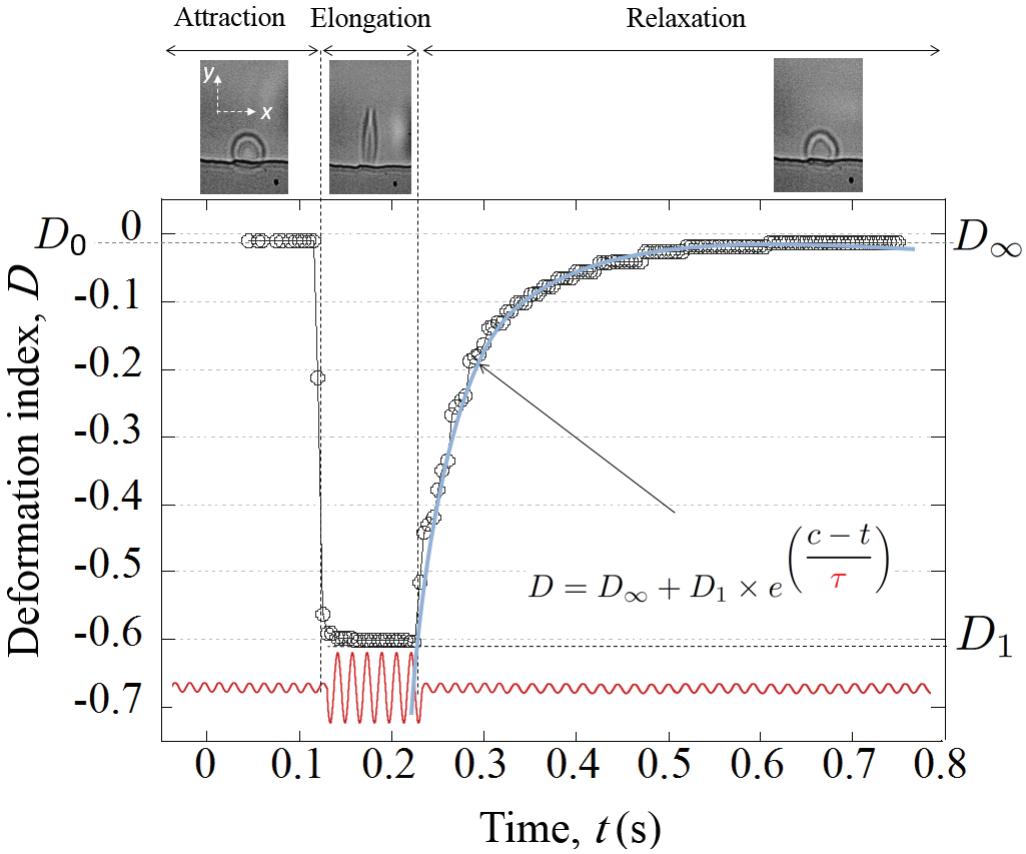

Figure 6.4: Typical deformation curve representing the deformation index D of a single RBC versus time during an ED cycle. Microscopic images of a cell at different deformation states are also reported. The blue curve is the exponential fit obtained from the experimental data during the relaxation process. The red curve displays a schematic representation of the applied voltage $\Delta V(t)$ (not to scale).

The low amplitude value $\Delta V_0 = 2$ V was chosen to attract the cells to the electrode edges *via* dielectrophoresis without inducing any RBCs deformation, as shown in Fig. 6.5. The deformation index D_0 associated with this amplitude is used as a reference value for the experiment.

When the amplitude was raised to ΔV_1 for a duration t_{sol}, we observed an elongation of RBCs

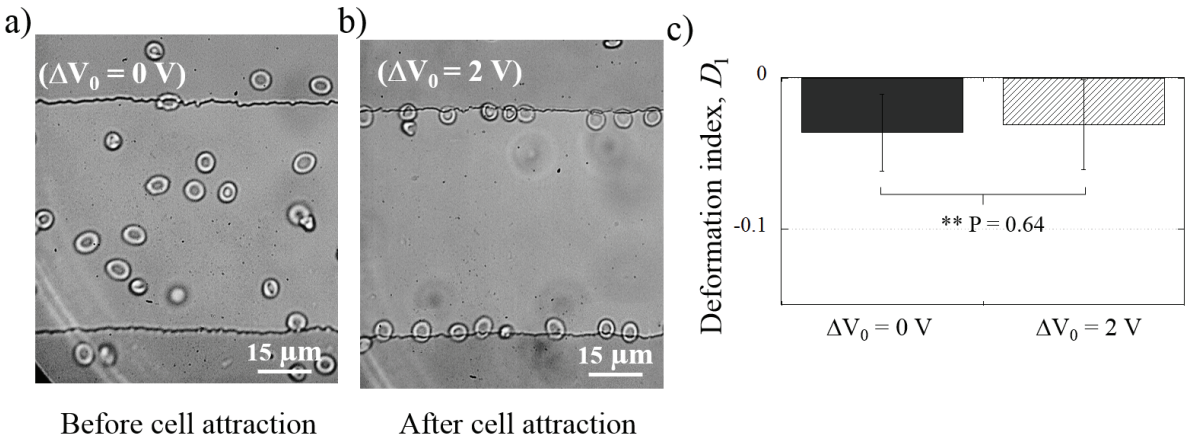

Figure 6.5: Microscopic images showing RBCs: (a) before (ΔV_0= 0 V) and (b) after application of the electrical field (ΔV_0= 2 V). (c) Measurements of the associated deformation indexes before and after application of a voltage amplitude ΔV_0= 2 V.

in the y-direction and their thinning in the x-direction that globally leads to a drop of D to a local minima D_1. At the end of the duration t_{sol}, the amplitude was turned down to its lowest value (ΔV_0 = 2 V) and we observed the cells relaxing towards their equilibrium resting shape (Fig. 6.4). From the relaxation part of the curve, we can retrieve the relaxation time, τ, by an exponential fit of the curve D = f(t), as well as the deformation index corresponding to the equilibrium shape, D_∞.

We may notice in Fig. 6.4 that the response time of RBCs to the electrical fields, *i.e* the time needed for the cell to reach its local maximum deformation, when the amplitude is increased to ΔV_1, is very short (~ 5-10 ms) compared to its relaxation time τ (~ 80 ms). The applied electrical force being dominant compared to the mechanical properties of the cell, the response time to this electrical solicitation is mainly dictated by the electrical device. By opposition, during the relaxation process the electrical force is suddenly decreased and the RBC relaxes depending on its mechanical properties.

In the rest of this chapter, we will focus on the evolution of D_1 and τ as a function of experimental conditions: ΔV_1, t_{sol}, η_{out}, t_{rest} and N. We chose not to give the electrical field values as for IDEs, this field is not uniform. We rather chose to give to the reader the information of the amplitude of the signal ΔV_1. We remind the reader that the inter-electrode gap is 85 µm.

6.2.2 Influence of the external medium: Glu/Suc solution

In addition to having a low conductivity, the chosen medium has to be isotonic (300 mOsm/kg) and at pH = 7.4 to be suitable for RBCs. Among various buffers reported in literature such as PBS 1x and HEPES[1] [77], we selected the Glu/Suc medium as it was the most suitable for ED experiments (low conductivity ~ 2.3 µS.cm^{-1}, isotonicity [101] and pH = 7.4).
Despite both its compatibility to ED experiments and suitability for RBCs, we noticed that cells

[1] *HEPES* : 2-[4-(2-hydroxyethyl)piperazin-1-yl]ethanesulfonic acid

mechanical properties evolved after staying in the Glu/Suc solution for time longer than 2 h. We monitored the evolution of RBCs maximal deformation D_1 and relaxation time τ versus incubation time in this medium for a sample of RBCs staying in a Glu/Suc solution. Figure 6.6 illustrates the evolution of D_1 and τ versus time. We notice that RBCs remain unaltered after 1 h kept in this medium as their maximal deformation and relaxation times did not show any significant differences. Starting from 2h of incubation, RBCs maximal deformation D_1 decreases and their relaxation time τ increases significantly. To avoid any bias in the measurements, all experiments were conducted using RBCs suspensions freshly prepared from the mother solution for each tested condition (waiting time below 1 h).

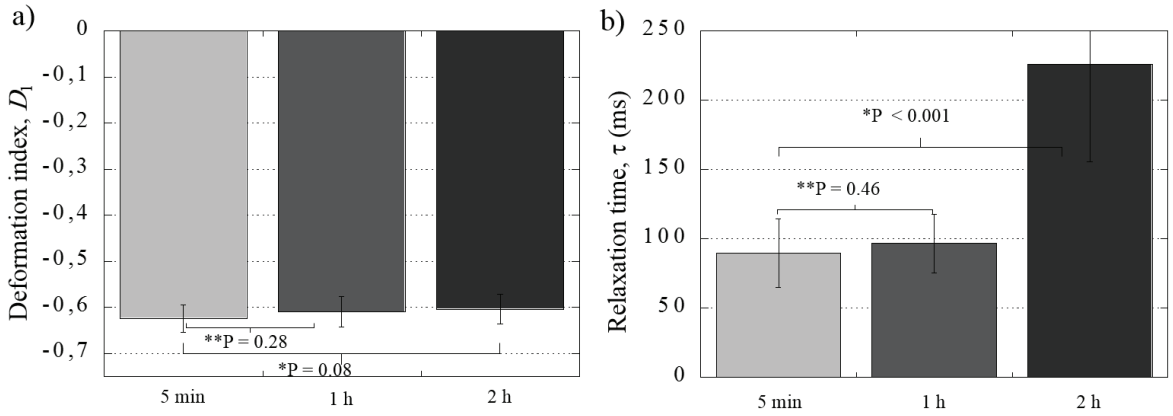

Figure 6.6: Evolution of RBCs maximal deformation D_1 and relaxation time τ with time spent in the Glu/Suc solution. ΔV_0= 2 V, ΔV_1= 48 V, $\eta_o ut$ = 1.3 mPa.s. Error bars represent the standard deviation.

6.2.3 Influence of the amplitude of solicitation ΔV_1

The dependency of the deformation D_1 upon the increase of the amplitude ΔV_1 is represented in Figure 6.7. We can notice that D_1 decreased from -0.1 to -0.62 when ΔV_1 was increased from 8 to 48 V. We can observe that the largest D_1 variation is seen between 8 and 24 V. Above 32 V, D_1 variation is very low and seems to saturate showing that RBC membrane is reaching its elasticity limit. Indeed, for amplitude above 48 V, we observed RBC lysis. The evolution of D_1 with ΔV_1 is consistent with the increase of F_{DEP} due to electrical field increase (equation (6.1)).

We evaluated the impact of the parameter ΔV_1 on the relaxation time of RBCs using two different amplitude values ΔV_1 = 32 V and ΔV_1 = 48 V. Figure 6.8-a represents in boxplots[2] the statistical results for the relaxation time of the two investigated conditions. It illustrates the fact that RBCs submitted to ΔV_1 = 48 V took longer times to relax to their equilibrium shape compared to those at condition

[2]A boxplot is a graphical representation of statistical data. In a typical box plot the top of the rectangle indicates the third quartile, a horizontal line near the middle of the rectangle indicates the median, and the bottom of the rectangle indicates the first quartile (50 % of points are inside the box). A vertical line extends from the top of the rectangle to indicate the maximum value, and another vertical line extends from the bottom of the rectangle to indicate the minimum value. Values exceeding 3/2 the inter-quartile interval are considered as outliers and represented as separated points.

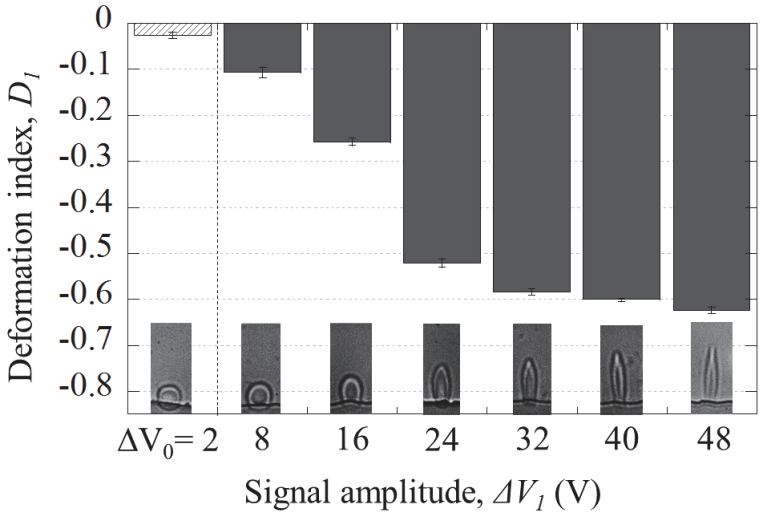

Figure 6.7: Evolution of hRBC maximum deformation D_1 as a function of the voltage amplitude. Microscopic images illustrates the deformation of cells at each voltage amplitude. Each error bar represents the standard error which is calculated from roughly 12 cells. η_{out} = 1.3 mPa.s, t_{sol} = 100 ms, N=1, f = 1 MHz.

ΔV_1 = 32 V (the difference between these two values was $\Delta\tau$ = 22.5 ms which is a value statistically significant as demonstrated by the T-test). In parallel, we also monitored the deformation D_1 for these two conditions (Fig. 6.8-b). As shown previously, we obtained an elongation index smaller for the lower ΔV_1 value. The difference between the two values was $\Delta D_1 \sim 0.02$, which is also statistically significant.

These findings point out the dependency of τ upon D_1, as more deformed cells take longer times to relax to their resting shape. This result is coherent with the calculation of Hochmuth and Evans [27] for viscoelastic materials. Indeed, equations (6.6) - which is equation (2.13) from Chapter 2 with $L = 2b$ et $W = 2a$ - and (6.7) describe the exponential decay of the cell deformation versus time as follows:

$$\frac{\left(\frac{2b}{2a}\right) - \left(\frac{2b}{2a}\right)_\infty}{\left(\frac{2b}{2a}\right)_m - \left(\frac{2b}{2a}\right)_\infty} = e^{-t/\tau} \tag{6.6}$$

Using our definition of the deformation index D, which has negative values when the cell is stretched, we get an exponential growth for the relaxation time and the equation (6.6) becomes:

$$\frac{D - D_\infty}{D_1 - D_\infty} = e^{t/\tau} \tag{6.7}$$

For a given deformation D, when the maximum elongation D_1 is increased (due to the increase of ΔV_1), it results in the decrease of $e^{t/\tau}$ and thus the rise of τ.

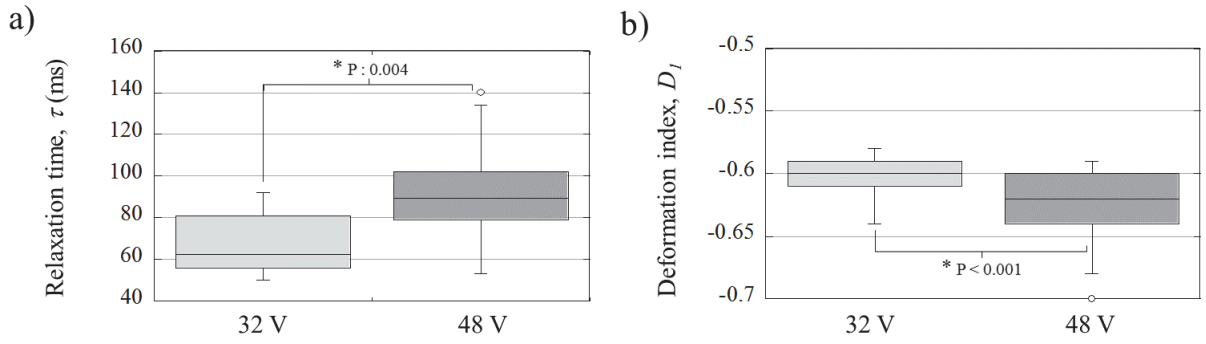

Figure 6.8: (a) Relaxation time τ and (b) deformation index D_1 for two experimental conditions ΔV_1 = 32 and ΔV_1 = 48 V. (η_{out} = 1.3 mPas, t_{sol} = 100 ms, f = 1 MHz, N = 1). Each boxplot represents roughly 15 RBCs.

The values for the relaxation time τ corresponding to the saturated deformation index of cells (ΔV_1 = 48 V) is ~ 90 ms. These values are in good agreement with values reported in literature $\tau \sim$ 100 ms [27] which represents the predicted value of the Kelvin-Voigt model for a viscoelastic material, which is calculated by $\tau = \eta_{mem}/\mu$, where η_{mem} and μ are the viscosity of the RBC membrane and the cell shear modulus, respectively. These values correspond also to those obtained in this thesis using passive microfluidics in the case of low velocities and low external medium viscosities η_{out} (see Chapter 05) and other techniques in the literature [27, 30, 49, 93, 117] . For elongation smaller than the maximum elongation that RBC can withstand, as for example for ΔV_1 = 32 V, τ is lower than 90 ms.

Based on the results presented above, we can conclude that in order to compare the relaxation time of different RBC samples, it is necessary that cells undergo the same initial elongation. In other words, for the measurements of τ, one critical parameter is the initial elongation of the cell D_1 and not the amplitude ΔV_1.

6.2.4 Effect of the external viscosity η_{out}

In this section, we investigated the influence of different external viscosity conditions: η_{out} = 1.3, 16.4 and 31.5 mPa.s. These values correspond respectively to a Glu/Suc solution, Glu/Suc/Dex4.5% solution and Glu/Suc/Dex9% solution. The evolution of D_1 as a function of ΔV_1 for two conditions (η_{out} = 1.3 and 31.5 mPa.s) is presented in Fig. 6.9. Experimental results show that, for identical voltage amplitude, cells in the Glu/Suc solution, *i.e.* η_{out} = 1.3 mPa.s, are more deformed than their counterparts in the Glu/Suc/Dex9% solution, *i.e.* η_{out} = 31.5 mPa.s. For η_{out} = 1.3 mPa.s, a deformation index D_1 below -0.6 is reached for ΔV_1 = 40 V, whereas for the more viscous solution, this deformation index value is reached at a higher electrical field (*i.e.* ΔV_1 = 48 V). As already explained previously, F_{DEP} depends both on the value of the real part of the Claussius-Mossotti factor and the square root of the electrical field. We measured that σ_m = 43 µS.cm^{-1} for η_{out} = 31.5 mPa.s and σ_m =

2.3 µS.cm^{-1} for η_{out} = 1.3 mPa.s. This difference of conductivity results in different $Re[CM(f)]$ curves (Fig. 6.3). At 1 MHz, we calculated that $\frac{Re[CM(f)]_{Glu/Suc}}{Re[CM(f)]_{Glu/Suc/Dex9\%}}$ = 1.033, which cannot probably explain alone this difference in deformation index observed for $\Delta V_1 \leqslant$ 40 V. Another explanation could be a difference of permittivity value between these two media. It would be interesting in future works to estimate the respective permittivities of these medium. One way would be to use electrical impedance spectroscopy.

However, we note that for ΔV_1 = 48 V, RBCs in both buffers reach their maximal deformation (D_1 = -0.62). Thus in the following, we decided to compare the relaxation times at conditions giving identical D_1, *i.e.* at ΔV_1 = 48 V.

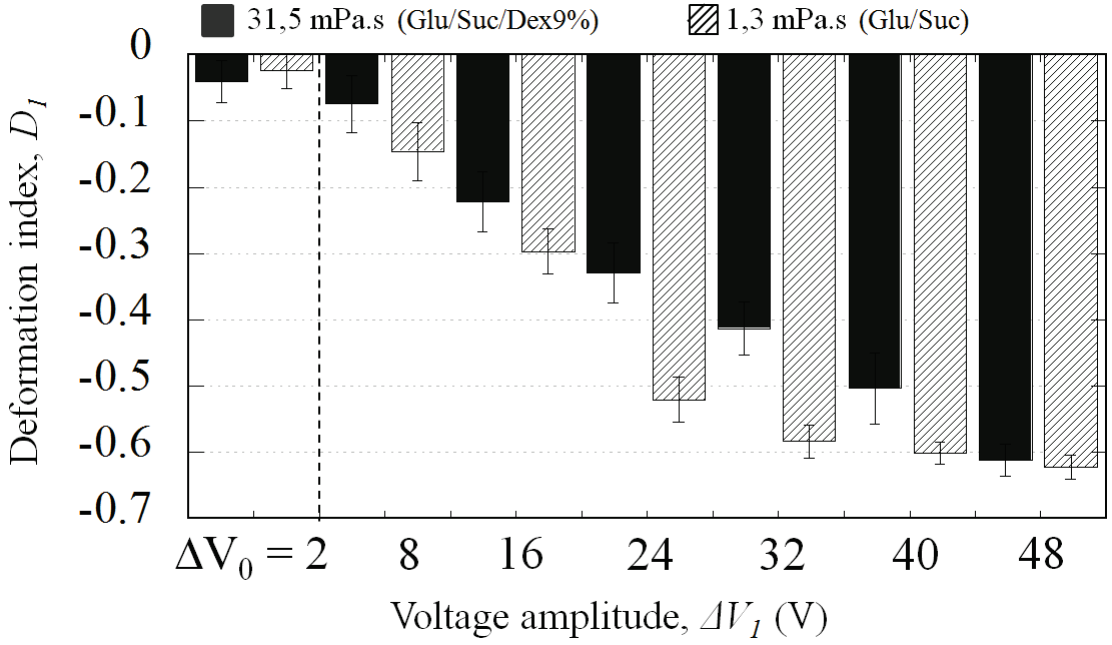

Figure 6.9: Evolution of RBCs deformation index D_1 with ΔV_1 for two different external medium viscosities: η_{out} = 1.3 mPa.s and η_{out} = 31.5 mPa.s. Each error bar represents the standard deviation which is calculated from roughly 12 cells. t_{sol} = 100 ms, N=1, f = 1 MHz.

To assess the impact of the external viscosity η_{out} on τ, we have tested three different viscosities: 1.3, 16.3 and 31.5 mPa.s. First, we verified that RBCs were submitted to the same deformation index, when applying ΔV_1 = 48 V for the three conditions (Fig. 6.10-a). This Figure shows that there is statistically no difference of D_1 value for the three different external viscosities tested.

The evolution of τ as a function of η_{out} is plotted in Fig 6.10-b. Results show that η_{out} also affects the mechanical response of RBCs. Indeed, this figure illustrates that for equivalent deformations, RBCs relaxed slower in the more viscous fluid. Surprisingly, this finding is contradictory with what was presented in Chapter 5, when using passive microfluidics. However, as already discussed in Chapter 3, previous results from Prado et al.[89] suggested that an inversion of the evolution of τ versus η_{out} occurs at very low flow speed. Indeed at high flow rate, τ decreases when increasing η_{out}

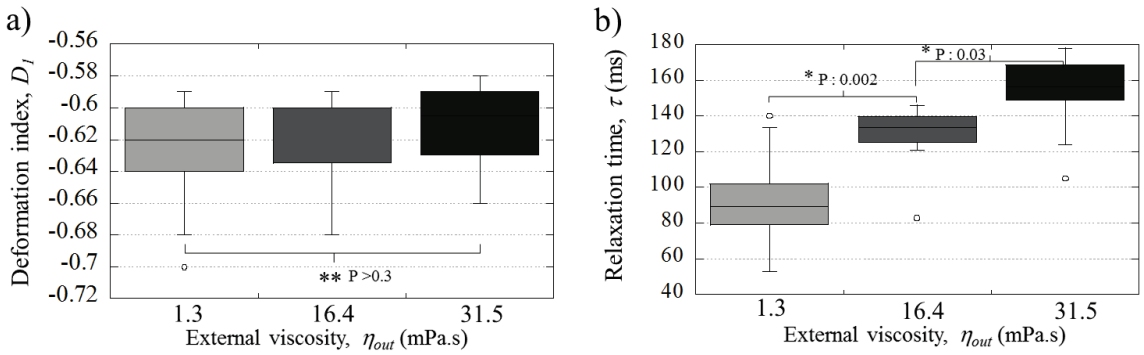

Figure 6.10: Impact of the external buffer viscosity η_{out} on the measurements of (a) D_1 and (b) τ (at ΔV_1 = 48 V, t_{sol} = 100 ms, N = 1, f = 1 MHz). Each boxplot represents roughly 12 RBCs.

- which is what we observed in passive microfluidics - whereas the opposite is observed at lower flow velocities, which is consistent with our ED measurements where RBCs flow speed in null. These published results would reconcile both our observations. At no flow condition (ED), we may explain this longer relaxation time by a need of longer times to push a more viscous surrounding liquid while RBCs are relaxing to their original discocyte shape. For the rest of this chapter, we used a Glu/Suc buffer with a viscosity of 1.3 mPa.s.

6.2.5 Influence of the solicitation duration t_{sol}

In this section, we evaluated the influence of the solicitation duration, *i.e.* the time during which cells are elongated before relaxing (t_{sol} = 100 ms, 1500 ms and 5000 ms) on D_1 and τ. To ensure all cells were submitted to the exact t_{sol} only once, each condition of t_{sol} was conducted on a separate new sample and cells were changed after each solicitation. Experimental results show that t_{sol} have no influence on D_1 as highlighted in Figure 6.11-a. RBCs showed the same maximal deformation regardless of the duration of solicitation t_{sol} as this maximal deformation is mainly imposed by the electrical device.

Previous studies in literature [134] where authors used small micropipettes (diameter below 1 µm) to deform cells, stated that RBC membrane presents a visco-elastic behavior for solicitation periods up to 5 min. For longer or higher strains, a permanent deformation of the RBC is observed. Being well below this limit, we expect the total recovery of their initial resting shape after RBC solicitations. However in the case of ED assays, t_{sol} seems to affect cells stationary shape D_∞. Results highlighted in Figure 6.11-b show a comparison of D_∞ of the three tested conditions to the initial deformation D_0. We can notice that D_∞ is not affected for t_{sol} = 100 ms (as shown with T-test), RBC recover totally their initial shape and thus have the same deformation state post-relaxation. For for t_{sol} = 1500 and 5000 ms, D_∞ showed significant yet not very important differences. RBCs that were elongated for longer times did not seem to recover totally their initial shape or may need longer times to reach a total shape recovery. When submitted to electrical field, complex phenomena occur on the cell membrane such as the appearance of pores that can be transient or permanent. These alterations

may modify cell mechanical characteristics and so stationary shape. The corresponding relaxation times have been extracted and presented in Fig. 6.12. Experimental data show that τ is directly linked to the duration of the applied solicitation. Indeed, while varying the parameter t_{sol}, we found that τ tends to increase significantly. Figure 6.12 shows that τ is around 80 ms for short solicitations (with t_{sol} = 100 ms) and increases to 120 ms at t_{sol} = 1500 ms before reaching 250 ms when t_{sol} = 5000 ms. At the time of the writing of this manuscript, we have no explanation on what makes τ increase with t_{sol}. We think that this difference may be due to an alteration of the membrane and its cytoskeleton resulting from the long solicitations and which is also reflected on the relaxed shape D_∞. However, in order to select the best experimental conditions to evaluate RBCs mechanical properties using ED, it is important to use a solicitation of 100 ms.

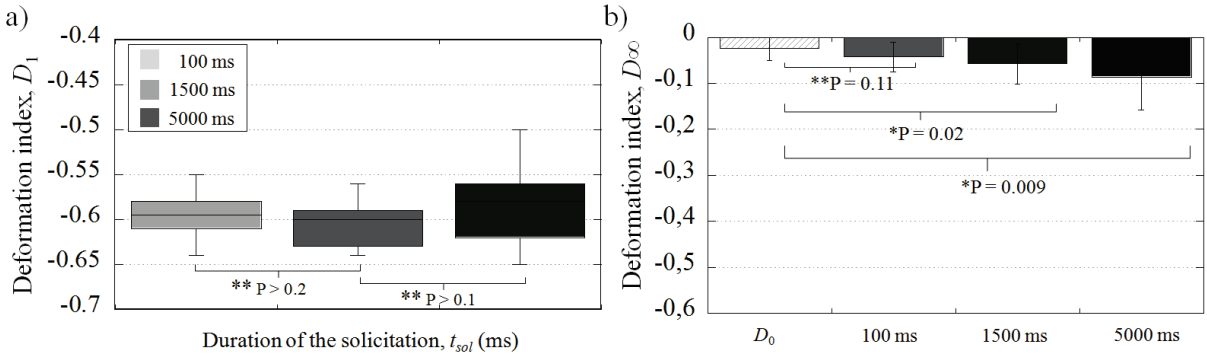

Figure 6.11: Influence of the solicitation duration t_{sol} on (a) D_1 and (b) D_∞. (ΔV_1 = 48 V, η_{out} = 1.3 mPa.s, N = 1 and f = 1 MHz). Each boxplot represents roughly 12 RBCs.

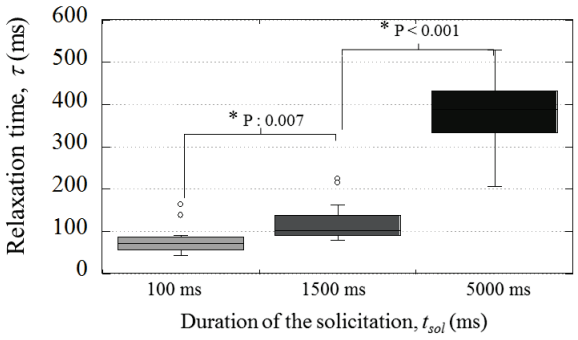

Figure 6.12: Influence of the solicitation duration t_{sol} on τ. (ΔV_1 = 48 V, η_{out} = 1.3 mPas, N = 1 and f = 1 MHz). Each boxplot represents roughly 12 RBCs.

6.2.6 Impact of the number of cycles N and the resting time t_{rest}

We aimed here at assessing the mechanical behavior of RBCs when submitted to repetitive solicitations. In this paragraph, we evaluated the influence of the number of cycles N as well as the resting time between two solicitations, t_{rest}. To realize this, we exposed RBC samples to a series of

periodic solicitations with N ranging from 40 to 400 cycles and t_{rest} ranging from 100 to 5000 ms. We submitted RBCs to this repetitive solicitation and then measured their relaxation time during the last cycle. Corresponding results are presented in Figure 6.13. For t_{rest} = 5000 ms and 1000 ms, we found that the deformation index D_1 remains constant even after 400 cycles (Fig. 6.13-a and c). In contrast, we can observe from Figures 6.13-b and d, a different behavior for the relaxation time. While the relaxation time τ remains steady until N = 200, we can see that for more numerous solicitations (starting N = 300), τ starts to increase, reaching τ = 164 ms and 177 ms at N = 400, for t_{rest} = 5000 and 1000 ms respectively.

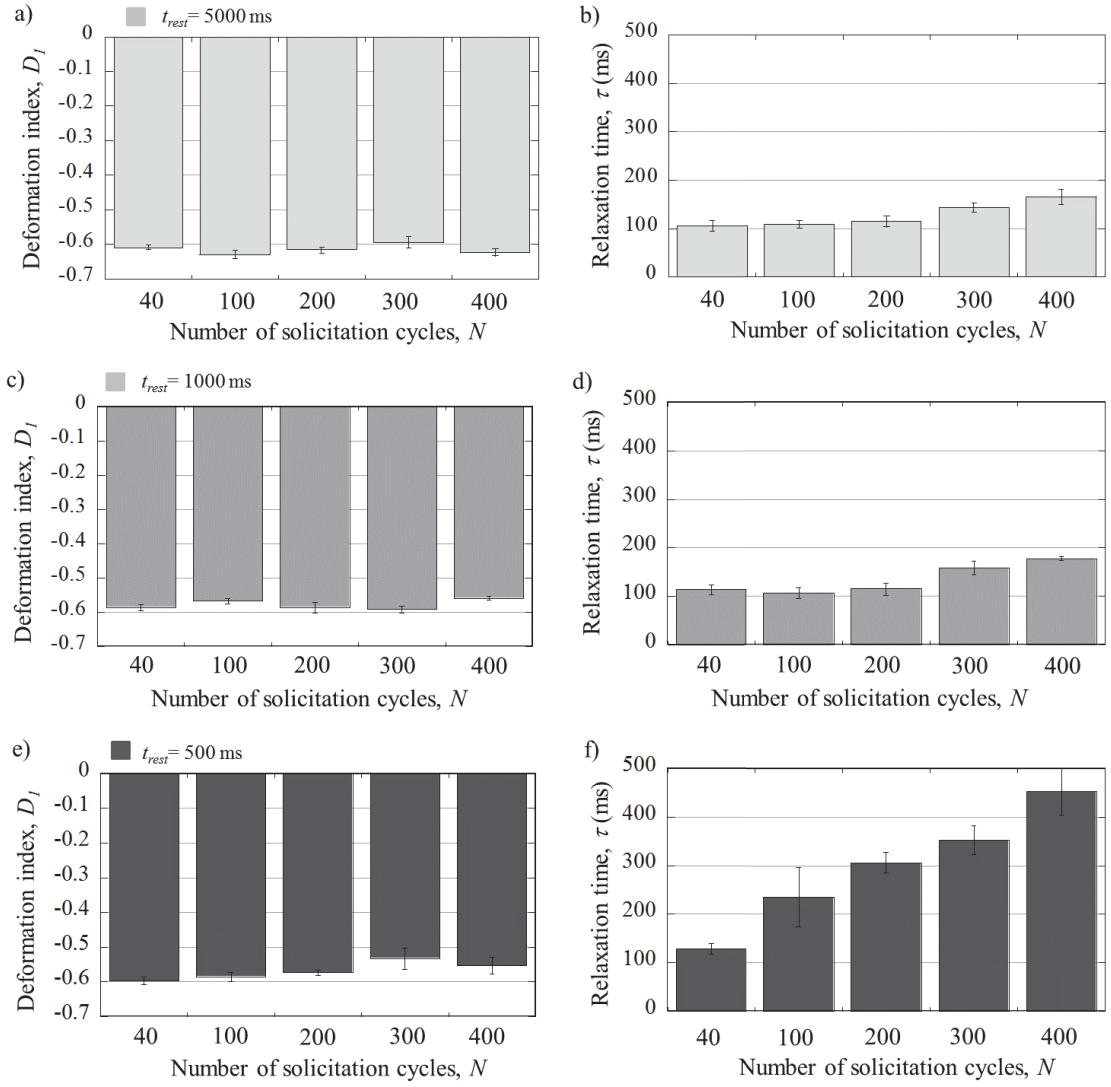

Figure 6.13: Evolution of D_1 and τ after a series of solicitations separated by: (a) and (b) 5000 ms, (c) and (d) 1000 ms and (e) and (f) 500 ms resting periods (t_{rest}). η_{out} = 1.3 mPa.s, t_{sol} = 100 ms and f = 1 MHz. Each error bar represents the standard error which is calculated from roughly 12 cells.

For t_{rest} = 500 ms (Fig. 6.13-e), we noticed that RBC deformation index D_1 is constant until 200

cycles and then starts to decrease, indicating an alteration of RBC behavior. However, this alteration is very weak ΔD_1 = 0.05. In comparison, we observed a steady increase of the relaxation time with the number of cycles until reaching ~ 450 ms at 400 cycles (Fig. 6.13-f). We may also notice that at N = 400 cycles, for both conditions t_{rest} = 500 ms and 1000 ms, both samples are at the same deformation index (D_1 = -0.55). However, RBCs did not experience the same relaxation times, τ = 450 ms and 177 ms respectively. From these results, we can conclude that the relaxation time τ seems to be a more sensitive parameter than the maximal deformation D_1 to evaluate difference in RBC mechanical properties. The reason for this, is that the deformation is usually imposed by the solicitation technique, while the relaxation is dictated by the cell properties. Recent work [135] has been done on RBCs fatigue based on their change of shape after reciprocated mechanical stress using a microfluidic channel. Authors found that, depending on the cells, complete RBC fatigue start to appear after the 500^{th} cycle which is in good agreement with our findings. Authors were focused at complete fatigue of RBC *i.e.* very small or inexistent recovery after the elongation, whereas, our work senses the debut of the fatigue. This difference may explain the slightly higher values reported comparing to our results. We also proved that - in addition to the effect of all the parameters shown earlier (ΔV_1, η_{out} and t_{sol}) - the resting period t_{rest} is also an influencing parameter for the determination of RBCs fatigue. Hence, not only the number of solicitation cycles N is important, but the frequency at which these solicitations were conducted as well.

These findings highlight that τ can be used to sense very finely RBCs mechanical properties.

We can also see from Figure 6.13 that, with experimental conditions t_{sol} = 100 ms, ΔV_1 = 48 V and t_{rest} = 500 ms, RBCs are altered faster than for $t_{rest} \geq$ 1000 ms during repetitive solicitation. It is therefore mandatory, when using ED to measure relaxation time, to assess conditions where no alteration of RBCs mechanical properties is induced by experimental conditions. Therefore, we can also state that for the ED experiments conducted with conditions, t_{sol} = 100 ms, ΔV_1 = 48 V and $t_{rest} \geq$ 1000 ms, RBCs are not altered by experimental conditions for $N \leqslant 200$ cycles. Indeed, we found relaxation times consistent with the values reported in literature.

6.3 Conclusion

We have highlighted the dependency of RBCs mechanical response upon the experimental conditions used during an ED assay. To our knowledge, this is the first time that such a thorough investigation of the influence of experimental parameters in ED has been carried out. In the case of ED assays, these experimental parameters are (t_{sol}, t_{rest}, N), as well as the initial elongation D_1 (resulting from the initial applied voltage ΔV_1) and the viscosity η_{out} of the external medium. We showed that in order not to affect the mechanical properties of cells by the application of an electrical field, it is necessary to carry out such assays conditions t_{sol}= 100 ms, ΔV_1= 48 V, t_{rest}> 500 ms, in the case of the electrode configuration used in this thesis. The modification of the electrode dimensions may

modify these optimized parameters. Besides, we also showed that the relaxation time seems to be a more sensitive parameter to monitor RBCs mechanical properties than the deformation index D_1. All these results lead to the conclusion that the relaxation time measured with ED presents a great potential as a biomarker to assess modification of RBC deformability among a given sample.

CHAPTER 7

DISCRIMINATION OF MECHANICALLY IMPAIRED RED BLOOD CELLS

Contents

In this chapter, we aimed at the evaluation of two approaches to distinguish mechanically impaired RBCs. First, for the passive approach, we investigated the use of Oscillating Width Constrictions (OWC) geometry characterized in Chapter 5 to study the behavior of healthy RBCs (hRBCs) and thermally rigidified RBCs (T-rRBCs). Then, we investigated the impact of the constrictions dimensions and compared the OWC to other configurations (i) a Unique and Long Constriction (ULC) and (ii) an OWC with longer constrictions (OWCLC). Next, we varied the dimensions of the enlargements by testing (iii) an OWC with longer enlargements (OWCLE), (iv) an OWC with wider enlargements (OWCWE) and finally (v) an OWC with wider and longer enlargements (OWCWLE). To confront the six tested geometries, we evaluated potential biomarkers for cell discrimination such as their speed V, deformation index D and relaxation time τ. In contrast, for the active approach, we used ED technique with the optimized parameters already exposed in Chapter 6 to perform the distinction of altered RBCs by artificial fatigue and heating protocol.

7.1 Characterization of the rigidified RBC samples

As already mentioned in Chapter 4 (section 4.1.2), throughout this work, we tested two rigidification protocols to produce mechanically impaired RBCs. The first protocol consisted in treating RBC with GA molecule. Three RBC samples treated with the same amount of GA (0.125 % v/v) in three different

experiments were injected in a OWC geometry and the videomicroscopic recording were analyzed according to the image analysis already described. Figure 7.1-a presents D_{out}, the deformation at the exit of the OWC geometry for the three experiments, all the other conditions (external viscosity, geometry and flow speed) being identical. The graph shows that although GA-rRBCs present some extension at the exit in the two first experiments, in the last experiment, GA-rRBCs seem to be plastic as they present no deformation at the exit ($D_{out} \sim 0$, $i.e.$ cells exited the OWC in their discocyte form). Although we used the same amount of GA in the same conditions, results were not reproducible. The second rigidification protocol consisted in a thermal process (heating at 50° C for 15 min) . The same reproducibility test was performed on three different experiments. The results presented in Figure 7.1-b show a good reproducibility of the thermal treatment. We may also notice that error bars are more important for the GA protocol comparing to the thermal one, revealing a higher variability among GA samples. Due to its reproducibility, the thermal treatment will be used to rigidify RBCs in the following experiments.

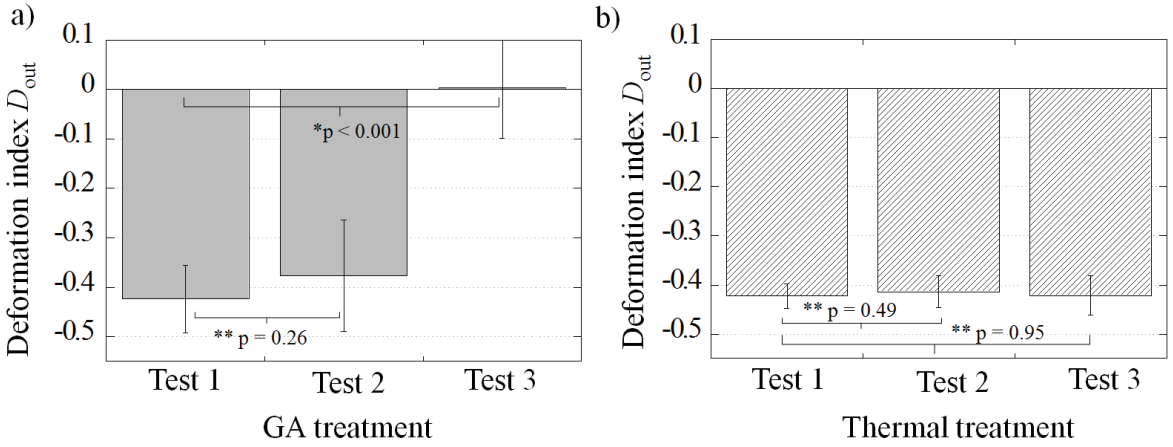

Figure 7.1: Deformation index D_{out} at the exit of the OWC geometry showing the reproducibility of the rigidification protocol for three different experiments: (a) using the GA protocol and (b) using the thermal heating process. Error bars represent the standard deviation. Each sample contains roughly 15 cells. η_{out}= 31.5 mPa.s

To characterize the amount of rigidification produced by the thermal process, we used the pressure drop technique already detailed in the literature [94, 95]. This technique allows the characterization of the volume and/or rigidity of cells. We used an optimized version of the geometry used by Abkarian et al. [94], as previous studied in the laboratory [136] have shown an increase of the sensitivity, when the virtual interface is located in a more confined cavity, as shown in Figure 7.2-a. One may notice that in our new configuration, the interface in not flat, however, the calibration curve is linear on the range of pressure of interest (Fig. 7.2-b).

Results from a typical experiment performed on a hRBC is shown in Figure 7.2-c. We can see the deformation curve and the associated pressure drop measurement corresponding to the time lapse

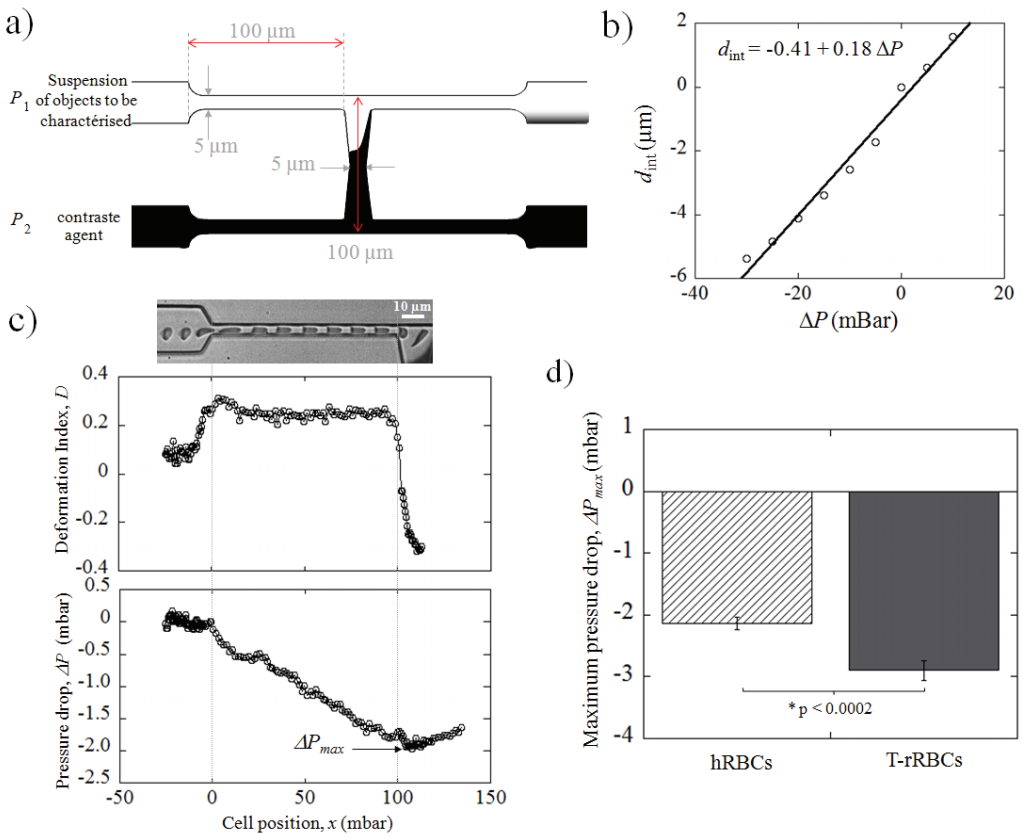

Figure 7.2: (a) Schematic representation of the pressure drop geometry used for the characterization of the rigidified samples. The important dimensions are reported on the scheme, the 4 branches being symmetrical. (b) A typical calibration curve, which allow the conversion of the virtual interface displacement d_{int} into a pressure drop ΔP. (c) Sequence of deformation associated with the passage of a hRBC inside the pressure drop device. The evolution of the deformation index D and the pressure drop ΔP associated are also presented as a function of the cell position x. The origin of the graphs has been arbitrarily set to be the entry of the constriction. η_{out} = 31.5 mPa.s, P_1 = 300 mBar et P_2 = 320 mBar. (d) Measurement of the maximum pressure drop ΔP_{max} of hRBCs and T-rRBCs. Error bars represent standard deviation calculated from roughly 30 cells for hRBCs and roughly 60 for T-rRBCs.

sequence of deformation. It appears that the maximum pressure drop (noted ΔP_{max}) is reached by the cell as it exits the channel as already reported [94, 104]. Experimental results issued from the pressure drop measurements of healthy and thermally rigidified RBCs reveal a small yet significant difference between the two probed samples (Figure 7.2-d). We can conclude that although T-rRBCs deform when flowing in close fitting channels, they present altered mechanical properties compared to hRBCs. This small variation of cell deformability is interesting for us as it could be a good model to test the sensitivity of our approaches. In the context of malaria diagnosis, the detection of ring infected RBCs (where the parasite is in a early stage of maturation) remains a challenge to tackle, as they present very few deformability difference with hRBCs. Therefore, we prefer to evaluate the relevance of our different techniques using a RBC sample with small mechanical alterations. [].

7.2 Discrimination of impaired RBCs using passive microfluidics

7.2.1 RBCs flow in the OWC geometry

In the following sections, we will start by reminding our reference geometry OWC. Then, we will describe how we retrieve all the parameters used to differentiate hRBCs and T-rRBCs. All the experiments in this section were conducted at an external medium viscosity η_{out} = 31.5 mPa.s. Thus, all the cells experienced a stretching behavior at the channel exit; they undergo an elongation at the exit D_{out}, which is extracted as well as the associated relaxation time τ.

7.2.1.1 Cell deformation

The OWC geometry is represented in Figure 7.3, the design and dimensions have already been introduced in Chapter 5. The main channel width W_o was set to 50 µm to minimize cell clogging in the geometry. The flow of various samples of RBCs through this geometry was studied and several potential parameters were considered for the distinction of mechanically impaired RBCs. Some of these parameters are extracted from cell deformation while others are related to cell transit velocity.

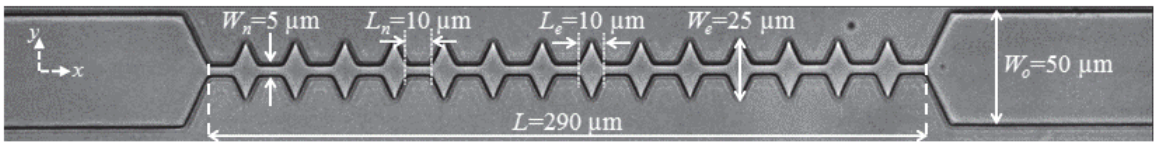

Figure 7.3: Microscopic image of the OWC geometry indicating the different dimensions. The height of the channel is set to 5 µm.

Two different samples (hRBCs and T-rRBCs) were flown into the OWC geometry and their deformation parameters D_{min}, D_{max}, ΔD and D_{out} were extracted and compared in Figure 7.4. We can notice from Figure 7.4-a, that the maximal deformation D_{max}, corresponding to the shape of cells being compressed inside a constriction, is statistically larger for hRBCs than for T-rRBCs. In contrast, both samples experience the same deformation D_{min} in the enlargements. Consequently, hRBCs have a larger deformation amplitude ΔD than their rigidified counterparts. These findings are coherent with the mechanical characterization detailed in section 7.1.

Besides, we have also compared the cell deformation at the exit, D_{out}, for both samples, as shown in Figure 7.4-b. This boxplot represents D_{out}, pooled over the different pressure conditions studied, for hRBCs and T-rRBCs. It shows that D_{out} for hRBC sample is lower than that of T-rRBC sample, traducing a higher elongation. Indeed, T-rRBCs being less deformable than the healthy ones, they experience less deformation at the exit for an equivalent applied solicitation. Therefore, it seems that this parameter D_{out} can be used to distinguish mechanically impaired RBCs from healthy ones.

Figure 7.5 illustrates the evolution of τ as a function of the applied pressure for both samples, hRBC and T-rRBC. We can observe that for both samples, τ decreases when the applied pressure

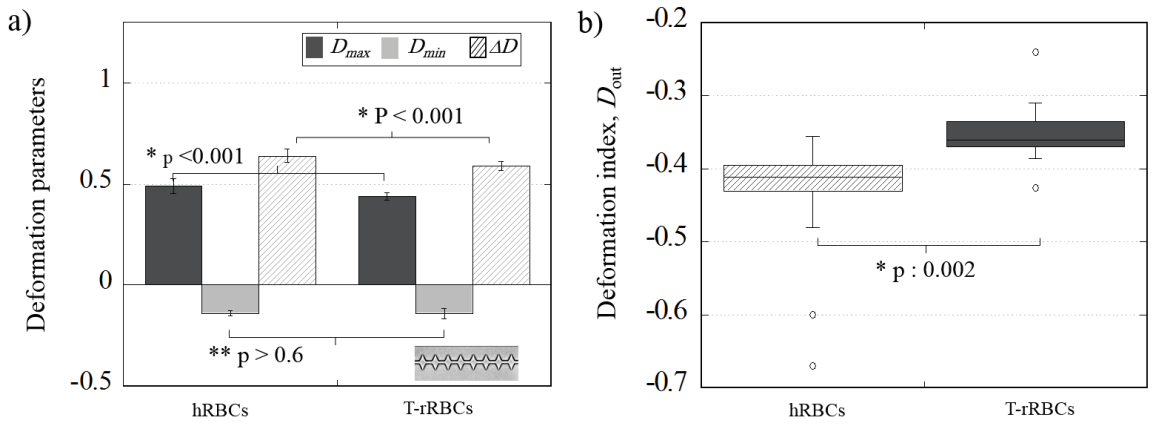

Figure 7.4: Comparison of (a) the deformation parameters D_{max}, D_{min} and ΔD and (b) the deformation index at the exit D_{out} between two RBC samples flowing in the OWC geometry: hRBCs and T-rRBCs. Error bars represent standard deviation calculated from roughly 15 cells. η_{out} = 31.5 mPa.s, W_o = 50 µm.

increases. Indeed by increasing the pressure, the velocity of the fluid, thus of the cell, increases. As presented in Chapter 5 for hRBCs, this parameter has a large impact on τ. We can see here that the same behavior is observed for T-rRBCs and that T-rRBCs relax faster than healthy cells, even though the difference is not always significant, the difference seems to be more pronounced at low pressure. This reduction of τ for T-rRBCs can arise from two phenomena: the decrease of D_{out} for this sample, or it can directly be a consequence of their modified mechanical properties.

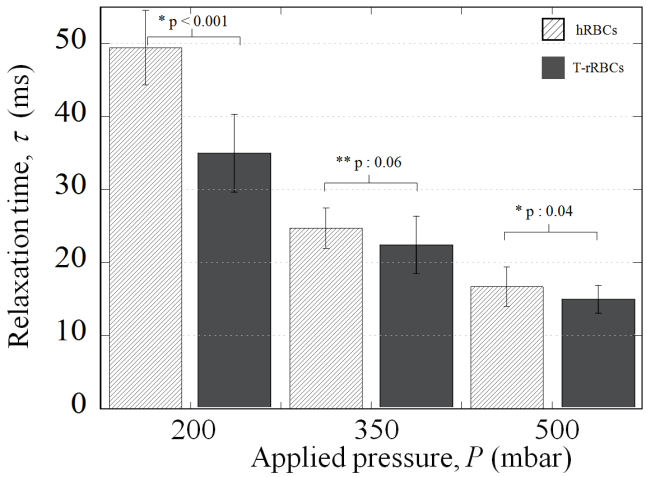

Figure 7.5: Relaxation time of hRBCs and T-rRBCs as a function of the applied pressure. Error bars represent standard deviation calculated from roughly 15 cells. η_{out} = 31.5 mPa.s and W_o = 50 µm.

We can conclude from the results presented above that ΔD, D_{out} and τ can be used to discriminate hRBCs and T-rRBCs with different mechanical properties.

7.2.1.2 Cell velocities

Along with the deformation parameters, cell velocities can also be considered as potential biomarkers for cell discrimination based on mechanical properties. The use of such parameter has been considered previously [91, 137, 138]. To overcome any velocity difference due to partial clogging of the channel or other technical issues, we decided to use the normalized velocity V_2/V_3. We remind the reader that V_3 presented less variability than V_1 due to the centering effect of the OWC geometry, it was therefore privileged to normalize the transit velocity V_2. Figure 7.6 presents the evolution of V_2/V_3 as a function of the applied pressure for both samples. We may notice that V_2/V_3 hardly varies with the applied pressure; it seems to be flow rate independent but rather related to the geometry design and dimensions.

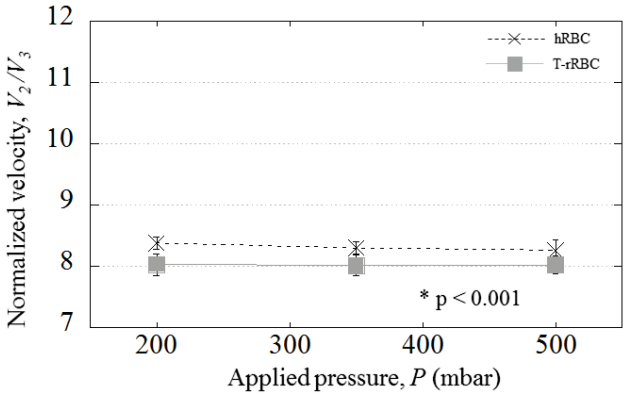

Figure 7.6: Representation of the normalized velocity V_2/V_3 as a function of the applied pressure in the OWC geometry, for hRBCs and T-rRBCs. η_{out} = 31.5 mPa.s.

We can also see from the results presented in Figure 7.6 that hRBCs flow statistically faster than T-rRBCs in the OWC geometry. This can be related to their respective deformations inside the OWC geometry, presented in Figure 7.4-a. Deformation results showed that both samples experience the same stretching in the enlargements D_{min}, but T-rRBCs being more rigid, they elongate less in the x-direction ($2a$ shorter and thus $2b$ larger for T-rRBCs than for hRBCs) when flowing inside the constrictions. Therefore, due to their larger section, they accumulate delay when entering each constriction.

We can conclude from these results that, although deformation parameters can be used as potential biomarkers to distinguish mechanically impaired RBCs from hRBCs, velocity parameters can also reflect this difference. As it is quite easy to implement in microfluidic devices time measurements, we can foresee that velocity parameters should be privileged. In the next section, we evaluated the impact of different OWC geometries (difference of shapes and dimensions of the enlargements and constrictions) to try to enhance the difference of velocity between two RBC populations presenting different mechanical properties. Thus, in the next section, we will only present the normalized cell velocities with their associated deformation (inside the median part).

7.2.2 Impact of the geometry parameters

Variations of the OWC geometry were tested to understand the impact of channel geometry on the flow of RBCs. First, we varied the parameters related to the length of the constrictions by testing a unique long constriction (ULC) as well as an OWC with longer constrictions (OWCLC), measuring 30 µm instead of 10 µm. In the second part, we studied the effect of the enlargement dimensions. To do so, we investigated OWC with longer enlargements (OWCLE), with 30 µm long enlargement instead of 10 µm, then OWC with wider enlargements (OWCWE) 50 µm instead of 25 µm and finally, an OWC with wider and longer enlargements (OWCWLE) 30 µm long and 50 µm high instead of 10 µm long and 25 µm wide. Microscopic images of the central zone of these channels are presented in Figure 7.7, full pictures of the geometries with all their dimensions are presented in Appendix B.

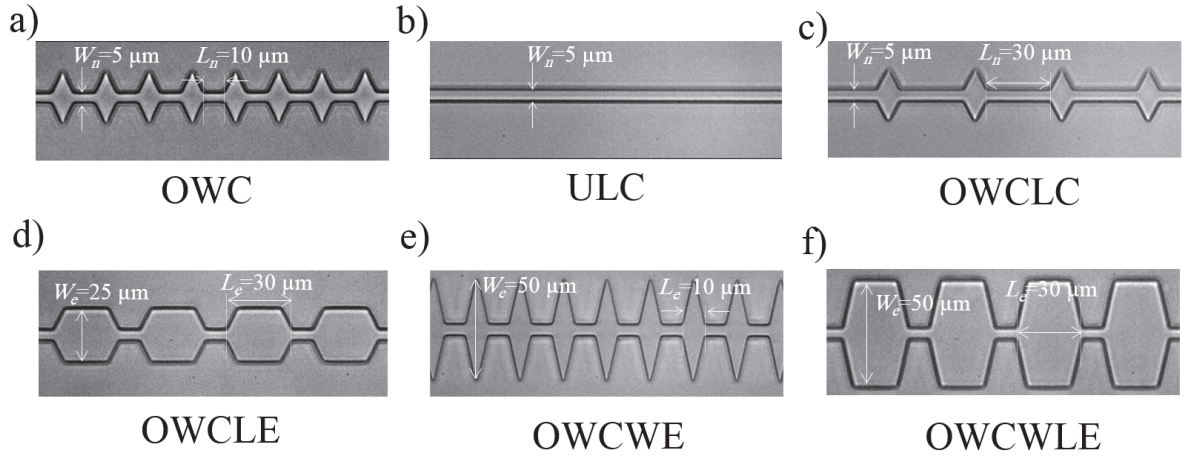

Figure 7.7: Microscopic images of the median part of microfluidic geometries tested for the discrimination of mechanically impaired RBCs. The height of all the channels was measured to be 5 µm.

The microfluidic flow inside the channels was simulated using 3-D Comsol Multiphysics® software, in order to estimate hydrodynamic resistances R_H for all the different geometries. R_H was estimated from the slope representing ΔP as a function Q, where ΔP is the difference of pressure between the inlet and outlet and Q the flow rate obtained from the simulation. The hydrodynamic resistance of each of the six geometries can be consulted in Appendix B. These results are consistent with the geometries, as the more confined the geometry is, the larger its resistance gets. The value of R_H impacts the dimensionless velocity, these calculated values will be used to explain the differences in V_2/V_3 between the different designs.

As already stated above, V_2/V_3 is flow rate independent but is directly linked to the channel geometry and its dimensions. Figure 7.8 represents V_2/V_3 as a function of the hydrodynamic resistance for the different geometries. We can note from the results that V_2/V_3 increases with R_H. For an equivalent ΔP between the different geometries, both V_2 and V_3 are modified due to the difference of hydodynamic resistance in the median part of the channel.

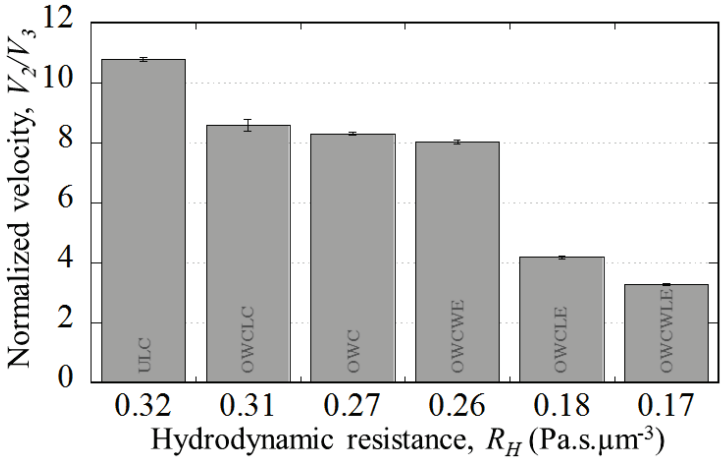

Figure 7.8: Evolution of the normalized velocity V_2/V_3 for hRBCs pooled over different pressure values as a function of channel hydrodynamic resistance R_H.

7.2.2.1 Variation of the constriction parameters

In this first section, we studied the effect of the length of the narrowing. We first tested the ULC geometry with no enlargements, and then we tested the OWCLC geometry. Results will be compared with those of the OWC geometry presented above.

Unique Long Constriction (ULC) geometry : The ULC channel consists in a unique constriction of the same length as the oscillating zone of the OWC (*i.e.* 290 µm). The width and depth of the constriction were kept at 5 µm. Figure 7.9 shows both the deformation index $\bar{D}$ defined as the stationary shape adopted by the cell inside the constriction (see Appendix B) and the normalized velocity V_2/V_3 for hRBCs and T-rRBCs. We can notice in Figure 7.9-a that both samples experience the same deformation inside the unique constriction which is mainly imposed by the channel geometry. In contrast with the OWC where the hRBCs experienced more deformation inside the constrictions, the extended length of the ULC forces both samples to adopt the channel dimensions and thus have the same deformation and "friction" during their passage. Regarding the velocities (Figure 7.9-b), V_2/V_3 does not show any significant difference between the two samples. If any delay is acquired by T-rRBCs at the entrance of a unique constriction, it is not enough to differentiate them with hRBCs.

Oscillating Width Channel with Longer Constrictions (OWCLC) geometry : In this section, we modified the length of the constrictions; instead of using constrictions of 10 µm, we extended their length to 30 µm. Results presented in Figure 7.10-a show that both hRBCs and T-rRBCs have the same deformation inside the constrictions D_{max}. Contrarily to the OWC, were the two samples showed different values for D_{max}, the length of the constrictions in the OWCLC was sufficient for the cells to adopt the same form in both samples. We can also notice that, cell stretching in the enlargements D_{min} is smaller for the T-rRBC than their healthy counterparts. Although the enlargements were kept

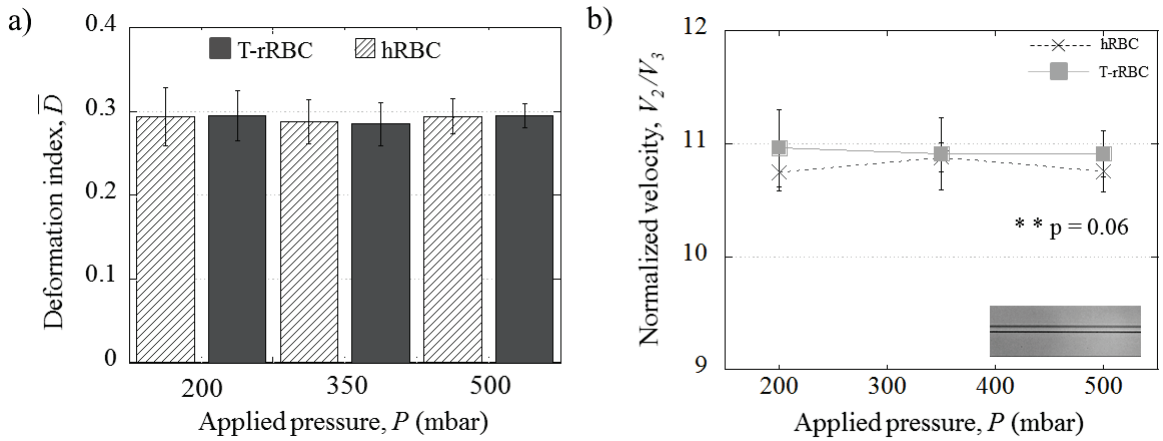

Figure 7.9: (a) Cell deformation index $\bar{D}$ and (b) normalized velocity V_2/V_3 versus the applied pressure P inside the ULC geometry for hRBCs and T-rRBCs. Error bars represent the standard deviation which is calculated from roughly 15 cells. η_{out} = 31.5 mPa.s.

at the same dimensions, this difference in D_{min} was not noticed in the OWC. We assume that the increased length of the constrictions causes T-RBCs to deform less in the widenings. Therefore, it would take less time for T-rRBCs to deform back in the x-direction in order to enter the constriction, leading to a globally faster transit through the OWCLC geometry (Figure 7.10-b).

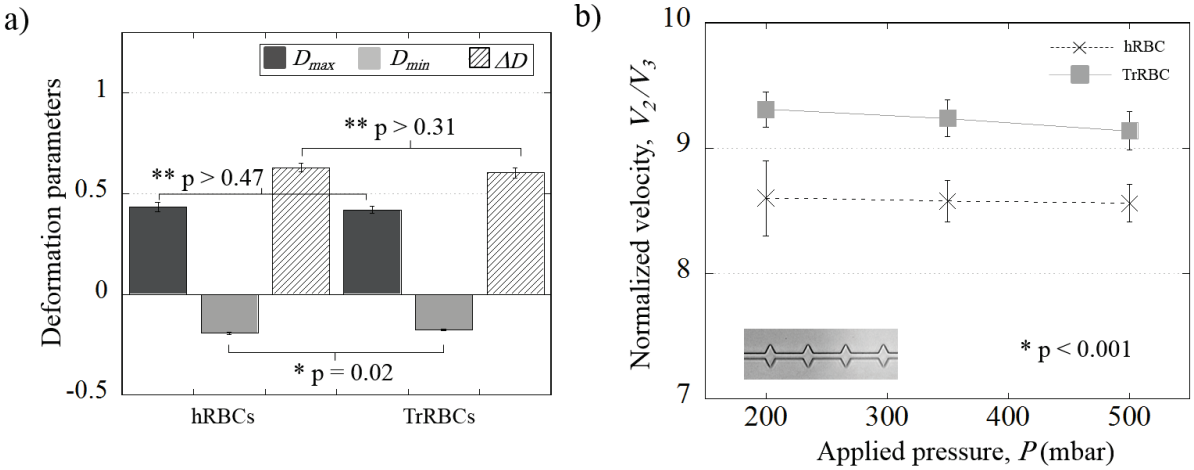

Figure 7.10: (a) Cell deformation indexes and (b) normalized velocity V_2/V_3 versus the applied pressure P inside the OWCLC geometry for hRBCs and T-rRBCs. Error bars represent the standard deviation which is calculated from roughly 15 cells. η_{out} = 31.5 mPa.s.

7.2.2.2 Variation of the enlargement parameters

In this section, we varied the enlargement dimensions. First, we investigated an OWC geometry with longer enlargements (OWCLE), with 30 µm long enlargements instead of 10 µm long ones, then an OWC with wider enlargements (OWCWE) implementing 50 µm wide widenings instead of having

enlargements 25 µm wide, and finally an OWC with both wider and longer enlargements (OWCWLE), with 50 µm wide and 30 µm long enlargements instead of 25 µm wide and 10 µm long ones.

Oscillating Width Channel with Longer Enlargements (OWCLE) geometry: For the OWCLE, 30 µm long enlargements instead of 10 µm long ones were used. We can note that T-rRBCs deform less than hRBCs both in the constrictions and in the enlargements. In contrast, from Figure 7.11-b we can observe that there is no statistically significant difference concerning the normalized velocity V_2/V_3 of the two samples. We explain this absence of speed difference between the two samples by the counterbalance of two separated effects. Indeed, T-rRBCs experiencing a smaller stretching in the constriction ($(D_{max})_{T-rRBCs} < (D_{max})_{hRBCs}$), they should travel through the geometry at lower speed. On the other hand, they also undergo a smaller stretching than hRBCs in the widenings. Thus, they would take less time to deform back in the x-direction to enter the next constriction, leading to a globally faster transit through the OWCLE geometry. We believe that the two different effects counterbalance each other, leading to an absence of significant difference in cell speed between the two RBCs samples. It is also worth noticing from the results in Figure 7.11-a that, for both RBC samples, the deformation parameters (in absolute value) are increased in this geometry compared to the values reached by these same parameter in the OWC geometry. For example, D_{min} is ranging from -0.4 to -0.5 according to the cell mechanical properties for OWCLE, whereas it was roughly reaching -0.17 for OWC. In the latter geometry, cells do not have the time to fully stretch in response to the widening, before being compressed again by the next narrowing. In the OWCLE, they have more time to deform in the y-direction, hence reaching higher amplitude of deformation.

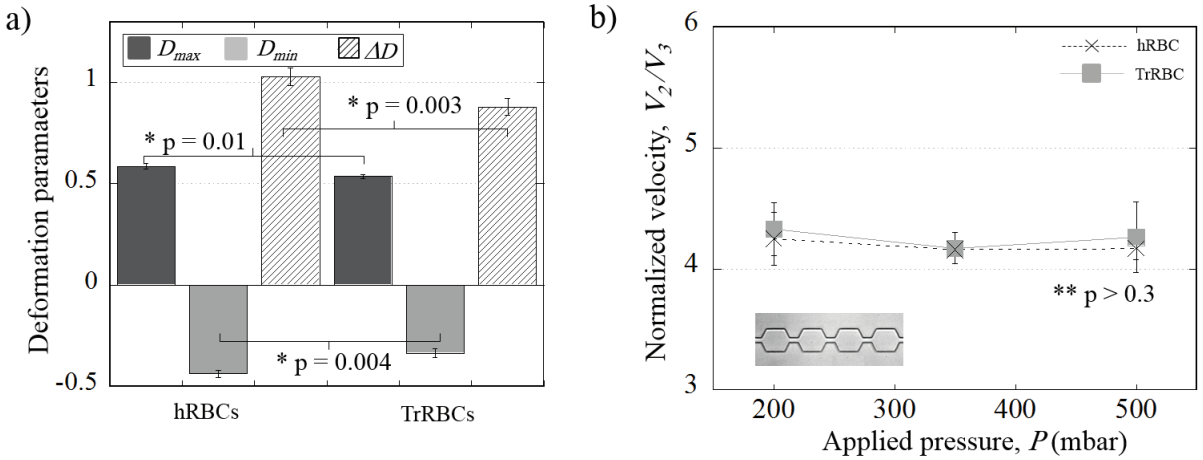

Figure 7.11: (a) Comparison of cell deformation indexes between hRBCs and T-rRBCs in the case of the OWCLE. (b)Evolution of the normalized velocity V_2/V_3 as a function of the applied pressure P. Error bars represent the standard deviation which is calculated from roughly 15 cells.

The Oscillating Width Channel with Wider Enlargements (OWCWE) geometry : For the OWCWE geometry, we extended the width of the enlargements to 50 µm compared to 25 µm in the case of

OWC geometry. We obtained results quite similar to those from the OWC geometry, $i.e\ D_{min}$ are equivalent for both samples, whereas, healthy cells are more stretched in the narrowings (D_{max} is higher) than their rigid counterparts (Figure 7.12-a), leading to a higher normalized velocity for hRBCs than for T-rRBCs (Figure 7.12-b). Therefore, increasing the width of the enlargements does not seem to have an impact on the behavior of RBCs. We believe that in the range of pressure applied during our experiments, the flow lines experienced by cells are similar for both the OWC and OWCLE.

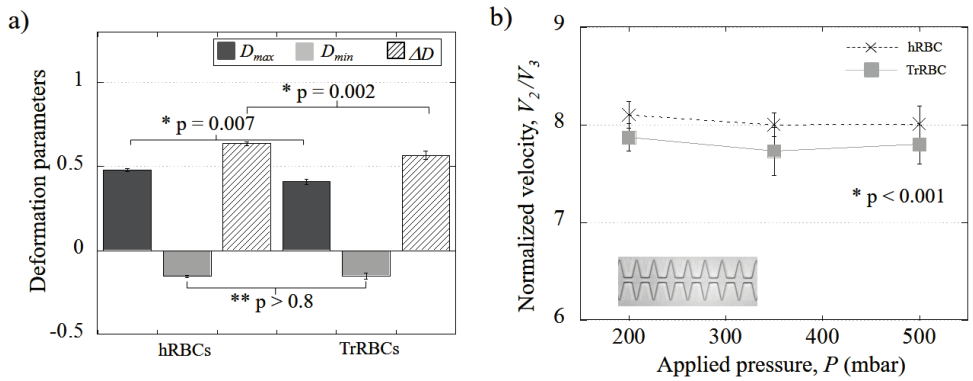

Figure 7.12: a) Cell deformation indexes and b) normalized velocity V_2/V_3 versus the applied pressure P inside the OWCWE geometry for hRBCs and T-rRBCs. Error bars represent the standard deviation which is calculated from roughly 15 cells. η_{out} = 31.5 mPa.s.

The Oscillating Width Channel with Wider and Longer Enlargements (OWCWLE) geometry : For the OWCWLE geometry, we implemented both higher and longer enlargements. Results are presented in Figure 7.13. We can observe that T-rRBCs both deform less (Figure 7.13-a) and flow faster (Figure 7.13-b). This difference in velocities is mainly due to the centering effect of this geometry. Indeed, we noticed that, when entering the geometry from a non-centered position, hRBCs tend to follow an oscillatory trajectory in the wider and longer enlargements compared to the T-rRBCs which follow a similar trajectory at first before getting centered earlier (Figure 7.14)-a. Indeed, when "oscillating" hRBCs follow streamlines close to the channel wall, hence increasing the length of the path followed, which is also associated with spending more time in regions of low velocities.

This phenomenon seems to be relatively close to that exploited in the Pinched Flow Fractionation technique (PFF) introduced by Yamada et al [139]. PFF uses the difference of size between particles pushed against the wall of a microchannel to separate them. Cells of different sizes will have their centers of mass positionned on different streamlines and thus will have different trajectories. In our case the difference of cell deformation between the hRBCs and the T-rRBCs will produce the same effect. Since T-rRBCs are less deformable, their center of mass will follow a streamline which is more centered as illustrated in Figure 7.14-b. In contrast, the more deformable hRBCs will have their center of mass closer to the channel wall and will therefore follow streamlines closer to the wall.

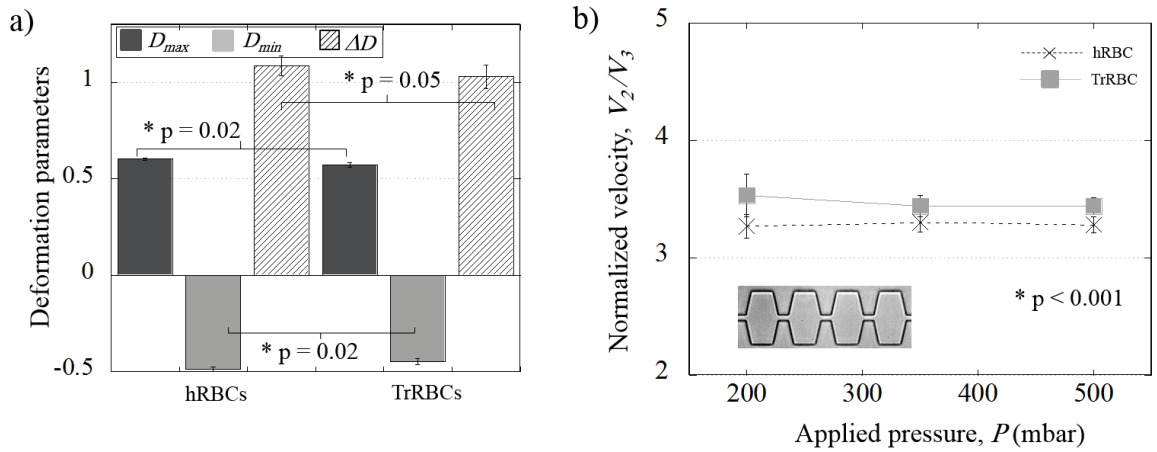

Figure 7.13: (a) Cell deformation indexes and (b) normalized velocity V_2/V_3 versus the applied pressure P inside the OWCWLE geometry for hRBCs and T-rRBCs. Error bars represent the standard deviation which is calculated from roughly 15 cells. η_{out} = 31.5 mPa.s.

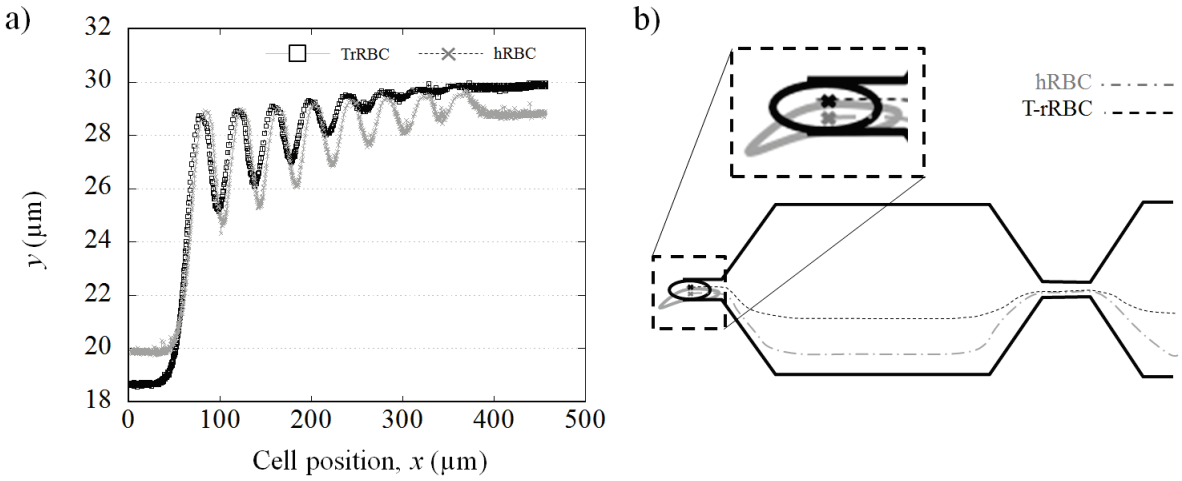

Figure 7.14: Evolution of the y-coordinate of the cell center of mass versus its x position for a hRBC (crosses) and a T-rRBC (open squares) in the OWCWLE microchannel. (b) schematic representation of the streamlines followed by hRBCs and T-rRBCs inside the OWCWLE.

7.2.2.3 Discussion on the most effective geometry

Experimental results issued from the six tested geometries showed different results concerning the normalized velocity V_2/V_3. Indeed, in some geometries such as ULC and OWCLE, no significant difference was obtained between the two samples. However, a difference of behavior was observed in the other geometries: hRBCs transited faster through the OWC and OWCWE, whereas, T-rRBC crossed faster in the OWCLC and OWCWLE.

Figure 7.15 shows the ratio of faster sample to slower one for the six configurations. We can notice from the results that the implementation of the widenings increased the efficiency of the geometries comparing to the ULC. We can also see from the results that ULC and OWCLE have the lowest ratio

among the six geometries as they produce the less difference in the flowing speed. OWC and OWCWE have almost the same ratio as the wider enlargements did not change the flowing dynamic of RBCs as already stated. The most efficient geometries seem to be the OWCLC and then OWCWLE: for the OWCLC, the increased length of the constrictions improved the geometry efficiency, a more thorough study on the constriction length may help optimizing further the OWCLC efficiency. For the OWCWLE, the ratio length/height of the enlargements seem to be the dominant parameter to consider in order to improve even further the OWCWLE. One may notice that the measured differences remain lower than 8% for all configurations. However, this differences still can be used to discriminate between the two samples as it can produce differences in flowing time. For instance, in the case of the OWCLC, the difference in flowing speed produces a difference of flowing time in the order of ~ 100 ms at 200 mbar, this difference can be increased if we decrease the flow speed.
Increasing the geometries length may amplify the measured differences, still, a compromise needs to be found between the channel length and the geometry efficiency. Indeed, an excessively long channel may induce the flow of several cells at the same time in the median part which may false measurements.

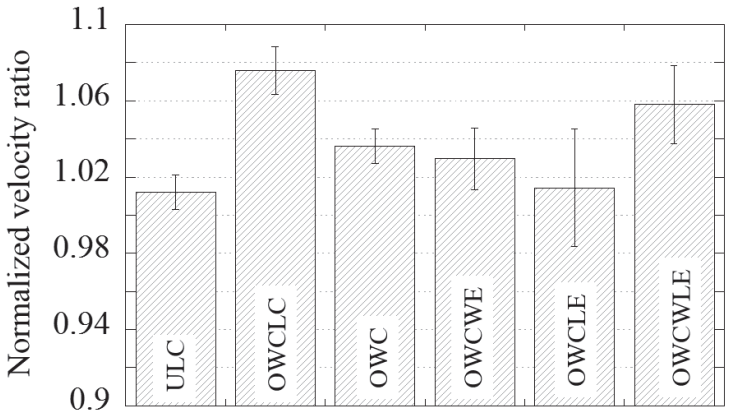

Figure 7.15: Ratio between the normalized velocity of the faster sample to the slower one for each tested geometry.

7.3 Discrimination of impaired RBCs using ED

Along with the passive microfluidic approach, we tried to evaluate the capacity of ED to differentiate mechanically impaired RBCs. Results from Chapter 6, showed us that the choice of experimental parameters is very important in order not to modify RBC mechanical properties. Therefore, we used these optimized parameters: η_{out} = 1.3 mPa.s, ΔV_1 = 48 V, t_{sol} = 100 ms, N = 1 and f = 1 MHz. We used these optimal parameters to characterize different samples of RBCs. First, we started by characterizing an "artificially" altered sample of RBCs. Next, we performed measurements on thermally rigidified samples (prepared as detailed in Chapter 4) versus hRBCs.

7.3.1 Effect of thermal treatment

We tested ED to measure deformation index and relaxation time of T-rRBCs, in order to evaluate the potential of this approach to discriminate healthy and mechanically impaired RBCs. First, we noticed that thermal rigidification seems not to affect cell response to electrical field gradient. Indeed, we were able to attract T-rRBCs toward electrodes using the same voltage values as for hRBCs (ΔV_1 = 2 V) at the same frequency 1 MHz. We noticed that, when applying the same solicitation conditions as for hRBCs (*i.e.* ΔV_1 = 48 V, η_{out} = 1.3 mPa.s, t_{sol} = 100 ms, N = 1 and f = 1 MHz), T-rRBCs showed significantly less deformation than their healthy counterparts ($D_1 \sim -0.52$ for T-rRBCs and $D_1 \sim -0.62$ for hRBCs) as shown in Figure 7.16-a. This difference in deformation index D_1 at the same applied voltage can be used as a first discrimination parameter between the two samples. When we look at the relaxation times, the difference in initial deformation D_1 will necessarily produce a difference in τ values. As presented in Figure 7.16-b, the measured relaxation times of T-rRBCs are smaller than those of hRBCs (~ 40 ms for T-rRBCs and ~ 90 ms for their healthy counterparts). This variation is significant if we do not take into account the difference in initial deformation between the two samples. However, for this experiment it is difficult to discriminate the impact of the alteration of the mechanical of T-rRBCs on D1 and tau. Indeed, it is highly expected that such treatment would also impact dielectric properties of the cells and thus dielectrophoretic force applied on the cells.

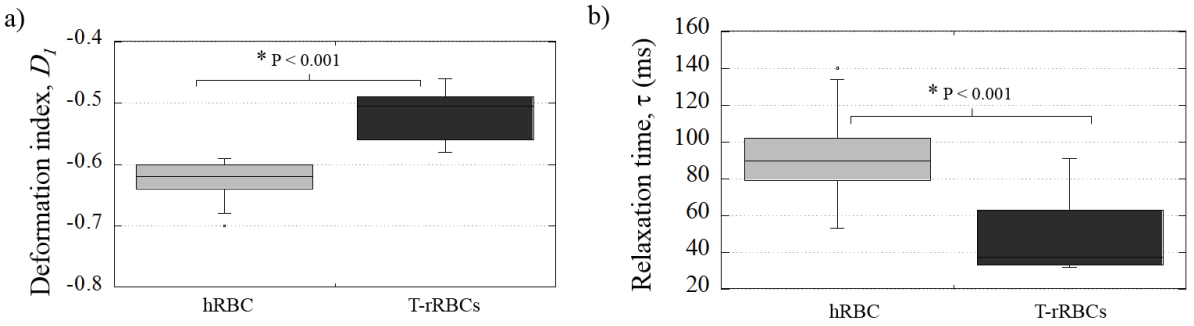

Figure 7.16: Impact of thermal rigidification on the deformation and relaxation of RBCs at ΔV_1 = 48 V. Each boxplot represents roughly 12 cells.

The value of the deformation index D_1 for T-rRBCs at ΔV_1 = 48 V ($D_1 \sim$ -0.52) is equivalent to the value D_1 of hRBCs at ΔV_1 = 24 V. Thus, in order to be able to compare the two samples relaxation times, we used the data for T-rRBCs at ΔV_1 = 24 V to have the same initial elongation D_1 for both samples (hRBCs and T-rRBCs).

Results presented in Fig 7.17 show that, for equivalent initial deformation ($D_1 \sim$ -0.52), T-rRBCs seem to relax faster than the ones in the control sample. Although T-test measurements reveal that this difference is not significant.

As already presented in Figure 7.16, T-rRBCs can be discriminated from hRBCs using ED if we compare the two samples at the same applied voltage. Indeed, when comparing at the same voltage value ΔV_1 = 48 V, both cell deformation D_1 and relaxation time τ can be used to discriminate the two

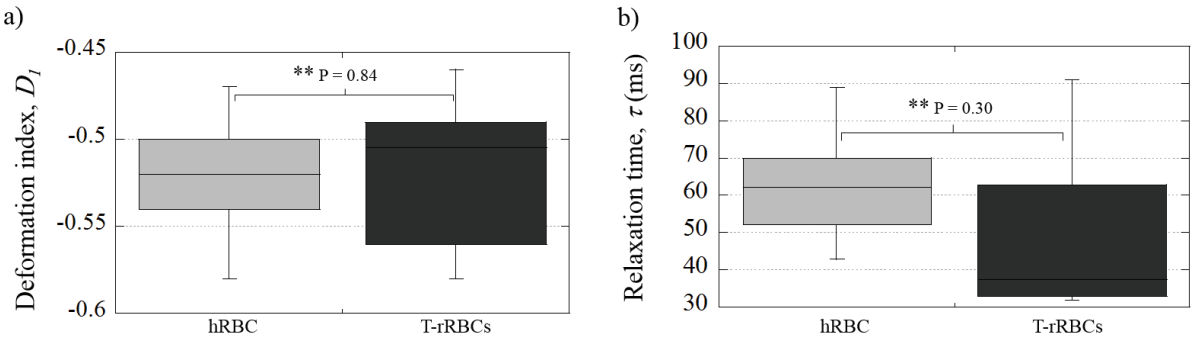

Figure 7.17: Comparison of hRBCs and T-rRBCs relaxation at equivalent initial deformation (D_1 ~ -0.52). Each boxplot represents roughly 12 cells.

samples. One important point that needs to be highlighted in further works is to determine if the measured difference in ED can be attributed to both differences in cell mechanical properties as well as their dielectric properties. One way to dissociate the two effects is to perform a characterization of cells dielectric properties using electro-rotation.

7.3.2 Characterization of a RBC sample submitted to an "artificial" fatigue

We demonstrated in Chapter 6 that by cycling RBCs using specific ED parameters, RBC mechanical properties were modified. We used this condition in order to "artificially" fatigue our hRBC sample and tried to estimate this fatigue - which can also be assimilated to a variation of mechanical properties of cells - using ED. Fig. 7.18 shows the results obtained during this experiment in terms of deformation and relaxation time. First, we measured D_1 and τ for the hRBC sample using the optimized parameters. Then, we cyclically submitted this sample to ED (η_{out} =1.3 mPa.s, ΔV_1 = 48 V, t_{sol} =5000 ms, t_{rest} = 1000 ms, N = 20 and f = 1 MHz) and finally repeated the measurements using the previously optimized parameters. As expected, we measured an evolution of both parameters: deformation index D_1 (Fig. 7.18-a) and relaxation time τ (Fig. 7.18-b) before and after the cyclic solicitation. After cyclic solicitation, RBCs deform less and take longer time to relax. As explained previously in Chapter 6, deformation index has an impact on τ. We showed that when D_1 decreases, τ decreases as well. Here, after a cyclic solicitation, D_1 decreased. If no fatigue was induced, we would expect a shorter relaxation time. However, in this case we measured a longer τ demonstrating that the cyclic solicitation probably induced an artificial fatigue to our hRBC sample. Such differences in mechanical properties can be detected using ED. If we compare the samples at same initial deformation, the difference will be more marked as τ is decreases for lower initial deformations (τ ~ 60 ms for D_1 ~ 0.52 and τ ~ 100 ms for D_1 ~ 0.62)

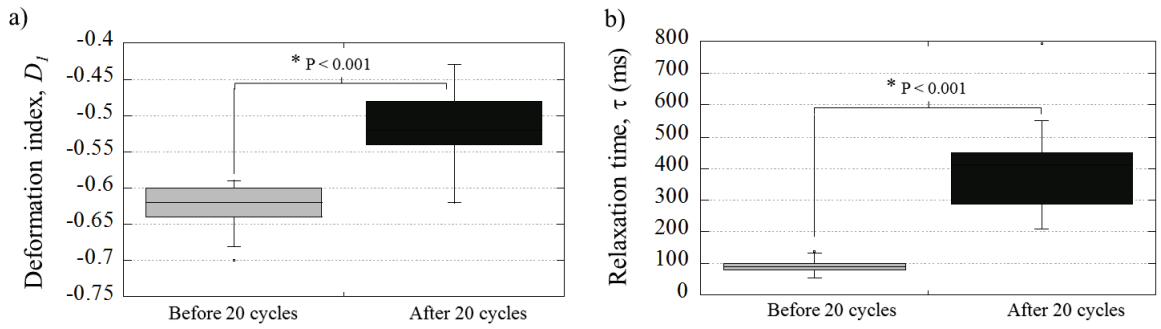

Figure 7.18: a) Deformation index D_1 and b) relaxation time τ of hRBCs before and after a cyclic solicitation. Solicitation parameters: η_{out} = 1.3 mPa.s, ΔV_1 = 48 V, t_{sol} = 5000 ms, t_{rest} = 1000 ms, N = 20 and f = 1 MHz. Measurement parameters: η_{out} = 1.3 mPa.s, ΔV_1 = 48 V, t_{sol} = 100 ms, N = 1 and f = 1 MHz.

7.4 Conclusion

Throughout this chapter, we presented experimental results concerning the discrimination of mechanically impaired RBCs using two different approaches. First, we started by presenting a passive approach using microfluidic channels. We showed that both deformation parameters and cell velocity constitute potential biomarkers for cells mechanical properties. We privileged the use of cell velocity for our study, as the measurement of transit times through the geometry seems more suitable for Point-Of-Care (POC) applications. The impact of the channel geometry on the flow of hRBCs and T-rRBCs was investigated and discussed.
In a second time, we used an active approach based on DEP force to perform the same analysis. An optimized set of parameters was used to deform healthy, "artificially" altered and rigidified samples. Although ED was proved to be efficient to discriminate between the samples, the measured difference can not be attributed solely to cells mechanical properties.

Both approaches can be suitable to achieve the discrimination between the two samples and each of them has its own advantages and drawbacks. The integration and automatisation of time measurements for passive microfluidics seem to be easier than the integration and automatisation of ED requiring semi-manual image analysis. In contrast, ED allows the analysis of a large population of cells simultaneously, whereas in passive microfluidics, single cells have to be studied one after the other, imposing high flow velocity in order to match the high throughput associated with POC diagnostic.

CHAPTER 8

CONCLUSION

Throughout this thesis, we aimed at evaluating the capacity of a passive microfluidic configuration and an electrodeformation assay to discriminate RBCs based on their mechanical properties. We first presented a study of the behavior of healthy RBCs flowing passively in a microfluidic channel with oscillating width. We documented the existence of two relaxation modes for the cell depending on the external flow parameters. The two behaviors observed experimentally were also retrieved using 2-D numerical simulations performed on Comsol Multiphysics®. Moreover, we presented a theoretical estimation of the local hydrodynamic stress that RBCs experience at the exit of the last geometrical constriction in conditions corresponding to the frontier between the two modes. This estimated transition stress was used to evaluate the Capillary numbers corresponding to each mechanical property of the RBC (stretching, bending and shear moduli). Obtained results showed that neither the stretching nor the bending moduli controlled the transition between the two relaxation modes. In contrast, we retrieved a Capillary number of shear around 1 in experimental conditions corresponding to the transition between both relaxation behaviors. Which means that the RBC shear modulus is the responsible mechanical property of the transition. We stress that this technique can be used to characterize cells mechanical properties based on their relaxation mode in a microfluidic flow. Finally, we investigated the dependency of cell deformation and relaxation upon the experimental conditions such as the cell velocity, the main channel width, as well as the external medium viscosity. Indeed, we reported that both cell deformation and relaxation were influenced by the variation of experimental conditions. Based on previous statements from the literature, we proposed an explanation to the obtained results in term of hydrodynamic stress and energy dissipation in the buffer.

Using a second approach based on electrodeformation, we highlighted the dependency of RBCs mechanical response upon the experimental conditions used during ED assays. We performed a

thorough investigation of the influence of experimental parameters in ED by testing several parameters related to the electrical solicitation of cells. We showed that in order not to affect the mechanical properties of cells by the application of an electrical field, it is necessary to carry out such assays in particular experimental conditions. Besides, we also showed that the relaxation time seems to be a more sensitive parameter to monitor RBCs mechanical properties, than its deformation mainly imposed by the measurement technique. The relaxation time measured with ED presents a great potential as a biomarker to assess modification of RBCs deformability among a given sample.

In the last chapter, we presented experimental results concerning the discrimination of mechanically impaired RBCs using both studied approaches. First, we showed that both deformation parameters and cell velocity constitute potential biomarkers for cells mechanical properties in passive microflow. We privileged the use of cell velocity for our study, as the measurement of transit times through the geometry seems to be more suitable for Point-Of-Care (POC) applications. The impact of the channel geometry on the flow of hRBCs and T-rRBCs was investigated and discussed. Using the active approach, we also showed that DEP force can be used to perform the discrimination of T-rRBCs, , although we have not concluded yet on the fact that we detect difference in cell mechanical or dielectric properties. Both approaches can be suitable to achieve the discrimination between the two samples and each of them has its own advantages and drawbacks. The integration and automatisation of time measurements for passive microfluidics seem to be easier than the integration and automatisation of ED requiring semi-automated image analysis. In contrast, ED allows the analysis of a large population of cells simultaneously, whereas in passive microfluidics, single cells have to be studied one after the other, imposing high flow velocity in order to match the high throughput associated with POC diagnostic.

The open perspectives from this study are interesting, as it constitutes a baseline for the developpment of microfluidic systems for the characterization and discrimination of cell mechanical properties. For passive approach, more thorough studies need to be carried out to optimize further the geometries and increase their efficiency before testing them on pathological samples. The same designs can be also adapted to work on other cell types than RBCs. For ED, further experiments have to be carried out using pathological samples to test the feasibility of the approaches notably by testing the sensitivity of pathological samples to DEP force.

APPENDIX A

APPENDIX A

A.1 Impact of the number of constrictions on the relaxation time τ

Numerical simulations have been performed to compare with our experimental findings regarding the two relaxation modes. A simplified version of the geometry was chosen for the computation, as the model was built with a single 5 µm wide and 10 µm long constriction introduced in a 15 µm wide channel. In order to compare the numerical results with our experimental data, we have verified experimentaly that the historic of deformation, *i.e.* number of narrowings in series did not impact the cell relaxation at the exit. To do so, we performed an experimental study using two configurations: (i) the OWC geometry, implementing 14 constrictions and (ii) a simplified geometry with only 1 short constriction. We studied the RBCs flow in both geometries while using the same external buffer viscosity η_{out} = 31.5 mPa.s and keeping the same channel width W_o = 15 µm and channel height h = 5 µm.. The results presented in Figure A.1-a represent the evolution of the deformation index of hRBCs as a function of time, for two different geometries: a OWC channel, composed of 14 constrictions, and a single 10 µm long constriction. The two cells which flows roughly at the same speed V_{cell} = 500 µm.s^{-1}, have been selected because they add approximately the same volume, estimated through an equivalence of the projected area. We can see from the graph that curves collapse pretty well, indicating that the two cells exhibit the same behavior at the exit of the constriction. Figure A.1-b represents the relaxation time τ as a function of the cell speed V_{cell} for the OWC geometry and a single short constriction. τ does not seem to be influenced by the change in the constriction number, as the τ values obtained for the two different configurations collapse on the same line. We concluded from this experiment that the use of a simplified design of the geometry does not impact the relaxation time values, hence allowing the comparison between numerical and experimental results. However, we noticed that the 14 constrictions geometry was more suitable for our experimental study as it had a more efficient centering effect than that with a single constriction

which justifies its use for the rest of the experiments.

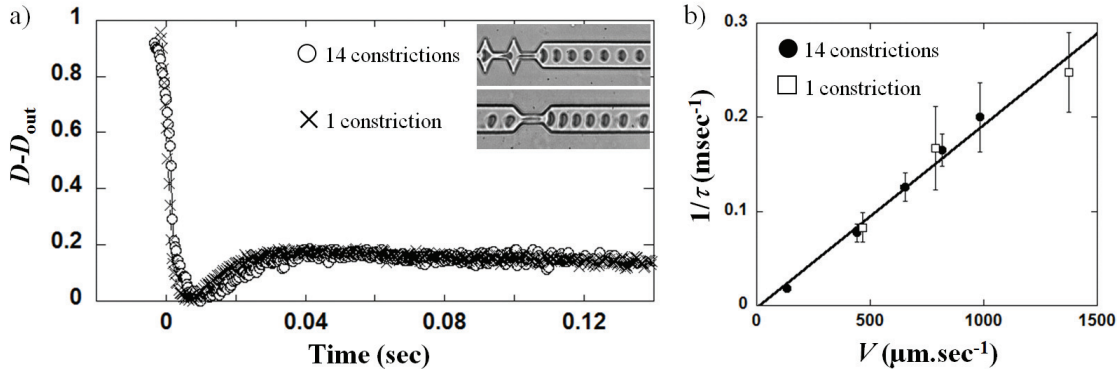

Figure A.1: (a) Evolution of D-D_{out} versus time for two cells of apporximately the same volume, flowing respoectively in a OWC channel and a single short constriction geometry. Hydrodynamic conditions were V_{cell} = 500 µm.s^{-1} and η_{out} = 31.5 mPa.s. (b) Relaxation time of hRBCs flowing out of a channel with 14 constrictions in comparison with a channel with a single short constriction as a function of the cell speed V_{cell}, at η_{out} = 31.5 mPa.s. The results using the two different configurations fit well which validate the comparision between experiment and numerical simulations.

APPENDIX B

APPENDIX B

B.1 Geometries evaluated for the discrimination of mechanically impaired RBCs using passive microfluidics

We present in this appendix the dimensions and hydrodynamic resistances R_H of the different variations of the Oscillating Width channel geometry OWC presented in Figure **??**. Six different geometries were evaluated to discriminate mechanically impaired RBCs and are presented below.

Oscillating width channel **OWC**

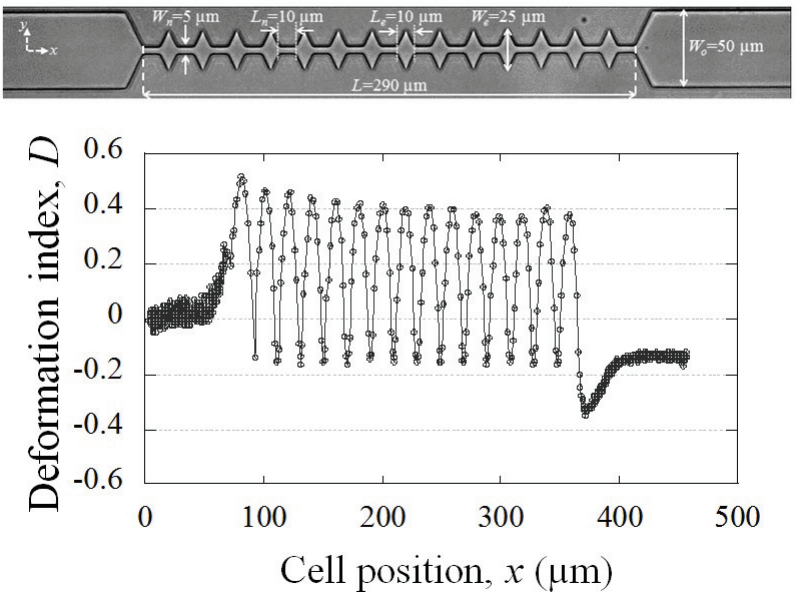

B.1.1 Variation of the constriction parameters

Unique Long Constriction **ULC** and Oscillating Width Channel with Longer Constrictions **OWCLC**

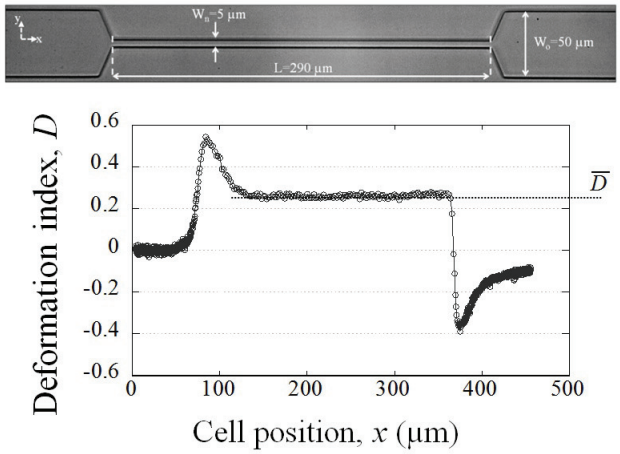

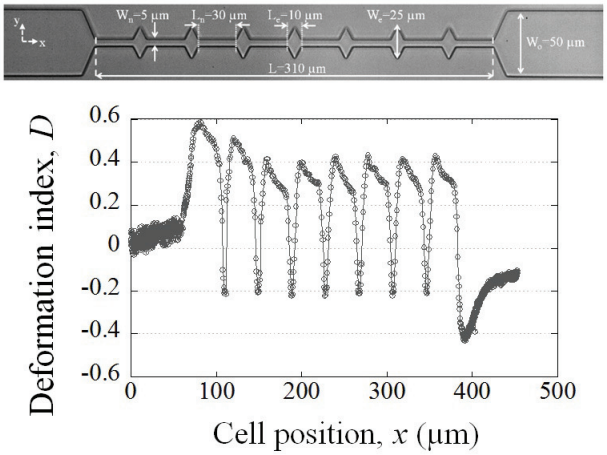

B.1.2 Variation of the enlargement parameters

Oscillating Width Channel with Wider Enlargements **OWCWE**
and Oscillating Width Channel with longer Enlargements **OWCLE**

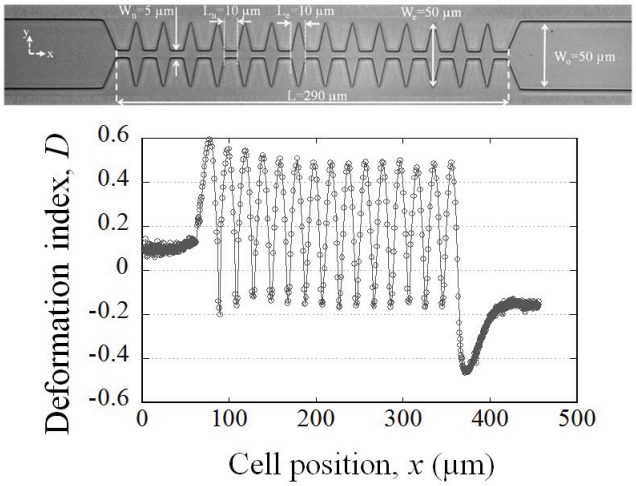

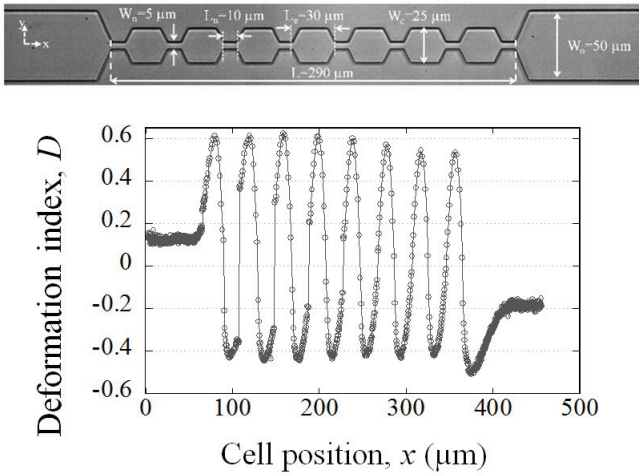

Oscillating Width Channel with Wider and Longer Enlargements OWCWLE

B.2 Presentation of the hydrodynamic resistances R_H

Hydrodynamic resistances of the tested geometries were calculated using Comsol Multiphysics simulations and are presented below.

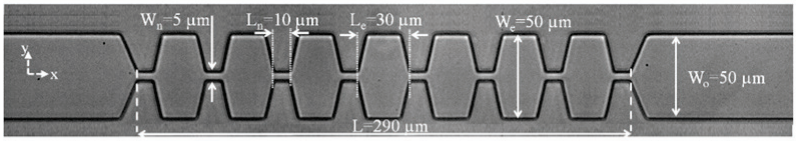
W_n=5 µm
L_n=10 µm
L_e=30 µm
W_e=50 µm
W_o=50 µm
L=290 µm
y
x

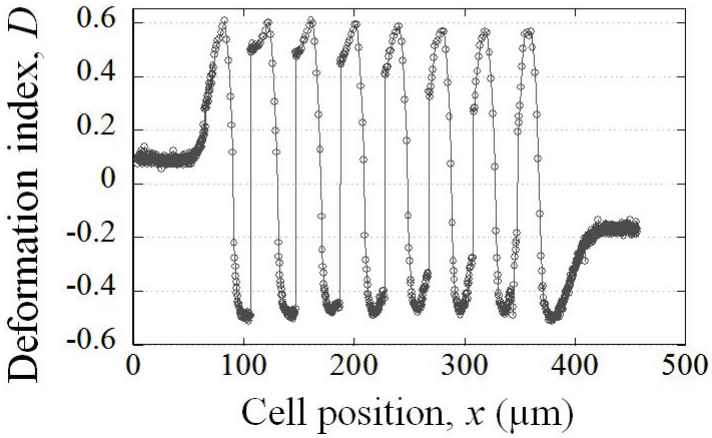
Deformation index, D
0.6
0.4
0.2
0
-0.2
-0.4
-0.6
0
100
200
300
400
500
Cell position, x (µm)

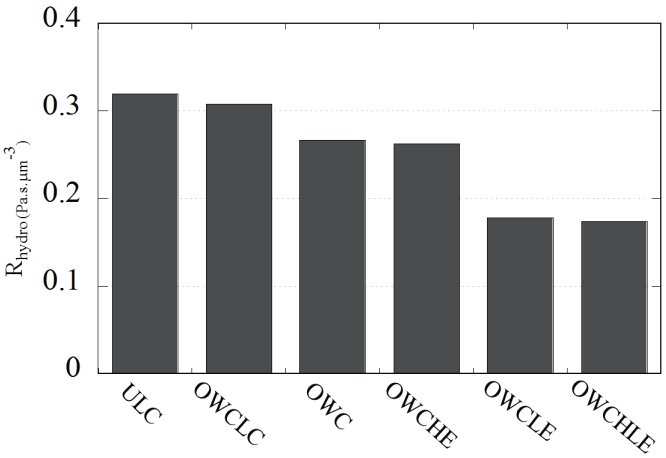
R_hydro (Pa.s.µm^-3)
0.4
0.3
0.2
0.1
0
ULC
OWCLC
OWC
OWCHE
OWCLE
OWCHLE

BIBLIOGRAPHY

[1] Yi Ma Lijia Cai Xing Yin Yuan Wang Kehui Guo Jigang Zhang Yujing Chen Jiangning Guo Xing Li Qibin Li Xiaoying Wang Wenjing Zhang Yan Wang Jin Jiang Xueyuan Xiang Yang Xu Chen Zheng Pingping Zhang Juanbin Li Ruiqiang Zhang Hongjie Shang Xiaobin Gong Ting Ning Guang Wang Jun Zen Ke Zhang Junfeng Zhang Chen-Yu Chen, Xi Ba. Characterization of microRNAs in serum: a novel class of biomarkers for diagnosis of cancer and other diseases. *Cell Research*, 18(10), 2008.

[2] P Megraud F Axon a T Deltenre M Hirschl a M Gasbarrini G O'Morain C Garcia J M Quina M Tytgat G N Vaira, D Malfertheiner. Diagnosis of Helicobacter pylori infection with a new non-invasive antigen-based assay. HpSA European study group. *Lancet*, 354(9172), 1999.

[3] Lacombe Francis Mahon Francois Xavier Vergnolle Ines, Allou Kaoutar and Vial Jean-Philippe. Verification of a quantitative method: complete blood count by flow cytometry, the HematoFlow (TM) system (Beckman Coulter). *ANNALES DE BIOLOGIE CLINIQUE*, 74:617–631, 2016.

[4] M. Nishino, H. Tanaka, H. Oqura, Y. Inoue, T. Koh, K. Fujita, and H. Sugimoto. Serial changes in leukocyte deformability and whole blood rheology in patients with sepsis or trauma. *J Trauma*, 59(6):1425–1431, 2005.

[5] A. D. van der Meer, A. A. Poot, J. Feijen, and I. Vermes. Analyzing shear stress-induced alignment of actin filaments in endothelial cells with a microfluidic assay. *Biomicrofluidics*, 4, 2010.

[6] S. Suresh, J. Spatz, J. P. Mills, A. Micoulet, M. Dao, C. T. Lim, M. Beil, and T. Seufferlein. *Connectiones between single-cell biomechanics and human disease states: gastrointestinal cancer and malaria.* Acta Biomaterialia, 2005.

[7] R. D. González-Cruz, V. C. Fonseca, and E. M. Darling. Cellular mechanical properties reflect the differentiation potential of adipose-derived mesenchymal stem cells. *Proc Natl Acad Sci USA*, 109, 2012.

[8] G. A. Barabino, M. O. Platt, and D. K. Kaul. Sickle cell biomechanics. *Annu Rev Biomed Eng*, 12:345–367, 2010.

[9] J. P. Mills, M. Diez-Silva, D. J. Quinn, M. Dao, M. J. Lang, Tan Ksw, C. T. Lim, G. Milon, P. H. David, O. Mercereau-Puijalon, S. Bonnefoy, and S. Suresh. Effect of plasmodial resa protein on deformability of human red blood cells harboring plasmodium falciparum. *Proc Natl Acad Sci USA*, 104(22):9213–9217, 2007.

[10] Giovanna Tomaiuolo. Biomechanical properties of red blood cells in health and disease towards microfluidics. *Biomicrofluidics*, 8:051501, 2014.

[11] M. Kaibara. Rheology of blood coagulation. *Biorheology*, 33(4):101–117, 1996.

[12] Gamaleldin I. Harisa. Blood viscosity as a sensitive indicator for paclitaxel induced oxidative stress in human whole blood. *Saudi Pharmaceutical Journal*, 23(1):48–54, 2015.

[13] Ikonet. http://www.ikonet.com/fr/ledictionnairevisuel/etre-humain/anatomie/circulation-sanguine/composition-du-sang.php.

[14] Université de médecine Angers. http://lewebpedagogique.com/arnaud/2009/05/14/b2-les-defenses-de-lorganisme-2/. *le web pédagogique*.

[15] E A Evans and Y C Fung. Improved measurements of the erythrocyte geometry. *Microvascular research*, 4:335–347, 1972.

[16] P Aguilar-Matinez. Érythrocytes. pages 1–6, 2007.

[17] Chantal Kohler. Les cellules sanguines. 2011.

[18] N Mohandas, , and E A Evans. Mechanical properties of the red cell membrane in relation to molecular structure and genetic defects. *Annual Review of Biophysics and Biomolecular Structure*, 23(1):787–818, 1994. PMID: 7919799.

[19] Camille Duprat and Howard Stone, editors. *Fluid-Structure Interactions in Low-Reynolds-Number Flows*. Soft Matter Series. The Royal Society of Chemistry, 2016.

[20] Y Kim and Kyoohyun Kim. Measurement techniques for red blood cell deformability: recent advances. *Blood Cell-An Overview*, (1), 2012.

[21] P Bassereau, J Ohayon, F Gallet, R Perzynski, and F Amblard. Thèse de Doctorat de l ,Äô Université Paris VI Physique des Liquides Guillaume Lenormand Élasticité du squelette du globule rouge humain - une étude par pinces optiques -. 2001.

[22] Samuel E. Lux. Anatomy of the red cell membrane skeleton: unanswered questions. *Blood*, 127(2):187–199, 2016.

[23] TPE globule Rouge. https://tpeglobulerouge.wordpress.com/reveilleau/losmose-dans-notre-cas-les-globules-rouges/.

[24] Frans A. Kuypers. Hemoglobin S polymerization and red cell membrane changes. *Hematology/Oncology Clinics of North America*, 28(2):155–179, 2014.

[25] R M Hochmuth and R E Waugh. Erythrocyte membrane elasticity and viscosity. *Annual review of physiology*, 49:209–219, 1987.

[26] W Rawicz, K C Olbrich, T McIntosh, D Needham, and E A Evans. Effect of chain length and unsaturation on elasticity of lipid bilayers. *Biophysical journal*, 79(1):328–339, 2000.

[27] R M Hochmuth, P R Worthy, and E A Evans. Red cell extensional recovery and the determination of membrane viscosity. *Biophysical journal*, 26(1):101–114, 1979.

[28] R Waugh and E A Evans. Thermoelasticity of red blood cell membrane. *Biophysical journal*, 26(1):115–131, 1979.

[29] E A Evans. New membrane concept applied to the analysis of fluid shear- and micropipette-deformed red blood cells. *Biophysical journal*, 13:941–954, 1973.

[30] S Hénon, G Lenormand, a Richert, and F Gallet. A new determination of the shear modulus of the human erythrocyte membrane using optical tweezers. *Biophysical journal*, 76(February):1145–1151, 1999.

[31] G Crandall and A. Critz. Influence of pH on elastic deformability of the human erythrocyte membrane. *American Journal of Physiology-Cell Physiology*, 1978.

[32] G B Nash and H J Meiselman. Alteration of red cell membrane viscoelasticity by heat treatment: effect on cell deformability and suspension viscosity. *Biorheology*, 22(1):73, 1985.

[33] E A. Evans, N. Mohandas, and a. Leung. Static and dynamic rigidities of normal and sickle erythrocytes. Major influence of cell hemoglobin concentration. *Journal of Clinical Investigation*, 73:477–488, 1984.

[34] E A Evans. Bending elastic modulus of red blood cell membrane derived from buckling instability in micropipet aspiration tests. *Biophysical journal*, 43(July):27–30, 1983.

[35] E A Evans and R M Hochmuth. Membrane viscoelasticity. *Biophysical journal*, 16(1):1–11, 1976.

[36] A Farutin, C Misbah, and L Bureau. Viscoelastic transient of confined Red Blood Cells. pages 1–11.

[37] Timo Betz, Martin Lenz, Jean-François Joanny, and Cécile Sykes. ATP-dependent mechanics of red blood cells. *Proceedings of the National Academy of Sciences of the United States of America*, 106:15320–15325, 2009.

[38] Minh Quan and Thai Mod. Modélisation microm écanique et simulation numérique du fluage des bétons avec prise en compte de l'endommagement et des effets thermo-hydriques. *PhD Thesis*, 2012.

[39] L Dintenfass. Internal Viscosity of the Red Cell and a Blood Viscosity Equation. *Nature*, 219:956–958, 1969.

[40] H Schmid, J.V Gosen, L Heinich, H.V Klose, and E Volger. A counter-rotating ‚Äúrheoscope chamber‚Äù for the study of the microrheology of blood cell aggregation by microscopic observation and microphotometry. *Microvascular Research*, 6(3):366–376, 1973.

[41] N Mohandas, M R Clark, M S Jacobs, and S B Shohet. Analysis of factors regulating erythrocyte deformability. *The Journal of clinical investigation*, 66(3):563–573, 1980.

[42] Kristen E. Bremmell, Allan Evans, and Clive a. Prestidge. Deformation and nano-rheology of red blood cells: An AFM investigation. *Colloids and Surfaces B: Biointerfaces*, 50(1):43–48, June 2006.

[43] Subra Suresh. Biomechanics and biophysics of cancer cells. *Acta Materialia*, 55:3989–4014, 2007.

[44] J Patrick Shelby, John White, Karthikeyan Ganesan, Pradipsinh K Rathod, and Daniel T Chiu. A microfluidic model for single-cell capillary obstruction by Plasmodium falciparum-infected erythrocytes. *Proceedings of the National Academy of Sciences of the United States of America*, 100(25):14618–14622, 2003.

[45] H Schmid-Schönbein, J von Gosen, L Heinich, H J Klose, and E Volger. A counter-rotating "rheoscope chamber" for the study of the microrheology of blood cell aggregation by microscopic observation and microphotometry. *Microvascular research*, 6(3):366–376, 1973.

[46] S.P. Sutera, V. Seshadri, P.a. Croce, and R.M. Hochmuth. Capillary blood flow: II. Deformable model cells in tube flow. *Microvascular Research*, 2(4):420–433, 1970.

[47] G. M. Artmann. Microscopic photometric quantification of stiffness and relaxation time of red blood cells in a flow chamber. *Biorheology*, 32(5):553–570, 1995.

[48] M Bessis and Mohandas. Automated ektacytometry: a new method of measuring red cell deformability and red cell indices. *Blood cells*, 6:315–327, 1980.

[49] O. K. Baskurt and H. J. Meiselman. Determination of red blood cell shape recovery time constant in a Couette system by the analysis of light reflectance and ektacytometry. *Biorheology*, 33(6):489–503, 1997.

[50] Evans E A and Paul L La Celle. Intrinsic Material Properties of the Erythrocyte Membrane Indicatedby Mechanical Analysis of Deformation. *Blood*, 45(1), 1975.

[51] Fiona K. Glenister, Ross L. Coppel, Alan F. Cowman, Narla Mohandas, and Brian M. Cooke. Contribution of parasite proteins to altered mechanical properties of malaria-infected red blood cells. *Blood*, 99(3):1060–1063, February 2002.

[52] S Chien, Kl L Sung, R. Skalak, S Usami, and a Tözeren. Theoretical and experimental studies on viscoelastic properties of erythrocyte membrane. *Biophysical journal*, 24(November):463–87, 1978.

[53] G. Binnig and C. F. Quate. Atomic Force Microscope. *Physical Review Letters*, 56(9):930–933, 1986.

[54] Robert Bosch Gmbh. Fabrication and characterization of planar Gunn diodes for Monolithic Microwave Integrated Circuits . Herstellung und Charakterisierung planarer Gunn-Dioden für monolitisch Controlled Oscillator Monolithic Microwave Integrated Circuit . *Physics*.

[55] I Dulinska, M Targosz, W Strojny, M Lekka, P Czuba, W Balwierz, and M Szymonski. Stiffness of normal and pathological erythrocytes studied by means of atomic force microscopy. *Journal of Biochemical and Biophysical Methods*, 66:1–11, 2006.

[56] Weisenhorn and Khorsandi M. Deformation and height anomaly of soft surfaces studied with an AFM. *Nanotechnology*, 1993.

[57] Andreas Fery and Richard Weinkamer. Mechanical properties of micro- and nanocapsules: Single-capsule measurements. 48:7221–7235, 11 2007.

[58] M. C. Audry. Private communication. 2017.

[59] a Ashkin. Acceleration anf trapping of particles by radiation pressure, 1970.

[60] C. Coirault, J.-C. Pourny, F. Lambert, and Y. Lecarpentier. Les pinces optiques en biologie et en médecine. *Médecine/Sciences*, 19:364–367, 2003.

[61] J Guck, R Ananthakrishnan, H Mahmood, T J Moon, C C Cunningham, and J Käs. The optical stretcher: a novel laser tool to micromanipulate cells. *Biophysical journal*, 81(August):767–784, 2001.

[62] Bin Chen, Fang Guo, and Hao Xiang. Visualization study of motion and deformation of red blood cells in a microchannel with straight , divergent and convergent sections. (28):429–440, 2011.

[63] Puja Mishra, Martyn Hill, and Peter Glynne-Jones. Deformation of red blood cells using acoustic radiation forces. *Biomicrofluidics*, 8(3):034109, May 2014.

[64] N Wang, J P Butler, and D E Ingber. Mechanotransduction across the cell surface and through the cytoskeleton., 1993.

[65] Marina Puig-de-morales marinkovic, Kevin T Turner, James P Butler, Jeffrey J Fredberg, Subra Suresh, Turner Kt, Butler Jp, and Suresh S Viscoelasticity. Viscoelasticity of the human red blood cell. *American Journal of Physiology-Cell Physiology*, 293:C597–C605, 2007.

[66] Gabriel Popescu, Takahiro Ikeda, Ramachandra R Dasari, and Michael S Feld. Diffraction phase microscopy for quantifying cell structure and dynamics. *Optics letters*, 31(6):775–777, 2006.

[67] Gabriel Popescu, Yongkeun Park, Ramachandra R. Dasari, Kamran Badizadegan, and Michael S. Feld. Coherence properties of red blood cell membrane motions. *Physical Review E - Statistical, Nonlinear, and Soft Matter Physics*, 76(3):28–32, 2007.

[68] Eyal Ben-Isaac, Yongkeun Park, Gabriel Popescu, Frank L H Brown, Nir S. Gov, and Yair Shokef. Effective temperature of red-blood-cell membrane fluctuations. *Physical Review Letters*, 106:1–5, 2011.

[69] YongKeun Yk Park, Catherine a. Best, Tatiana Kuriabova, Mark L. Ml Henle, Michael S. Feld, Alex J. Levine, and Gabriel Popescu. Measurement of the nonlinear elasticity of red blood cell membranes. *Physical Review E*, 83:1–11, 2011.

[70] YongKeun Park, Catherine a Best, Kamran Badizadegan, Ramachandra R Dasari, Michael S Feld, Tatiana Kuriabova, Mark L Henle, Alex J Levine, and Gabriel Popescu. Measurement of red blood cell mechanics during morphological changes. *Proceedings of the National Academy of Sciences of the United States of America*, 107(15):6731–6736, 2010.

[71] G V Gass, L V Chernomordik, and L B Margolis. Local deformation of human red blood cells in high frequency electric field. 1093:162–167, 1991.

[72] Jochen Guck, Stefan Schinkinger, Bryan Lincoln, Falk Wottawah, Susanne Ebert, Maren Romeyke, Dominik Lenz, Harold M Erickson, Revathi Ananthakrishnan, Daniel Mitchell, Josef Käs, Sydney Ulvick, and Curt Bilby. Optical deformability as an inherent cell marker for testing malignant transformation and metastatic competence. *Biophysical journal*, 88(5):3689–3698, 2005.

[73] Mauritz Jma, T. Tiffert, R. Seear, F. Lautenschlager, A. Esposito, V. L. Lew, J. Guck, and C. F. Kaminskia. Detection of plasmodium falciparum-infected red blood cells by optical stretching. *J Biomed Opt*, 15(3), 2010.

[74] H. Engelhart and E. Sackmann. On the measurement of shear elastic moduli and viscosities of erythrocyte plasma membranes by transient deformation in high frequency electric fields. *Biophys J*, 54:495–508, 1988.

[75] E A Evans and R. Skalak. *Mechanics and thermodynamics of biomembranes*. Boca Raton, Florida CRC Press, 1980.

[76] L. A. MacQueen, M. D. Buschmann, and M. R. Wertheimer. Mechanical properties of mammalian cells in suspension measured by electro-deformation. *J Micromech Microeng*, 20, 2010.

[77] I. Doh, W. C. Lee, Y. H. Cho, a. P. Pisano, and F. a. Kuypers. Deformation measurement of individual cells in large populations using a single-cell microchamber array chip. *Applied Physics Letters*, 100(17):173702–1737023, April 2012.

[78] G. Du, A. Ravetto, Q. Fang, and den Toonder JMJ. Cell types can be distinguished by measuring their viscoelastic recovery times using a microfluidic device. *Biomed Microdevices*, 13:29–40, 2010.

[79] M. Gnerlich, S. F. Perry, and S. Tatic-Lucic. A submersible piezoresistive mems lateral force sensor for a diagnostic biomechanics platform. *Sensor Actuat A-Phys*, 188:111–119, 2012.

[80] B. Barazani, S. Warnat, A. Fine, and T. Hubbard. Mems squeezer for the measurement of single cell rupture force, stiffness change, and hysteresis. *J Micromech Microeng*, 27, 2017.

[81] N. Lafitte, H. Guillou, M. Kumemura, L. Jalabert, T. Fujii, H. Fujita, and D. Collard. Integrated mems platform with silicon nanotweezers and open microfluidic device for real-time and routine biomechanical probing on molecules and cells. 35th annual international conference of the ieee engineering in medicine and biology society (embs 2013). *Osaka, Japan*, pages 148–151, 2013.

[82] Alison M. Forsyth, Jiandi Wan, William D. Ristenpart, and Howard a. Stone. The dynamic behavior of chemically "stiffened" red blood cells in microchannel flows. *Microvascular Research*, 80(1):37–43, July 2010.

[83] S. S. Lee, Y. Yim, K. H. Ahn, and S. J. Lee. Extensional flow-based assessment of red blood cell deformability using hyperbolic converging microchannel. *Biomed Microdevices*, 11:1021–1027, 2009.

[84] D. R. Gosset, Tse Htk, A. S. Lee, Y. Ying, A. G. Lindgreen, O. O. Yang, J. Rao, A. T. Clark, and D. Di Carlo. Hydrodynamic stretching of single cells for large population mechanical phenotyping. *Proc Natl Acad Sci USA*, 109:7630–7635, 2012.

[85] G Tomaiuolo and S Guido. Start-up shape dynamics of red blood cells in microcapillary flow. *Microvascular Research*, 82(1):35–41, July 2011.

[86] Giovanna Tomaiuolo, Mario Barra, Valentina Preziosi, Antonio Cassinese, Bruno Rotoli, and Stefano Guido. Microfluidics analysis of red blood cell membrane viscoelasticity. *Lab on a chip*, 11:449–454, 2011.

[87] Giovanna Tomaiuolo, Luca Lanotte, Giovanni Ghigliotti, Chaouqi Misbah, and Stefano Guido. Red blood cell clustering in Poiseuille microcapillary flow. *Physics of Fluids*, 24(2012), 2012.

[88] Giovanna Tomaiuolo, Marino Simeone, Vincenzo Martinelli, Bruno Rotoli, and Stefano Guido. Red blood cell deformation in microconfined flow. *Soft Matter*, 5(19):3736, 2009.

[89] Gael Prado, Alexander Farutin, Chaouqi Misbah, and Lionel Bureau. Viscoelastic transient of confined red blood cells. *Biophysical Journal*, 108(9):2126–2136, 2015.

[90] Julien Picot, Papa Alioune Ndour, Sophie D. Lefevre, Wassim El Nemer, Harvey Tawfik, Julie Galimand, Lydie Da Costa, Jean Antoine Ribeil, Mariane de Montalembert, Valentine Brousse, Bruno Le Pioufle, Pierre Buffet, Caroline Le Van Kim, and Olivier Francais. A biomimetic microfluidic chip to study the circulation and mechanical retention of red blood cells in the spleen. *American Journal of Hematology*, 90(4):339–345, 2015.

[91] Hansen Bow, Igor V Pivkin, Monica Diez-Silva, Stephen J Goldfless, Ming Dao, Jacquin C Niles, Subra Suresh, and Jongyoon Han. A microfabricated deformability-based flow cytometer with application to malaria. *Lab on a chip*, 11(6):1065–1073, March 2011.

[92] S. Huang, A. Undisz, M. Diez-Silva, H. Bow, M. Dao, and J. Han. Dynamic deformability of plasmodium falciparum-infected erythrocytes exposed to artesunate in vitro. *Integr Biol*, 5:414–422, 2013.

[93] S Braunmüller, L Schmid, E Sackmann, and T Franke. Hydrodynamic deformation reveals two coupled modes/time scales of red blood cell relaxation. *Soft Matter*, 8(44):11240, 2012.

[94] M. Abkarian, M. Faivre, and H. A. Stone. High-speed microfluidic differential manometer for cellular-scale hydrodynamics. *Proc Natl Acad Sci USA*, 103(3):538–542, 2006.

[95] M. Horton R. Smistrup K. Best-Popescu C. A. Abkarian, M. Faivre and H. A. Stone. Cellular-scale hydrodynamics. *Biomed Mater*, 3, 2008.

[96] Z. S. Khan and S. A. Vanapalli. Probing the mechanical properties of brain cancer cells using a microfluidic cell squeezer device. *Biomicrofluidics*, 7, 2013.

[97] Quan Guo, Sarah J. Reiling, Petra Rohrbach, and Hongshen Ma. Microfluidic biomechanical assay for red blood cells parasitized by Plasmodium falciparum. *Lab on a Chip*, 12(6):1143, March 2012.

[98] Marie-Eve Myrand-Lapierre, Xiaoyan Deng, Richard R. Ang, Kerryn Matthews, Aline T. Santoso, and Hongshen Ma. Multiplexed fluidic plunger mechanism for the measurement of red blood cell deformability. *Lab Chip*, 15(1):159–167, 2015.

[99] B. M. Cooke, N. Mohandas, and R. L. Coppel. The malaria-infected red blood cell: structural and functional changes. *Adv Parasit*, 50:1–86, 2001.

[100] Quan Guo, Simon P. Duffy, Kerryn Matthews, Aline T. Santoso, Mark D. Scott, and Hongshen Ma. Microfluidic analysis of red blood cell deformability. *Journal of Biomechanics*, 47(8):1767–1776, June 2014.

[101] Julien Marchalot, Jean François Chateaux, Magalie Faivre, Hichem C. Mertani, Rosaria Ferrigno, and Anne Laure Deman. Dielectrophoretic capture of low abundance cell population using thick electrodes. *Biomicrofluidics*, 9(5):1–13, 2015.

[102] A. L. Rakow and R. M. Hochmuth. Effect of heat treatment on the elasticity of human erythrocyte membrane. *Biophysical Journal*, 15(11):1095–1100, 1975.

[103] Younan Xia and George M. Whitesides. Soft Lithography, 1998.

[104] F. Quemeneur. Relationship between mechanical parameters and behaviour under external stresses in lipid vesicles with modified membranes. *PhD Thesis*, 2010.

[105] M. Mohri, H. Kakinuma, M. Sakamoto, and H. Sawai. Plasma Etching of ITO Thin Films Using a CH_4/H_2 Gas Mixture. *Japanese Journal of Applied Physics*, 29:L1932–L1935, October 1990.

[106] Magalie Faivre. Drops , vesicles and red blood cells : Deformability and behavior under flow. *PhD Thesis*, 2006.

[107] Meongkeun Ju, Swe Soe Ye, Bumseok Namgung, Seungkwan Cho, Hong Tong Low, Hwa Liang Leo, and Sangho Kim. A review of numerical methods for red blood cell flow simulation. *Computer Methods in Biomechanics and Biomedical Engineering*, 18(2):130–140, 2015. PMID: 23582050.

[108] C.T. et al. Lim. Mechanical models for living cells,Äîa review. *Journal of Biomechanics*, 39.

[109] Fung Yc. *Biomechanics: mechanical properties of living tissues*. Springer-Verlag, New York, 2nd edition, 1993.

[110] H. Noguchi and G. Gompper. Shape transitions of fluid vesicles and red blood cells in capillary flows. *P Natl Acad Sci USA*, 102(40):14159–14164, 2005.

[111] D. A. Fedosov, B. Caswell, and Karniadakis Ge. A multiscale red blood cell model with accurate mechanics, rheology, and dynamics. *Biophys J.*, 98(10):2215–2225, 2010.

[112] J. Li, M. Dao, C. T. Lim, and S. Suresh. Spectrin-level modeling of the cytoskeleton and optical tweezers stretching of the erythrocyte. *Biophys J.*, 88(5):3707–3719, 2005.

[113] O. Y. Zhongcan and W. Helfrich. Bending energy of vesicle membranes - general expressions for the 1st, 2nd, and 3rd variation of the shape energy and applications to spheres and cylinders. *Phys Rev A.*, 39(10):5280–5288, 1989.

[114] Z. G. Zhang and X. W. Zhang. Mechanical behavior of the erythrocyte in microvessel stenosis. *Science China Life Sciences*, 54:450–458, 2011.

[115] Aleksey Ni, Taqi Ahmad Cheema, and Cheol Woo Park. Numerical study of RBC motion and deformation through microcapillary in alcohol plasma solution. *Open Journal of Fluid Dynamics*, (March):26–33, 2015.

[116] A. Rodriguez Ferran A. Huerta J. Donea, J.Ph. Ponthot. *Encyclopedia of Computational Mechanics Volume 1: Fundamentals*, volume 1. 2004.

[117] H. Engelhardt, H. Gaub, and E. Sackmann. Viscoelastic properties of erythrocyte membranes in high-frequency electric fields. *Nature*, 307(5949):378–80, 1984.

[118] Herbert A. Pohl. The motion and precipitation of suspensoids in divergent electric fields. *Journal of Applied Physics*, 22(7):869–871, 1951.

[119] Nathan Swami, Chia-Fu Chou, Venkatraman Ramamurthy, and Vasudha Chaurey. Enhancing dna hybridization kinetics through constriction-based dielectrophoresis. *Lab Chip*, 9:3212–3220, 2009.

[120] Ronald Pethig. Dielectrophoresis: Status of the theory, technology, and applications. *Biomicrofluidics*, 4(2):1–35, 2010.

[121] I-Fang Cheng, Hsien-Chang Chang, Diana Hou, and Hsueh-Chia Chang. An integrated dielectrophoretic chip for continuous bioparticle filtering, focusing, sorting, trapping, and detecting. *Biomicrofluidics*, 1(2):021503, 2007.

[122] G. W. Leung, F. T. Lau, S. L. Leung, and W. J. Li. Formation of au colloidal crystals for optical sensing by dep-based nano-assembly. In *2007 2nd IEEE International Conference on Nano/Micro Engineered and Molecular Systems*, pages 922–926, Jan 2007.

[123] Igor Cima, Chay Wen Yee, Florina S. Iliescu, Wai Min Phyo, Kiat Hon Lim, Ciprian Iliescu, and Min Han Tan. Label-free isolation of circulating tumor cells in microfluidic devices: Current research and perspectives. *Biomicrofluidics*, 7(1), 2013.

[124] H Engelhardt and E Sackmann. On the measurement of shear elastic moduli and viscosities of erythrocyte plasma membranes by transient deformation in high frequency electric fields. *Biophysical journal*, 54(3):495–508, 1988.

[125] E Du, Ming Dao, and Subra Suresh. Quantitative Biomechanics of Healthy and Diseased Human Red Blood Cells using Dielectrophoresis in a Microfluidic System. *HHS Public Access*, (1):35–41, 2014.

[126] Ezekiel O. Adekanmbi and Soumya K. Srivastava. Dielectrophoretic applications for disease diagnostics using lab-on-a-chip platforms. *Lab Chip*, 16:2148–2167, 2016.

[127] Michael P. Hughes. Fifty years of dielectrophoretic cell separation technology. *Biomicrofluidics*, 10(3):1–9, 2016.

[128] A. Mortadi, A. El Melouky, E. G. Chahid, R. El Moznine, and O. Cherkaoui. Studies of the clausius,ÄìMossotti factor. *Journal of Physical Studies*, 20(4):4001–1–4001–4, 2016.

[129] Swagatika Dash and Swati Mohanty. Dielectrophoretic separation of micron and submicron particles: A review. *Electrophoresis*, 35(18):2656–2672, 2014.

[130] Wonhgee Lee; Peter Tseng; Dino Di Carlo. *Microtechnology for cell manipulation and sorting*. 2017.

[131] J. Gimsa, P. Marszalek, U. Loewe, and T. Y. Tsong. Dielectrophoresis and electrorotation of neurospora slime and murine myeloma cells. *Biophysical Journal*, 60(4):749–760, 1991.

[132] Peter Gascoyne, Ronald Pethig, Jutamaad Satayavivad, Frederick F. Becker, and Mathuros Ruchirawat. Dielectrophoretic detection of changes in erythrocyte membranes following malarial infection. *Biochimica et Biophysica Acta - Biomembranes*, 1323(2):240–252, 1997.

[133] Vladimir L. Sukhorukov, Gustav Meedt, Markus Kürschner, and Ulrich Zimmermann. A single-shell model for biological cells extended to account for the dielectric anisotropy of the plasma membrane. *Journal of Electrostatics*, 50(3):191–204, 2001.

[134] E A. Evans and Paul La Celle. ntrinsic material properties ofbthe erythrocyte membrane indicated by mechanical analysis of deformation. *blood*, 45(1), 1975.

[135] Shinya Sakuma, Keisuke Kuroda, Chia-Hung Dylan Tsai, Wataru Fukui, Fumihito Arai, and Makoto Kaneko. Red blood cell fatigue evaluation based on the close-encountering point between extensibility and recoverability. *Lab on a Chip*, 14(6):1135, 2014.

[136] Gelszinnis Renaud. Approches microfluidiques pour la séparation de cellules parasitées. *PhD Thesis*, pages 1–167, 2015.

[137] Kendra D. Nyberg, Michael B. Scott, Samuel L. Bruce, Ajay B. Gopinath, Dimitri Bikos, Thomas G. Mason, Jin Woong Kim, Hong Sung Choi, and Amy C Rowat. The physical origins of transit time measurements for rapid, single cell mechanotyping. *Lab Chip*, 16(17):3330–3339, 2016.

[138] T. C. Fisher, F. J. Van Der Waart, and H. J. Meiselman. The influence of suspending phase viscosity on the passage of red blood cells through capillary-size micropores. *Biorheology*, 33(2):153–168, 1996.

[139] Masumi Yamada, Megumi Nakashima, and Minoru Seki. Pinched flow fractionation:,Äâ continuous size separation of particles utilizing a laminar flow profile in a pinched microchannel. *Analytical Chemistry*, 76(18):5465–5471, 2004. PMID: 15362908.